Studies on Resistive Plate Chambers (RPC) for INO and scintillators for reactor antineutrino detection

By

Varchaswi K S Kashyap

PHYS01201004018

Nuclear Physics Division,
Bhabha Atomic Research Centre (BARC),
Mumbai - 400 085

A thesis submitted
to the Board of Studies in
Physical Sciences

In partial fulfillment of requirements
For the Degree of

DOCTOR OF PHILOSOPHY
of
HOMI BHABHA NATIONAL INSTITUTE

June, 2016

ii

Homi Bhabha National Institute

Recommendations of the Viva Voce Committee

As members of the Viva Voce Committee, we certify that we have read the dissertation prepared by **Varchaswi K S Kashyap** entitled **"Studies on Resistive Plate Chambers (RPC) for INO and scintillators for reactor antineutrino detection"** and recommend that it may be accepted as fulfilling the thesis requirement for the award of Degree of Doctor of Philosophy.

Chairman - Prof. A. K. Mohanty	**Date:**
Guide / Convener - Prof. L. M. Pant	**Date:**
Examiner - Prof. V. Bhatnagar	**Date:**
Member 1 - Prof. B. S. Acharya	**Date:**
Member 2 - Prof. Amar Sinha	**Date:**
Technical Advisor - Dr. B. Satyanarayana	**Date:**

Final approval and acceptance of this thesis is contingent upon the candidate's submission of the final copies of the thesis to HBNI.

I hereby certify that I have read this thesis prepared under my direction and recommend that it may be accepted as fulfilling the thesis requirement.

Date:

Place: **Prof. L M Pant (Guide)**

DECLARATION

I hereby declare that the investigation presented in the thesis has been carried out by me. The work is original and has not been submitted earlier as a whole or in part for a degree/diploma at this or any other Institution/University.

June 2016, Mumbai

Varchaswi K S Kashyap

List of Publications arising from the thesis

Publications in Refereed Journal

Published

1. V. K. S. Kashyap, L. M. Pant, A. K. Mohanty, and V. M. Datar, Simulation results of Liquid and Plastic scintillator detectors for reactor antineutrino detection - A comparison, *Journal of Instrumentation*, 11(03):P03005, 2016.

Accepted

1. V. K. S. Kashyap, C. Yadav, S. T. Sehgal, R. Sehgal, R. G. Thomas, L. M. Pant, A. K. Mohanty, Plastic scintillator based hodoscope for characterization of large area RPCs, *Pramana - J. Phys*.

Communicated

1. INO Collaboration. Physics potential of the ICAL detector at the India-based Neutrino Observatory (INO). arXiv, (1505.07380v1), 5 2015. *Pramana - J. Phys*.

Symposium and conference proceedings

1. Monte Carlo simulation for estimation of trigger rate in Cosmic Hodoscope at NPD-BARC, V. K. S. Kashyap et al, *Proceedings of the DAE-BRNS Symp. on Nucl. Phys. 57 (2012) 936*

2. Avalanche mode operation of a Glass RPC with humid gas mixture, V. K. S. Kashyap et al, *Proceedings of the DAE-BRNS Symp. on Nucl. Phys. 58 (2013) 870*

3. Simulation and conceptual design of a detector for sterile neutrino search and remote reactor monitoring, V. K. S. Kashyap et al, *Proceedings of the DAE-BRNS Symp. on Nucl. Phys. 58 (2013) 946*

4. Characterization of 1 m x 1 m Glass RPC with "ANUSPARSH-II" ASIC based Frontend DAQ Electronics, V. B. Chandratre et al, *Proceedings of the DAE-BRNS Symp. on Nucl. Phys. 58 (2013) 992*

5. Performance of ANUSPARSH-III ASIC chipset with 1 m $\times$ 2 m glass RPC, V. K. S. Kashyap et al, *Proceedings of the DAE-BRNS Symp. on Nucl. Phys. 59 (2014) 852*

6. Background measurements at the DHRUVA reactor site for feasibility studies towards antineutrino detection from reactors, V K S Kashyap et al, *Proceedings of the DAE-BRNS Symp. on Nucl. Phys. 59 (2014) 978*

7. Liquid and plastic scintillator detectors for detecting antineutrinos from reactors - A GEANT4 simulation study, V. K. S. Kashyap et al, *Proceedings of the DAE-BRNS Symp. on Nucl. Phys. 59 (2014) 944*

8. G-10 read out panel 1 m × 1 m as an option for RPCs in INO, S T Sehgal et al, *Proceedings of the DAE-BRNS Symp. on Nucl. Phys. 59 (2014) 922*

9. Time distribution measurements of prompt-delay events at the Dhruva reactor for detection of antineutrinos, V. K. S. Kashyap et al, *Proceedings of the DAE-BRNS Symp. on Nucl. Phys. 60 (2015) 924*

10. Simulation of detector response for antineutrino induced events with a proto-type plastic detector array, S. P. Behera et al, *Proceedings of the DAE-BRNS Symp. on Nucl. Phys. 60 (2015) 1032*

11. Variation in the thermal neutron flux at the anti-neutrino measurement site in the Dhruva reactor, A K Singh et al, *Proceedings of the DAE-BRNS Symp. on Nucl. Phys. 60 (2015) 968*

12. Development of large area (1 m × 2 m) bakelite gas gaps in India for INO and related experiments, V. K. S. Kashyap et al, *Proceedings of the DAE-BRNS Symp. on Nucl. Phys. 60 (2015) 946*

Varchaswi K S Kashyap

DEDICATED TO

My family

ACKNOWLEDGEMENTS

garding antineutrino detectors and reactor monitoring.

I also like to thank Mr. Avinash Joshi from Alpha Pneumatics Pvt. Ltd.

I am highly thankful to my closest friends Revathi and Milind and also my school buddies Girish, Satish, Suhas and Hrishikesh for their warmth and encouragement.

I owe a lot to my father Late. Sri. C. G. Kumara Swamy, who influenced me greatly. He would always be interested to learn more about anything he did, always strived towards perfection and was a 'Jack of All' kind of a person. Unfortunately, he was not able to see me complete my PhD. I cannot thank enough my mother Vanaja Swamy who's love and care has made me what I am today. Her concern and prayers have have always been with me. I am thankful to my brother Yashaswi K. R. Kashyap who never asked as to what I was doing, always believed in me and supported me.

I thank the almighty for giving me strength and will to pursue my wish of doing a PhD. I am grateful to my guru Vid. L. Ramasesha who taught me classical music and influenced my personality.

The open source community has been a gift. It has made numerous scientific tools used extensively in physics research, easily accessible to people free of cost. I'd like to express my thanks to the Linux, LaTeX, GEANT and ROOT communities.

Contents

Synopsis

Prelude

Neutrino oscillation has been one of the most fascinating topics in Particle physics. Neutrinos oscillate from one flavor to the other as they propagate. This exhorts us to accept the fact that they possess a very tiny but finite mass which according to the Standard Model of particle physics is zero. The determination of this mass and precision measurement of the oscillation parameters has long standing implications on our understanding of nature like the origin of the universe and the dominance of matter over antimatter.

Neutrinos are chargeless and interact through the weak interaction. This makes the task of studying them very difficult and challenging even though they are the second most abundant particles in the universe - first being photons. Detectors needed to study them must be huge and functioning over a long period of time to achieve sufficient statistics.

The magnetized Iron Calorimeter (ICAL) detector at the proposed India-

based Neutrino Observatory (INO) aims at the precision measurement of neutrino oscillation parameters and determination of neutrino mass hierarchy [1]. Antineutrinos emitted from the core of the reactors can be used to monitor them remotely. This concept proposed by Mikaélyan in the 1970s and demonstrated first by experiments at Rovno reactor in USSR in the late 1980s [2], can be used to determine the state of the fuel burnup in a nuclear reactor in a non intrusive way. It can also be used to check nuclear proliferation. This is interesting since one of the most elusive particles in the universe - the neutino, finds application. Due to the re-evaluation of the antineutrino flux from the core of reactors an anomaly known as the Reactor Antineutrino Anomaly has come into picture. There is a possiblity of the existence of the so called sterile neutrino - A neutrino which does not interact by any of the standard model interactions but only through gravitation and mixing. Detectors used for monitoring can also be used to probe the existence of light sterile neutrinos. It has been proposed to setup a 1 t detector made of plastic scintillator bars near the research reactor at BARC for this purpose.

The thesis focussing on detector studies for neutrino experiments and has been divided into two parts. The first part focusses on studies related to RPC - characterization of the RPC with G10 and polycarbonate honeycomb readouts using a hodoscope to obtain all relavent parameters such as efficiency, clustersize, timing characteristics and testing of RPC using ANUSPARSH ASIC based frontend. The second discusses the simulations done to compare plastic and liquid scintillator detectors for detecting electron antineutrinos produced from the core of nuclear reactors in relation to reactor monitoring and some preliminary background measurements.

PART I - Studies on Resistive Plate Chambers (RPC) for INO

Introduction

The detector elements in the proposed ICAL detector at INO are RPCs. ICAL will be a 50 kt magnetized iron calorimeter with a magnetic field of ~1.5 tesla. It will have alternating layers of iron plates and RPCs. The dimension of this humongous detector is 48 m × 16 m × 14.5 m [1]. ICAL will use the RPCs to track the path of particles generated after the interaction of neutrinos in the iron plates. RPCs [3] are gaseous detectors having resistive electrodes usually made of bakelite or glass. Particles are detected when they ionize the gas mixture. Depending on the gas composition and mode of operation, signals are induced on readout strips by the generation of avalanche or streamers after ionization in presence of a high electric field. The geometry, shape and configuration of RPCs depends on the application and requirement. RPCs are fast detectors possessing excellent timing properties. They are inexpensive, have good position resolution and can cover large area. They are used for trigger, tracking and timing purposes in many high energy physics experiments.

Plastic Scintillator based Hodoscope

The proposed ICAL at INO [4] would require approximately 30000 RPCs of ~4 m^2 area. These experiments are built underground and operate over long periods of time. If detectors develop problems when these experiments are running, it is not possible to service or replace them. Therefore, RPCs need to be tested

thoroughly before being employed. The dimension and number of RPCs needed for these experiments, requires a setup which can characterize each RPC in a reasonable amount of time for functional parameters such as efficiency, cluster size, strip profile and noise rate. A cosmic muon hodoscope is a suitable option.

Hodoscope is an instrument which is used to detect the path of a particle. The hodoscope at NPD-BARC was constructed to characterize RPCs with cosmic muons, both for the RE4 (4th RPC Endcap disk) upgrade for the CMS experiment during the long shutdown (LS1) and also for the R & D related to RPCs for INO, muon tomography and related experiments [5]. The Hodoscope contains sixteen large area scintillators for characterization of RPCs using cosmic muons as triggers. These large area scintillators have been fabricated to fully characterize RPCs in one go covering the entire active area. The hodoscope is equipped with high voltage cables, gas lines and racks for placement and characterization of RPCs. It can handle RPCs upto 1 m × 2 m dimension and is connected to a VME based data acquisition system. CERN based software has been adapted to the hodoscope. Multiple RPCs can be characterized simultaneously in a programmable automated manner.

Glass RPC with G10 readout

1 m^2 square Glass RPC with G10 readouts operating in the avalanche mode has been characterized using the hodoscope. Glass gas gap has been fabricated in KODEL (Korean Detector Lab), South Korea. The surface resistivity of the conductive graphite coating is 1 MΩ/square.

The proposed ICAL detector at INO has alternating layers of iron plates and

RPC. The spacing between two layers of iron plates (plate thickness 5.6 cm) is 4 cm. Glass gas gaps used in a glass RPC have a total thickness of 8 mm, 3 mm thickness of two glass plates each + electrode spacing of 2 mm. This coupled with polycarbonate honeycomb based readouts having thickness of ~5 mm and cage for electromagnetic shielding, will make the RPC thicker and could cause difficulty in handling. To reduce the thickness of the RPC, readout based on G10 having a thickness of 1 mm has been explored. These readouts have been fabricated by a local company in Mumbai.

The readout has 32 strips of copper each 1 m long and 3 cm wide. The characteristic impedence of these strips is 5 Ω. Since the preamplification electronics have 50 Ω impedance signals will be distorted due to reflection. Reflection has been reduced by using a matching resistive circuit [6]. RPC has been characterized and shows an efficiency of ~95 %. Clustersize is less than 2 strips per event on average [5].

Testing of RPC with Anusparsh ASIC based preamplifier electronics

ANUSPARSH ASIC based preamplifier electronics developed by Electronics Division, BARC is a suitable option for the frontend in the ICAL detector. Efficiency and timing characteristics of the RPC with polycarbonate honeycomb readouts has been tested using these boards and the results are comparable with that measured with G10 using HMC based preamplifiers.

PART II - Scintillators for reactor antineutrino detection

Introduction

Nuclear reactors are the strongest man made sources of electron antineutrinos. Electron antineutrinos are emitted in the decay chains of fission fragments in core of reactors. Four isotopes ^{235}U, ^{238}U, ^{239}Pu and ^{241}Pu contribute to 99.9% of the thermal power in a nuclear reactor. Among them ^{235}U and ^{239}Pu are the main fissioning isotopes. It is known that the flux of antineutrinos emitted from the decay chains of fission fragments of ^{235}U is higher as compared to that of ^{239}Pu. Due to the "Burnup effect", as the reactor operates, the number of antineutrinos emitted will decrease over time due to the formation of ^{239}Pu as ^{235}U gets consumed. The number of antineutrinos that can be detected is given by the expression

$$N_{\nu_e} = \gamma(1 + k)P_{th} \tag{1}$$

where γ is a constant which depends on the detector and the geometry, P_{th} is the thermal power and k is the fuel composition which evolves with time. It is possible to monitor reactors remotely utilizing the difference in the energy spectrum of neutrinos emitted by the fissioning isotopes (^{235}U and ^{239}Pu) in a reactor. IAEA (International Atomic Energy Agency) the UN body for peaceful use of nuclear energy has also shown interest in using the neutrino method as a new safeguards tool.

Improved calculations done on the neutrino flux shows a 3% increase in the expected number of antineutrinos from reactors [7, 8]. Re-evaluation of the data

of neutrino experiments performed at source to detector distances <100 m using these fluxes, shows that the ratio of observed to expected neutrinos is less than unity. This has been termed as the Reactor Antineutrino Anomaly (RAA) [9]. This anomaly may be due to something related to reactor systematics or some unknown physical phenomena. If it is not due to the former, then, RAA cannot be understood within the 3 neutrino framework. However, if a fourth flavor known as the sterile neutrino is postulated, and if it mixes with $\bar{\nu}_e$, then the deficit in their measured number at short distances can be understood. Experiments at very short baselines of tens of meters can determine the existence of the sterile neutrino or help improve our understanding of reactor physics. The electron antineutrino survival probability in the two flavor scenario is given by

$$P_{ee} = 1 - \sin^2(2\theta_{new}) \sin^2 \left(\frac{\Delta m_{new}^2 L}{4E_{\bar{\nu}_e}} \right) \tag{2}$$

where, θ_{new} is the mixing angle, $E_{\bar{\nu}_e}$ is the energy of the electron antineurino, L is the source to detector distance and Δm_{new}^2 is the mass squared difference. To observe oscillation at such short distances, the mass squared difference Δm_{new}^2 should be ~ 1 eV^2.

Inverse neutron beta decay reaction

$$\bar{\nu}_e + p \rightarrow n + e^+ \tag{3}$$

is a very strong signature used for detecting electron antineutrinos. Detectors rich in free protons such as organic scintillators are most suitable. In the detector a neutrino interacts with a free proton and produces a positron and a neutron. Positron carries most of the neutrino's energy. The positron annihilates after depositing its energy almost immediately producing 2 gamma rays of 511 keV

each. This is the prompt event. The energy of the neutron is around tens of keV and it thermalizes in the detector finally getting captured releasing a cascade of gamma rays upto ~8 MeV. Detectors are usually doped with high neutron capture cross section elements like Gd for this purpose. This forms the delayed signal. A correlated signature of this type is the signal of a neutrino.

The energy averaged interaction cross section of antineutrinos from reactors is of the order $10^{-43} cm^2$. Since reactors are a copious source of antineutrinos, a modestly sized detector (~1 t) is sufficient for sterile neutrino mixing studies and reactor monitoring to be carried out on a reasonable amount of time.

Detectors made of plastic or liquid scintillators are suitable options. Simulations on detector designs based on existing experiments like NUCIFER[10], PANDA[11] and Ref. [12] have been performed for comparison.

It has been proposed to set up a plastic scintillator based detector array called ISMRAN (India's Scintillator Matrix for Reactor AntiNeutrino) of mass 1 t near the Dhruva research reactor site at BARC to understand and develop the technology of reactor monitoring and do possible physics studies. The detector will have 100 Gadolinium foil wrapped plastic scintillator bars each coupled to two PMTs so as to form a cube of side 1 m.

Simulation of liquid and plastic scintillator geometries

Simulations have been performed on liquid and plastic scintillator based detectors modelling detector geometries in GEANT4 [13] using parameters of commercially available scintillators from Eljen Technology Ltd. and Saint-Gobain Ceramics and Plastics Inc.

The plastic scintillator geometry is modular and cubical made of 100 plastic scintillator (EJ-200 (Eljen)/BC-408 (Saint-Gobain)) units. The total volume has been fixed to 1 m^3 so that the mass of the detector is ~1 t. Two variations have been considered where in the first case called 'Mono', each unit has one plastic bar coupled to two photomultipliers and in the second case called 'Quad', each unit has four smaller bars coupled to two photomultipliers using light guides. The total number of readout channels (200) remains the same in both cases. Each bar is wrapped with Gd_2O_3 coated aluminized mylar foils with Gd_2O_3 density of either 4.8 mg·cm^{-2} or 2.4 mg·cm^{-2} [14].

The Liquid scintillator geometry has ~1 m^3 of Gd doped liquid filled in a steel vessel coupled to large area photomultipliers using an acrylic disk. The Gd doping has been considered to be 0.25%. Two commercially available liquid scintillators EJ-331 (Eljen)/BC-521 (Saint-Gobain) and EJ-335 (Eljen)/BC-525 (Saint-Gobain) have been modeled [14].

Performances of the detector configurations for neutron capture, efficiency and resolutions have been compared [14].

In any neutrino experiment background reduction is of paramount importance. For reactor experiments accidental coincidences mimicking a correlated event from cosmic rays, fast neutrons and background radioactivity are a major concern. The smaller the neutron capture time window the better. Liquid shows the smallest mean capture time (~12 μs). The quad design has a moderate capture time (~30 or 40 μs depending on Gd_2O_3 coat density) and the mono has a large capture time (~65 μs)[14].

Liquid scintillator geometry shows better efficiency compared to plastic scintillator based geometry. Owing to the higher proton content, the event rate in liq-

uid scintillator detectors are higher compared to the plastic. More statistics can be achieved for the same duration. Liquid scintillators have simplified readout, reducing the number of channels. They are cheaper compared to the plastic array and have pulse shape discrimination ability. However, they have toxicity, long term stability and flammability concerns. Using event topology, prompt and delayed events can be identified using the plastic geometry. In the case of reactor monitoring although a little expensive, measurements with the plastic scintillator are feasible. They do not have flammability concerns. They are easy to handle and have no stability issues. These factors are very important if the detector is to be mounted on a mobile unit.

Considering the issues of safety and the distance at which these detectors would be placed from the reactor, plastic scintillator based geometry appears to be more suitable. The efficiency is lower but still manageable.

Background measurements

To assess the background at the reactor site, measurements with gamma and neutron detectors have been done. Combinations of shielding for neutron and gamma have been used to understand the background. It is seen that most of the high energy gamma background is due to the radiative capture of thermal neutrons on materials in the surrounding environment such as walls, support structures etc.

Conclusion

A plastic scintillator based hodoscope has been instrumented. Using this hodoscope multiple RPCs can be characterized for functional parameters such as efficiency, clustersize, strip profile and timing characterstics. For an experiment like ICAL at INO, hodoscopes such as this at multiple centres are necessary considering the huge deployment of RPCs. RPC with G10 readout has been characterized and its performance is good. RPC assembled with polycarbonate honeycomb readouts has also been tested with ANUSPARSH ASIC based frontend electronics developed by Electronics Division, BARC for fast detectors. The results are comparable with that measured with G10 and Hybrid Micro Circuit (HMC) based preamplifiers.

Liquid and plastic scintillation detectors have been compared through simulations using the GEANT4 framework. Plastic scintillator based detectors are preferrable when it comes to safety and mobility. Their performance is slightly poor compared to liquid scintillator based detector but manageable.

Preliminary background measurements have been done at the proposed site for the reactor antineutrino detector. The sources of background is mainly due to gamma generated after the radiative capture of neutrons in the surrounding support structures and walls. Fast neutron and thermal neutron background also exist which have to be properly shielded.

Outlook

Bakelite is another material used in RPCs. They have certain advantages when compared to glass. They are lighter, relatively flexible and have bulk resistivity an order of magnitude lesser. Handling is easier. The scale of RPC deployment is enormous in the case of ICAL at INO. So it would be worthwhile to explore the possibility of using bakelite RPCs in INO. This would require the identification and collaboration with Indian bakelite industries, testing and benchmarking of bakelite RPCs produced in India. In this regard 1 m × 2 m bakelite RPCs have been procured from General Tecnica, Italy. Parallely, bakelite procured in India are being fabricated into gas gaps for RPCs by a local company in Mumbai to be assembled and tested.

RPCs are potential candidates for use as detectors for detecting contraband materials utilizing the principle of muon tomography. Due to their large area and relatively lower cost they can be used to check for illegal trasportation of contraband materials through cargo at seaports and airports.

Among the plastics, mono geometry is the simplest. A small prototype with 20 plastic bars of the mono variant called Mini-ISMRAN will be assembled at the Dhruva research reactor hall with shielding for both gamma and neutrons. Neutrons will be shielded using Borated rubber or polythene and lead will be used to shield from gamma. For cosmic muon shielding, active veto detectors will be used. This will give an idea if the quad design is indeed necessary.

List of Figures

List of Tables

List of Abbreviations

ASIC   Application Specific Integrated Circuit

BARC   Bhabha Atomic Research Centre

BGO   Bismuth Germanium Oxide

BP   Borated Polyethylene

BR   Borated Rubber

CAMAC   Computer Automated Measurement and Control

CERN   Conseil Européen pour la Recherche Nucléaire,

                The European Organization for Nuclear Research

CMS   Compact Muon Solenoid

DONUT   Direct Observation of the NU Tau

DPP-PSD   Digital Pulse Processing - Pulse Shape Discrimination

ECL   Emitter Coupled Logic

FPGA   Field Programmable Gate Array

HMC   Hybrid Micro Circuit

HPGe   High Purity Germanium

ICAL   Iron CALorimeter

IMB   Irvine-Brookhaven-Michigan

INO   India-based Neutrino Observatory

ISMRAN   India's Scintillator Matrix for Reactor AntiNeutrino

LVDS   Low Voltage Differential Signaling

LYBO   Lithium Yttrium BOrate

MSP   Mass Stopping Power

MWPC   Multi-Wire Proportional Counter

NIM   Nuclear Instrument Module

NPD   Nuclear Physics Division

PANDA   Plastic AntiNeutrino Detector Array

PET   Poly Ethylene Terephthalate

PPC   Parallel Plate Counter

PSC   Planar Spark Chamber

RPC   Resistive Plate Chamber

SK Super Kamiokande

SLAC Stanford Linear Accelerator Centre

SNO Sudbury Neutrino Observatory

TAC Time to Amplitude Converter

TIFR Tata Institute of Fundamental Research

VME Versa Module Eurocard

Neutrino

1.1 Brief history

In 1930, Wolfgang Pauli postulated a new particle to explain the continuous energy spectrum observed in the process of beta decay. He wrote

> *"I have done something very bad today by proposing a particle that cannot be detected; it is something no theorist should ever do."*

in a letter to a group of experimental physicists at Tuebingen, Germany, explaining it as a desperate remedy. He called the particle as "neutron". In 1932, James Chadwick discovered a more massive neutral particle and also named it the neutron. The name "neutrino" (meaning "little neutral one" in Italian) was coined by Enrico Fermi to avoid confusion when he developed his theory to explain the process of beta decay (1934) in which, a neutron (discovered by Chadwick) decayed into a proton emitting an electron and a neutrino (postulated by Pauli).

$$n \rightarrow p + e^- + \bar{\nu}_e \qquad (1.1)$$

1

The process of beta decay had been observed already and the model of the atom and the nucleus was beginning to take shape. Great physicists like Neils Bohr, were even willing to consider that the law conservation of energy was valid only under statistical circumstances to explain beta decay.

The theory of beta decay put forth by Fermi was a milestone in the theory of weak interactions. The theory of relativity and quantum mechanics was being developed at the same time using which Dirac was able to predict the existence of antiparticles. Discovery of the positron by Anderson in 1932 proved this prediction.

In 1937, another particle - the muon (μ), was discovered in cosmic ray experiments by J.C. Street, E.C. Stevenson [15] and S.H. Neddermeyer, C. D. Anderson [16]. The observation of the decay of the muon in a few years led to the establishment of the universality of Fermi interactions. The neutrino had not been observed yet.

The interaction strength for the neutrino was so weak that people thought its detection was impossible. F. Reines and C. L. Cowan setup an experiment to detect neutrinos produced in nuclear reactors. They hoped to detect the neutrino via the inverse neutron beta decay reaction:

$$\bar{\nu}_e + p \rightarrow n + e^+. \tag{1.2}$$

The initial results of their experiment in 1953 at the nuclear power plant at Hanford, Washington, were unconvincing since they were looking only at the signal from the gamma after positron annihilation. In 1956, at the nuclear power plant at Savannah River, South Carolina, they were able to detect the neutrino [17].

Meanwhile, another problem existed - the decay of K^+ by two different modes known as the $\tau - \theta$ puzzle, where the K^+ sometimes decayed into two pions (θ) and sometimes into three pions (τ). The process could occur only if parity was violated in weak decays.

Considering the suggestions of T. D. Lee and C. N. Yang, an experiment was performed by Madam Wu et al [18], using a polarized ^{60}Co source. This experiment which spanned ~8 min, concluded that parity was violated in beta decay. Further, parity violation was also observed in the decays $\pi \rightarrow \mu + \nu$ and $\mu \rightarrow e + 2\nu$ by Richard L. Garwin, Leon M. Lederman and Marcel Weinrich [19]. Whether these neutrinos were same as that emitted during beta decay was to be determined.

The answer to the above question came when the muon neutrino was discovered by Leon M. Lederman, M. Schwartz, J. Steinberger and co-workers at the Brookhaven National Laboratory, using the proton accelerator and detectors with spark counters weighing 10 t [20].

The τ lepton was discovered in 1975 by Martin Perl and group at SLAC [21]. The existence of τ lepton naturally implied the existence of the last neutrino flavor ν_τ. It was discovered in 2001, by the DONUT experiment at Fermilab [22].

1.1.1 The Standard Model

One of the greatest works in physics has been the development of the Standard Model of particle physics. Formulated by G. Glashow, S. Weinberg and A. Salam in 1967, it consists of three generations of quarks and leptons. The

fundamental forces of nature - Electromagnetic, Strong and Weak are mediated by their corresponding gauge bosons. Gravity is not included. It is illustrated in Figure 1.1. Particles obtain their mass through the Higgs mechanism developed in 1964 by P. W. Higgs [23], F. Englert and R. Brout [24], and G. S. Guralnik, C. R. Hagen and T. W. B. Kibble [25] - the field quanta being the Higgs boson.

In the standard model, the neutrino is considered to be massless. It is an elegant theory which has stood the test of time. All the particles predicted by the SM have been observed, the recent one being the 'Higgs boson' discovered by the ATLAS [26] and CMS [27] collaborations at the Large Hadron Collider (LHC), CERN.
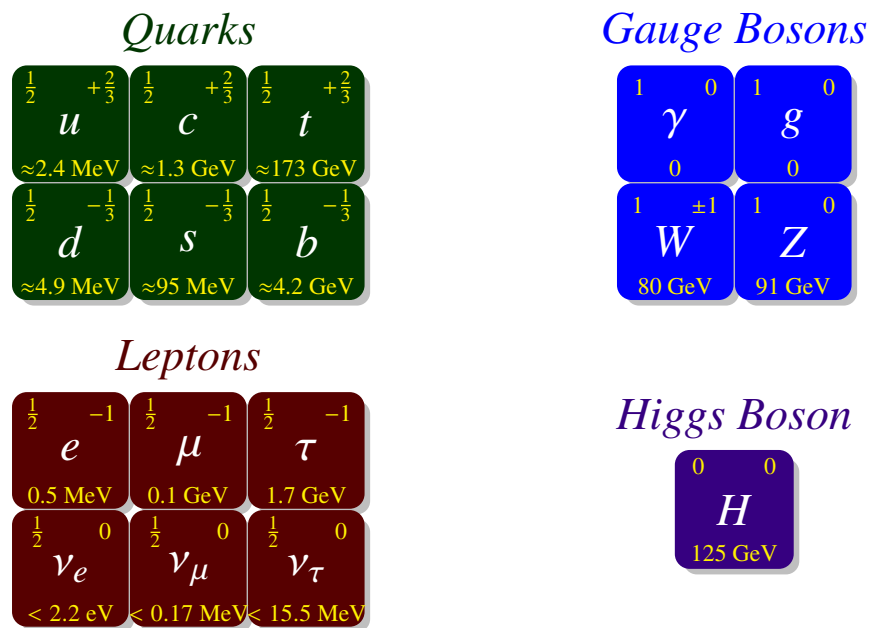
FIGURE 1.1: The standard model of particle physics (Key: Top left corner - spin, top right corner - charge, center - particle, bottom center - mass.).

1.1.2 Solar neutrino anomaly

The sun generates energy by fusing hydrogen atoms to produce He. Thermo nuclear fusion process in the sun can be expressed by the reaction

$$4p \rightarrow {}^{4}_{2}\text{He} + 2e^{+} + 2\nu_{e} \tag{1.3}$$

which had been known for quite sometime from the first half of the twentieth century. An enormous number of neutrinos are emitted from the core of the sun. R. Davis Jr. and J. Bahcall proposed an experiment in 1964 to observe these neutrinos by using a large detector made of perchloroethylene (C_2Cl_4) - a cleaning liquid. Neutrinos interacting with the chlorine atoms would convert ^{37}Cl to ^{37}Ar.

$$^{37}\text{Cl} + \nu_e \rightarrow {}^{37}\text{Ar} + e^- \tag{1.4}$$

The number of ^{37}Ar atoms one would expect to be produced could be calculated. A detector with a cylindrical steel tank, 6 m in diameter and 15 m long, containing around 400 000 L of C_2Cl_4 was constructed at the Homestake Gold Mine in Lead, South Dakota, USA. When the first results were obtained in 1968, it was seen that only one third of the expected number of neutrinos were detected. This discrepancy in the expected to detected number of neutrinos from the sun came to be known as the 'Solar Neutrino Anomaly'.

About 2 decades later, in 1989, the Kamiokande detector was built by the Japanese-American collaboration to find evidences for proton decay. The detector was made up of 3000 t of water in a cylindrical tank observed by about 1000 photo-multipliers. Though the detector was made for proton decay, it had the capability to observe neutrinos, when electrons scattered by them emitted

Cerenkov light. The detector was more sensitive to higher energy solar neutrinos produced in the decay ^{8}B nucleus during the fusion cycle. They were able to observe only half the number of predicted solar neutrinos although not the same as the homestake experiment but in support of the anomaly.

Other experiments whose results were in support of this anomaly were GALLEX [28] and SAGE [29].

1.1.3   Atmospheric neutrino anomaly

Due to the development of Grand Unified Theories, certain exotic phenomena such as the proton decay became a possibility. In the 1980's many experiments were built around the world to find evidence for it. The theoretical limit for the process at that time suggested the construction of huge detectors with proton rich materials such as water. The Kamiokande at Japan and IMB (Irvine-Michigan-Brookhaven) in the USA were two such experiments.

Both Kamiokande and IMB utilized the principle of Cerenkov radiation to detect neutrinos. For charged particle decays in cosmic rays, ν_μ/ν_e i.e. the ratio of number of muon neutrinos (anti-neutrinos) to number of electron neutrinos (anti-neutrinos) is around 2 up to around 1 GeV and increases with energy further. This fact is established by independent theoretical calculations.

Kamiokande and IMB both observed a reduction in the number of μ like events in their detectors and hence the ratio was lesser than expected. This deficit came to be known as the 'Atmospheric Neutrino Anomaly'.

However, two other contemporary experiments NUSEX [30] and Frejus [31] which utilized different technique of detection - iron plates and particle counters

- did not observe any reduction in the ratio.

Both the solar and atmospheric neutrino anomalies gave hint to new physics. Neutrino oscillation theory seemed to be the possible explanation to these anomalies.

1.1.4   Neutrino oscillations

Around the year 1991, the construction of a bigger and advanced version of the Kamiokande detector called the Super Kamiokande (Super-K) began in Japan. It took five years for the construction of the detector and data taking started in 1996. Super-K was a water Cerenkov detector having a diameter of 39.3 m and height of 41.4 m. It contained 50 kt of ultra-pure water.

After analysis of two years of data, in 1998, the Super-K collaboration confirmed the atmospheric neutrino anomaly reported by the previous Kamiokande, IMB and Soudan-2 [32] experiments.

Cosmic ray interactions in the atmosphere all around the earth is uniform. In an underground experiment such as Kamiokande or IMB, one expects the number of upward going neutrinos - neutrinos produced in the atmosphere on the other side of the earth reaching the detector after passing through the earth - to be same as those produced in the atmosphere over ground. The zenith angle dependence should be uniform. It was shown in their analysis that the ratio of the up going muon neutrinos to the downward going muon neutrinos was ~0.5. Previous results with Kamiokande was not conclusive enough.

In 1999, the SNO [33] detector began taking data at the Sudbury Neutrino Observatory. It was a spherical detector filled with 1000 t of heavy water (D_2O),

observed by ~10000 PMTs of 20 cm diameter. This detector had the capability to observe three different types of neutrino interactions - elastic scattering (ES), Charge Current scattering (CC) and Neutral current scattering (NC).

$$\nu_x + e^- \rightarrow \nu_x + e^- \quad (ES)$$
$$\nu_e + d \rightarrow e^- + p + p \quad (CC) \qquad (1.5)$$
$$\nu_x + d \rightarrow \nu_x + n + p \quad (NC)$$

Among reactions in (1.5) the CC reaction is only sensitive to electron neutrinos, whereas the NC reactions are sensitive to all flavors and ES reactions are mostly sensitive to electron neutrinos.

In 2001, with their first results [34], the SNO collaboration confirmed the phenomenon of neutrino oscillation. The data on solar neutrino oscillations from Super-K also supported the deficit of the solar neutrinos. In 2004, Super-K collaboration observed a clear wave like pattern in their data of atmospheric neutrinos confirming the oscillations. After these results many experiments have shown clear evidence for neutrino oscillation, T2K, MINOS - accelerator based oscillation experiments [35, 36], Daya Bay, Double CHOOZ and RENO - reactor based experiments which did the precision measurement of the mixing angle θ_{13} [37, 38, 39], to name a few. The phenomenon of neutrino oscillation which requires neutrinos to be massive, shows that neutrinos do possess mass.

The theory of neutrino oscillation was first formulated by B. Pontecorvo in the 1950s between electron neutrinos drawing analogy to the $K^0 \rightarrow \bar{K}^0$ oscillations observed in cosmic rays. At that time, only one flavour of neutrino (ν_e) was known. After the discovery of the muon and the muon neutrino, he extended the theory to include two flavors and also between right handed states (Now known

as sterile neutrinos) in 1967 [40] (Translated from Russian). It is interesting to note that Pontecorvo had predicted that half the number of solar neutrinos would be observed before the publication of the results of Davis' experiment. Independently in 1962, Z. Maki, M. Nakagawa and S. Sakata defined the concept using a different model where they discussed oscillations between muon and electron neutrino flavours [41].

The comprehensive phenomenological theory of neutrino oscillations took shape in the 1970's due to the work of B. Pontecorvo, Z. Maki, M. Nakagawa, S. Sakata, J. Bahcall, S. Frautschi, H. Fritsch, P. Minkowski, S. Elizer and A. Swift [40, 41, 42, 43, 44]. Neutrino mixing became similar to quark mixing in the hadron sector.

According to the theory of neutrino oscillation, neutrino in the flavor basis can be represented using the mass basis as

$$|\nu_l\rangle = \sum_i U_{li}^* |\nu_i\rangle \tag{1.6}$$

where, $l = e, \mu, \tau$ are the three neutrino flavors and $i = 1, 2, 3$ are the mass eigen states.

$$U = \begin{bmatrix} c_{12}c_{13} & s_{12}c_{13} & s_{13}e^{-i\delta_{13}} \\ -s_{12}c_{23} - c_{12}s_{23}s_{13}e^{i\delta_{13}} & c_{12}c_{23} - s_{12}s_{23}s_{13}e^{i\delta_{13}} & s_{23}c_{13} \\ s_{12}s_{23} - c_{12}c_{23}s_{13}e^{i\delta_{13}} & -c_{12}s_{23} - s_{12}c_{23}s_{13}e^{i\delta_{13}} & c_{23}c_{13} \end{bmatrix}$$

$$\times \text{diag}(e^{i\lambda_1}, e^{i\lambda_2}, e^{i\lambda_3}) \tag{1.7}$$

where, $c_{ab} = \cos\theta_{ab}, s_{ab} = \sin\theta_{ab}, \theta_{13}, \theta_{23}, \theta_{12}$ are the mixing angles, δ_{13} is the Dirac phase which characterizes CP violation (Charge-Parity) and λ_i are the Majorana phases. The Majorana phases are relevant only if neutrinos are Majorana particles.

The matrix U is known as the PMNS matrix in honor of B. Pontecorvo, Z. Maki, M. Nakagawa and S. Sakata.

The oscillation probability for a neutrino oscillating from one flavor to the other is given by

$$
\begin{aligned}
P_{\nu_\alpha \to \nu_\beta}(L, E) = \delta_{\alpha\beta} &- 4 \sum_{k>j} \Re[U^*_{\alpha k} U_{\beta k} U_{\alpha j} U^*_{\beta j}] \sin^2\left(1.27 \frac{\Delta m^2_{kj} L}{E}\right) \\
&+ 2 \sum_{k>j} \Im[U^*_{\alpha k} U_{\beta k} U_{\alpha j} U^*_{\beta j}] \sin^2\left(2.54 \frac{\Delta m^2_{kj} L}{E}\right)
\end{aligned}
\tag{1.8}
$$

For the anti-neutrino case it is given by

$$
\begin{aligned}
P_{\nu_\alpha \to \nu_\beta}(L, E) = \delta_{\alpha\beta} &- 4 \sum_{k>j} \Re[U^*_{\alpha k} U_{\beta k} U_{\alpha j} U^*_{\beta j}] \sin^2\left(1.27 \frac{\Delta m^2_{kj} L}{E}\right) \\
&- 2 \sum_{k>j} \Im[U^*_{\alpha k} U_{\beta k} U_{\alpha j} U^*_{\beta j}] \sin^2\left(2.54 \frac{\Delta m^2_{kj} L}{E}\right).
\end{aligned}
\tag{1.9}
$$

where E is the energy of the neutrino in MeV(GeV), L is the distance from the source to the detector in m(km) and $\Delta m^2_{kj} = m^2_j - m^2_k$ is the mass squared difference in eV^2. The ultra-relativistic approximation has been used while arriving at the above relations i.e. $E_j = \sqrt{p_j^2 + m_j^2} \approx p_j + m_j^2/2p_j \approx E + m_j^2/2E$ where, E is the total energy of the neutrino, E_j, p_i and m_j are the energy, momentum and mass of the jth mass eigen state respectively.

1.1.5   Two neutrino mixing

Most neutrino experiments are insensitive to the influence of three neutrino mixing. So, an effective model with two neutrino mixing can be used. Two flavor neutrinos are considered, ν_α, ν_β can be pure flavors ($\alpha, \beta = e, \mu$ or $\alpha, \beta = e, \tau$ or $\alpha, \beta = \mu, \tau$) or linear combinations of pure flavors ($\nu_\alpha = \nu_e$ and $\nu_\beta = c_\mu \nu_\mu + c_\tau \nu_\tau$

$(c_\mu^2 + c_\tau^2 = 1)$ in case of electron neutrino disappearance experiments or $\nu_e \to \nu_{\mu,\tau}$ in experiments where ν_μ and ν_τ are not distinguishable)[45].

The effective mixing matrix in such a case can be written as

$$U = \begin{bmatrix} \cos\vartheta & \sin\vartheta \\ -\sin\vartheta & \cos\vartheta \end{bmatrix} \tag{1.10}$$

where, ϑ is the mixing angle.

The neutrino oscillation and survival probabilities are given by

$$\begin{aligned} P_{\nu_\alpha \to \nu_\beta}(L,E) &= \sin^2 2\vartheta \, \sin^2\left(1.27\frac{\Delta m^2 L}{E}\right) \quad (\alpha \neq \beta) \\ P_{\nu_\alpha \to \nu_\alpha}(L,E) &= 1 - \sin^2 2\vartheta \, \sin^2\left(1.27\frac{\Delta m^2 L}{E}\right). \end{aligned} \tag{1.11}$$

Here, ν_α, ν_β are the flavor eigen states and $\Delta m^2 \equiv \Delta m_{21}^2 = m_2^2 - m_1^2$ is the mass squared difference between the mass eigen states ν_2, ν_1. The probabilities defined so far are known as 'Vacuum oscillation probabilities'.

Matter effects

In 1978, L. Wolfenstein [46] showed that neutrinos propagating in matter are influenced by a potential due to coherent forward elastic scattering with the particles in the medium (electrons and nucleons). The mixing angle (vacuum) could be substituted by an effective mixing angle leading to enhanced oscillations even if the vacuum mixing angle is small. In the year 1985, S. P. Mikheev and A. Yu. Smirnov [47] found out that there could be resonant flavor transitions when neutrinos propagated in matter with varying density. Together, this effect came to be known as the *MSW effect* and provided an explanation for the large oscillation seen in the solar neutrino sector. In the two neutrino case for a material medium, the mixing matrix would be given by [45]

$$U_{\mathrm{M}} = \begin{bmatrix} \cos \vartheta_{\mathrm{M}} & \sin \vartheta_{\mathrm{M}} \\ -\sin \vartheta_{\mathrm{M}} & \cos \vartheta_{\mathrm{M}} \end{bmatrix} \tag{1.12}$$

where, ϑ_{M} is the effective mixing angle given by

$$\tan 2\vartheta_{\mathrm{M}} = \frac{\tan 2\vartheta}{1 - \dfrac{A_{\mathrm{CC}}}{\Delta m^2 \cos 2\vartheta}} \tag{1.13}$$

and

$$\Delta m_M^2 = \sqrt{(\Delta m^2 \cos 2\vartheta - A_{\mathrm{CC}})^2 + (\Delta m^2 \sin^2 2\vartheta)^2}. \tag{1.14}$$

Here, Δm_M^2 is the effective mass difference, $\vartheta, \Delta m^2$ are the mixing angle, mass squared difference in vacuum and $A_{\mathrm{CC}} = 2\sqrt{2}EG_{\mathrm{F}}N_e$ is term related to the matter potential. G_F is the Fermi's coupling constant and N_e is the electron density. $A_{\mathrm{CC}} = \Delta m^2 \sin^2 2\vartheta$ is the condition for resonance, where $\vartheta_{\mathrm{M}} = \pi/4$ becomes maximal leading to resonant flavor transitions.

1.1.6   Neutrino - Majorana and Dirac

If a fermion is its own antiparticle, it is known as a Majorana particle. Normal fermions are called Dirac particles. Only neutral particles can be Majorana, otherwise they would violate charge conservation. In 1937, E. Majorana showed that beta decay could be explained using an alternative approach where one need not have negative energy states as obtained by Dirac equation.

However, the problem with this approach was that the particle-antiparticle concept in the case of neutral fermions has to be put aside.

Neutrino oscillation experiments are not sensitive to the Majorana phases and hence cannot determine whether neutrinos are Majorana or not. In 1937, Racah
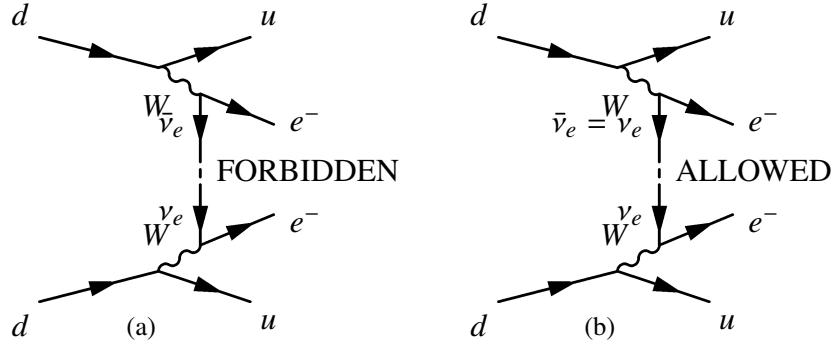
FIGURE 1.2: (a) Neutrinoless double beta decay in the Standard Model. (b) Neutrinoless Double Beta Decay for the Majorana case.

suggested reactions through which the majorana nature could be determined. In 1938, following Racah, Furry [48] for the first time discussed Neutrinoless Double Beta Decay.

Neutrinoless double beta decay $(2\beta_{0\nu})$ is a process which violates lepton number by 2 units. In this process, a neutrino emitted by a beta decaying nucleus is absorbed by a nucleon of the same nucleus emitting two beta particles. It is forbidden in the SM due to helicity and particle-antiparticle mismatch. The feynman diagrams for the processes are shown in Figure 1.2. The reaction can be written as

$$N(A,Z) \rightarrow N(A,Z+2) + 2e^-$$
$$N(A,Z) \rightarrow N(A,Z-2) + 2e^+$$

(1.15)

Hence, $2\beta_{0\nu}$ is one of the best method to probe the Majorana nature of neutrino. It can also give an idea about the absolute scale of the neutrino mass. Various experiments around the world are running or being planned for neutrinoless double beta decay [49, 50, 51, 52, 53].

1.1.7   Neutrino mass ordering

Neutrino flavor conversions can be explained using two sets of mass squared differences (Δm_{21}^2 and Δm_{31}^2), three mixing angles ($\theta_{12}, \theta_{13}, \theta_{23}$) and the Dirac CP-phase δ. The index on the mass eigen state is arbitrary. By convention the smaller of the two mass differences has $m_2 > m_1$ so that $\Delta m_{21}^2 > 0$. The mass squared difference Δm_{21}^2 has been measured and known to be positive by solar neutrino experiments. Two possibilities arise.

Normal Mass Ordering (NO) or hierarchy (NH): If $m_3 > m_2 > m_1$, then $\Delta m_{32}^2 > 0$.

Inverted Mass Ordering (IO) or hierarchy (IH): If $m_2 > m_1 > m_3$, then $\Delta m_{32}^2 < 0$.

The sign of Δm_{32}^2 (same as that of Δm_{31}^2) is not known. But it is known that $|\Delta m_{21}^2| \ll |\Delta m_{31(32)}^2|$ (See Ref. [54], Chapter 14). Therefore, in both the cases,

$$|\Delta m_{32}^2| \cong |\Delta m_{31}^2|, \quad |\Delta m_{31}^2 - \Delta m_{32}^2| = \Delta m_{21}^2 \ll |\Delta m_{31,32}^2|$$

The measurement of the sign of Δm_{32}^2 is therefore very crucial for the determination of neutrino mass ordering.

1.2   India-based Neutrino Observatory (INO)

India-based Neutrino Observatory (INO) is a proposed mega science project in India. It is to be setup under the Bodi West Hills near Pottipuram village, Theni district, Tamil Nadu in South India. Constructed under the mountain, it will have

a rock cover of at least 1 km or more on all the sides. It will be a world class observatory for performing low background experiments. Such a huge basic science project is being done for the first time in the country.

The magnetized ICAL (Iron CALorimeter) detector is one of the detectors to be housed at INO which will primarily study atmospheric neutrinos. The observatory will be constructed to support other rare event experiments such as neutrinoless double beta decay, dark matter search and low energy neutrino spectroscopy whose R & D activities are underway. Apart from these, such an environment can be used to do certain studies in Biology, Geology etc.

1.2.1 ICAL

The ICAL detector will have Resistive Plate Chambers (RPCs) as the main detector elements. It will have 151 alternating layers of iron plates and RPCs. The iron plates will be 5.6 cm thick and 4 cm of gap would be provided between them to place the RPCs. It will be constructed in 3 modules. The dimension of the detector including all 3 modules would be 48 m × 16 m × 14.5 m with a total mass of 50 kt. The parameters of the ICAL are summarized in Table 1.1. The mechanical/CAD drawing of ICAL is shown in Figure 1.3.

A magnetic field of ~1.5 T would be generated in the ICAL using copper coils. When fully constructed, the ICAL would be the largest electromagnet in the world.

RPCs having an efficiency of ~95 % for muons and time resolution of ~1 ns will provide the timing and position information of the particles generated by the interaction of atmospheric neutrinos with the iron plates. The cross section

TABLE 1.1: Parameters of the ICAL detector [1].

ICAL	
No. of modules	3
Module dimension	16 m × 16 m × 14.5 m
Detector dimension	48 m × 16 m × 14.5 m
No. of layers	151
Iron plate thickness	5.6 cm
Gap for RPC trays	4.0 cm
Magnetic field	1.5 T
RPC	
RPC unit dimension	2 m × 2 m
Readout strip width	3 cm
No. of RPC units /Layer/Module	64
Total no. of RPC units	∼ 30 000
No. of electronic readout channels	3.9×10^6

for the interaction of atmospheric neutrinos is ∼ 10^{-38} cm^2 [55]. 50 kt of iron serves two purposes: (1) Furnishing plenty of nuclei for neutrino interaction and (2) Providing sufficient magnetic flux density to bend muons generated after neutrino interaction. Using the tracks of the particles in presence of the strong magnetic field energy information will be obtained.

TABLE 1.2: Current oscillation parameter best fit values [1].

Parameter	Best fit values	3σ ranges
Δm_{21}^2 (eV^2)	7.5×10^{-5}	$[7.0, 8.1] \times 10^{-5}$
Δm_{31}^2 (eV^2)	2.46×10^{-3} (NH)	$[2.32, 2.61] \times 10^{-3}$ (NH)
Δm_{32}^2 (eV^2)	-2.45×10^{-5} (IH)	$-[2.59, 2.31] \times 10^{-3}$ (IH)
$\sin^2 \theta_{12}$	0.3	$[0.27, 0.34]$
$\sin^2 \theta_{23}$	0.45 (NH), 0.58 (IH)	$[0.38, 0.64]$
$\sin^2 \theta_{13}$	0.022	$[0.018, 0.025]$
$\delta_{CP}(^\circ)$	306	$[0, 360]$

The best fit values of the current oscillation parameters are listed in Table 1.2. The principal aims of ICAL are
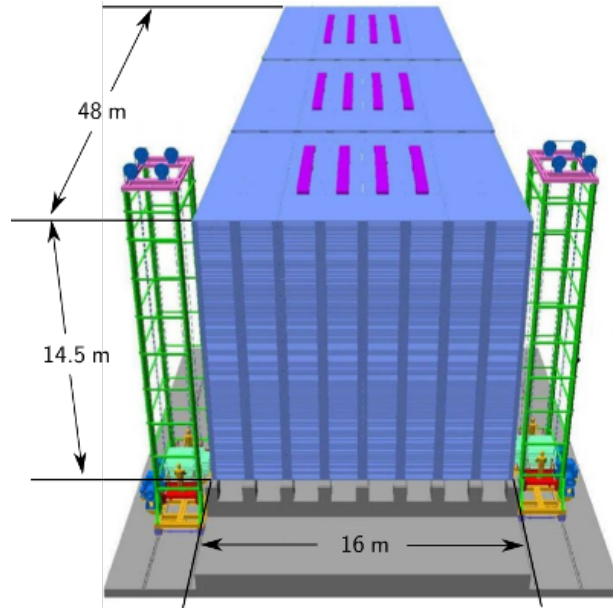
FIGURE 1.3: Mechanical/CAD drawing of the proposed ICAL detector.

1. Determination of neutrino mass ordering or hierarchy.

2. Determine the deviation of θ_{23} from the maximal value and its correct octant.

3. Explore CP violation in the lepton sector.

Many experiments around the world under operation, construction or planning like NOνA [56], Hyper-K [57], PINGU [58], LBNE [59], LBNO [60], JUNO [61], T2K [62], T2HK [57] etc., share one or more goals with the ICAL. Due to its magnetic field ICAL can distinguish neutrinos and anti-neutrinos - a feature not available in the case of water Cerenkov experiments. Using the earth's matter effect, ICAL can also perform complementary measurements of θ_{13} with the ongoing reactor and accelerator experiments. Synergy of ICAL with

some of the experiments above will improve the global reach to the oscillation parameters.

Studies have and are being performed to explore ICAL's ability to do new physics. These include high energy muons, long range forces, CPT violation, and non-standard interactions (NSI) (See Ref. [1], and references therein).

1.3 Are there more number of neutrinos?

The invisible decay width of the Z boson measured at the LEP collider at CERN [63, 64, 65, 66] indicates that there can be 3 neutrino flavors. Fit to the average data of ALEPH, DELPHI, L3 and OPAL measurements is best when 3 flavors are used. It is shown in Figure 1.4.
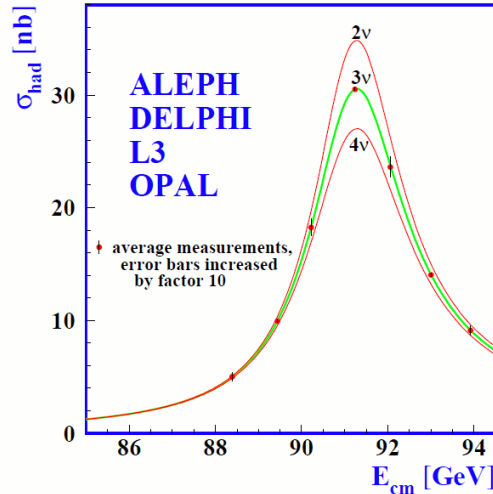
FIGURE 1.4: Invisible width of the Z boson. Figure from [67].

This data constrains the number of active flavors to 3. If there are more, they should be very heavy. In the LSND experiment, electron neutrinos were observed in a pure muon neutrino beam [68]. The data could be explained only

with a mass square difference of $\Delta m^2 \sim 1$ eV^2. Such a large mass squared differ-ence is not possible among active neutrinos as seen in Table 1.2. It would require a fourth neutrino. Since the Z boson width shows that the number of neutrinos are three, the fourth neutrino should be sterile.

Sterile neutrino

A sterile neutrino is a neutrino which has no interactions except through mixing with active flavors and gravity. They appear in many theories - Neutrino Minimal Standard Model (νMSM), sterile neutrino dark matter, split seesaw mechanism, etc. In the standard model, right handed neutrinos or left handed anti-neutrinos do not take part in weak interactions. They are regarded as sterile. There could be 1, 2 or more sterile neutrinos. According to theories, at least one of them can be light.

Data in support of the sterile neutrino first came from the LSND experiment as mentioned before. MiniBOONE experiment did not see the excess in their muon neutrino beam. However, they observed an excess in the case of muon anti-neutrinos [69] in support of the LSND result. Also in the Gallium experi-ments strong sources of electron neutrinos were used for calibration such as ^{51}Cr and ^{37}Ar (both decay by electron capture). Both the source strength and cross sections were known to some precision. But, a deficit was observed in the mea-sured to expected count rate (See Ref. [70], Chapter III). A possible explanation is a sterile neutrino with $\Delta m^2_{\text{sterile}} > 1$ eV^2.

Another phenomenon in support of sterile hypothesis is the recent Reactor Anti-neutrino Anomaly (RAA).

1.3.1   Reactor Anti-neutrino Anomaly - Another anomaly?

In 2011, the group of the Double CHOOZ experiment re-evaluated the neutrino flux expected from reactors. They found the number of neutrinos expected from nuclear reactors to be 3.5% more than what was calculated before [7, 8]. A reanalysis of the data of all reactor anti-neutrino experiments performed at distances <100 m was done. The ratio of expected to detected neutrino deviated from unity with a value $R = 0.943 \pm 0.022$ at a confidence level of 3σ. It has been termed as the 'Reactor Anti-neutrino Anomaly' [9].

This anomaly may be due to something related to reactor systematics or some unknown physical phenomena. If it is not due to the former, then, RAA cannot be understood within the 3 neutrino framework. However, if a fourth flavor known as the sterile neutrino exists, and is postulated to mix with $\bar{\nu}_e$, then the deficit in their measured number at short distances can be understood.

1.4   Reactor monitoring and sterile neutrino search

The fission processes happening in the reactor produce numerous radioactive isotopes whose β decay produce electron anti-neutrinos. A 1 GW$_{th}$ reactor produces roughly 1.5×10^{20} neutrinos per second. Around six anti-neutrinos per fission. Flux is a drawback for experiments which rely on cosmic sources such as the Super-K, INO, etc. Reactors are indeed one of the best sources to study neutrinos. The flux falls by the inverse square law. So, the time the experiment will have to take data will depend on the distance from the source and statistics

needed. The energy averaged interaction cross section of anti-neutrinos from reactors is of the order of 10^{-43} cm^2.

1.4.1 Reactor Monitoring

In a nuclear reactor, the isotopes of Uranium and Plutonium undergo fission following the absorption of predominantly thermal neutrons. Electron anti-neutrinos are emitted from the decay chains of fission products of Uranium(U) and Plutonium(Pu). Major contribution to the thermal power and the emitted anti-neutrinos comes from the fission of ^{235}U and ^{239}Pu isotopes. ^{235}U, ^{239}Pu, ^{238}U, ^{241}Pu together contribute 99.9 % of the total thermal power [71]. Inverse neutron beta decay reaction

$$\bar{\nu}_e + p \rightarrow n + e^+ \tag{1.16}$$

was used to detect anti-neutrinos for the first time and is still used in various reactor anti-neutrino experiments [72].

Due to the "Burnup effect", as the reactor operates, the number of anti-neutrinos emitted will decrease over time due to the formation of ^{239}Pu as ^{235}U gets consumed. The number of anti-neutrinos that can be detected is given by the expression

$$N_{\bar{\nu}_e} = \gamma(1 + k)P_{\text{th}} \tag{1.17}$$

where γ is a constant which depends on the detector and the geometry, P_{th} is the thermal power and k is the fuel composition which evolves with time [73]. It is possible to monitor reactors remotely utilizing the difference in the energy spectrum of neutrinos emitted by the fissioning isotopes (^{235}U and ^{239}Pu) in a reactor. The concept of utilizing this change in the flux of emitted anti-neutrinos to mon-

itor and estimate the burn-up and composition of fuel of a reactor remotely was proposed by Mikaélyan in the 1970s and was demonstrated first by experiments at Rovno reactor in USSR in the late 1980s [2]. A few years ago, it was also demonstrated through the results of the SONGS experiment [74].

IAEA (International Atomic Energy Agency), the UN body for peaceful use of Nuclear Energy has shown interest in the neutrino method as a new safeguards method to check nuclear proliferation.

1.4.2   Sterile Neutrino Physics

Apart from reactor monitoring these detectors can be used to investigate the RAA described in Section 1.3.1. Experiments at very short baselines of tens of meters can determine the existence of the sterile neutrino or help improve our understanding of reactor physics. The electron anti-neutrino survival probability in the two flavor scenario is given by

$$P_{ee} = 1 - \sin^2(2\theta_{\text{new}}) \sin^2 \left(1.27\frac{\Delta m^2_{\text{new}}L}{E_{\bar{\nu}_e}}\right) \tag{1.18}$$

where, θ_{new} is the mixing angle, $E_{\bar{\nu}_e}$ is the energy of the electron anti-neutrino, L is the source to detector distance and Δm^2_{new} is the mass squared difference. To observe oscillation at such short distances, the mass squared difference Δm^2_{new} should be ~ 1 eV^2 [70].

Since reactors are a copious source of anti-neutrinos, a modestly sized detector (~ 1 t) is sufficient for sterile neutrino mixing studies and reactor monitoring to be carried out on a reasonable amount of time.

1.4.3 India's Scintillator Matrix for Reactor AntiNeutrino (ISMRAN)

It has been proposed to setup a detector of mass 1 t for studies related to reactor monitoring and possible sterile neutrino physics at the Dhruva research reactor facility at Bhabha Atomic Research Centre (BARC), Trombay, India.

Similar to the PANDA experiment [11], the proposed design consists of 100 plastic scintillator bars of $(100 \times 10 \times 10)$ cm^3 dimension. Each bar is coupled to two 3″ photo-multipliers. The bars are arranged in a way so that a cube of 1 m^3 volume is formed. The detector will be hermetically shielded by Lead $\geq$ 10 cm, borated polyethylene (50% boron) ~10 cm from inside to outside. Muon veto detectors made of plastic scintillators would be place outside the shielding hermetically to veto events due to muon interaction in the core detector. The engineering drawing of ISMRAN being designed by Centre for Design and Manufacture (CDM), BARC is shown in Figure 1.5. ISMRAN will utilize the
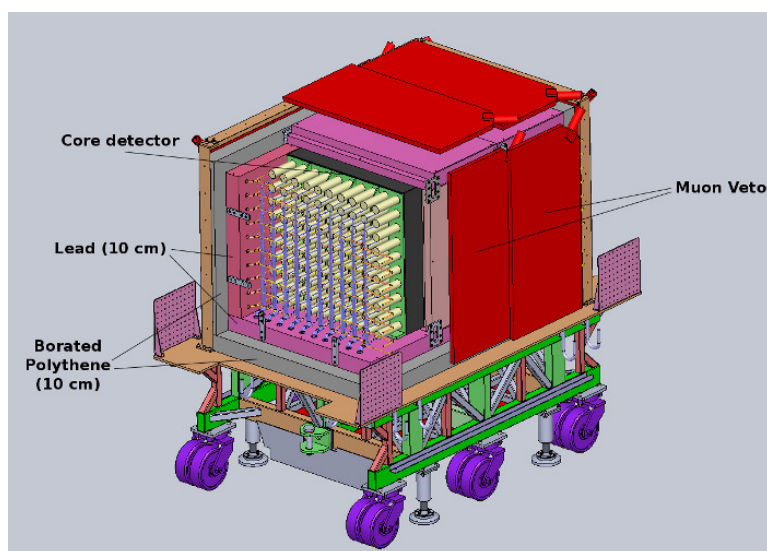
FIGURE 1.5: Engineering drawing of ISMRAN with shielding and trolley.

inverse neutron beta decay reaction (1.16) to detect anti-neutrinos. A neutrino signature would be the correlated signal from positron and neutron. The prompt event will be due to the energy deposited by the positron and gamma produced after its annihilation. The delayed event would be from the radiative capture of the neutron. For effective capture of neutron each bar would be wrapped by a Gd_2O_3 coated aluminized mylar foil having a density of 4.8 mg/cm^2. Gd has a large cross section for thermal neutron capture. A cascade of gamma rays up to a total energy of ~8 MeV would be emitted after the capture of a neutron. Reaction (1.16) is a very strong method of detecting anti-neutrinos and requires detectors rich in free protons. Hence an organic scintillator based detector is the best choice.

Due to the continuous energy spectrum of the anti-neutrinos emitted from reactors, the oscillation minima are expected to occur at distances <10 m from the reactor (See, Ref. [70], Section III). Right now, the place that has been allotted to the experiment at the reactor site is ~13 m far from the reactor core. VME digitizer based acquisition system will be employed reducing the bulk of electronics.

Data on sterile neutrino that currently exists from various experiments is only based on count rates. The effect of distance on the oscillation has to be observed. The core detector with shielding would be mounted on a trolley so that data can be taken at different source to detector distances.

Shielding design shown in Figure 1.5 is in the evaluation stage. Permission to proceed with the order for the required lead and borated polyethylene is awaited. A prototype with 20 scintillator bars of $(100 \times 10 \times 10)$ cm^3 dimension each (20% of the proposed detector) called 'Mini-ISMRAN' will be setup at the

allotted place in the reactor hall.

1.5 Summary

The Standard Model of particle physics is an elegant theory which has stood the test of time. All the particles predicted by it have been discovered. However, due to the elusive neutrino's peculiar behavior, it has now come to light that neutrinos have mass and oscillate between flavors as they propagate. The determination of their mass and precision measurement of oscillation parameters have great impact on our understanding about nature. The journey to the discovery of neutrino oscillation and interesting physics related to neutrino have been explained briefly.

The proposed INO (India-based Neutrino Observatory) is an ambitious mega science project of India to setup a world class underground laboratory for doing rare event studies in South India. A 50 kt magnetized Iron CALorimeter (ICAL) will be setup in this laboratory to do precision measurement of oscillation parameters using atmospheric neutrinos and throw light on questions such as the mass ordering of neutrinos and CP violation in the lepton sector. This detector would be employing ~30000 RPCs as detector elements (Larger than the total number of RPCs used in various experiments around the world!). It would be the largest electromagnet in the world when fully constructed. R & D activities related to detectors, engineering and phenomenology are underway.

The idea of using anti-neutrinos generated in nuclear reactors to determine the state of fuel burn-up existed from the 1970s. Experiments around the world were done to exploit this idea. A successful demonstration to pave the way

for commercial use still needs lot of work. This idea is exciting since the elusive neutrino finds application and moreover, non intrusive remote reactor monitoring can be performed. Nuclear proliferation can also be checked.

Due to interesting data from experiments and observation of anomalies such as the Reactor Anti-neutrino Anomaly, the existence of a sterile neutrino is a possibility. Detectors designed for monitoring purposes can double up for detection of the sterile neutrino. This is due to the very short source to detector distance (~10 m) needed to perform these experiments. In this direction, a detector of mass 1 t has been proposed at the research reactor facility at BARC to do research on reactor monitoring technology and sterile neutrino physics.

The proposed detector called ISMRAN consists of 100 plastic scintillator bars of dimension $(10 \times 10 \times 100)$ cm^3, each coupled to two photo-multipliers. Each bar would be wrapped by Gd_2O_3 coated aluminized mylar foil to facilitate neutron capture. The bars will be arranged so as to form a cube of dimension 1 m^3. The detector along with hermetic shielding (lead, borated polythene and muon veto) will be kept at a distance of ~10 m from the reactor.∎

The thesis has been divided into two parts. The first part with a brief introduction on gas detectors and RPCs, describes the studies done on glass RPCs for ICAL detector at INO. The second part discusses simulations done to compare liquid and plastic scintillation detectors for reactor monitoring and sterile neutrino search. It also discusses some preliminary background measurements done at the reactor site. The thesis is basically on detector studies for two kind of neutrino experiments - Atmospheric and Reactor.

Part I

Studies on Resistive Plate

Chambers (RPC) for INO

Resistive Plate Chambers

Of the various particle detectors that exist today gaseous detectors are one of the easiest to construct but difficult to maintain with consistency. The discovery of the electron by J. J. Thomson was through a discharge tube which is a form of a gas detector.

2.1 Gas detectors

The general principle of detection in gaseous detectors is the collection of free charges created by the ionization of gas subjected to an electric field by incident radiation. Electrons after ionization by the incident radiation will multiply and form avalanches if the electric field is high enough. If the field applied is even higher, streamers and sparks are created.

Some important and familiar gas detectors are described briefly before discussing the RPC. The features of the gas detectors are explained so that the advantages and disadvantages of RPCs can be understood when compared to them.

Since the electric field is directly proportional to the applied voltage, gas detectors can be operated under different modes. The general classification is shown in Figure 2.1.
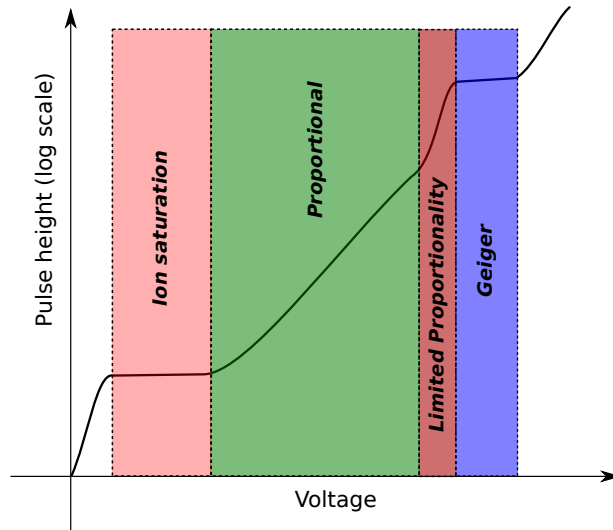
FIGURE 2.1: Gas detector operating regions.

Ionization Chamber

It is the simplest of gas detectors. It contains two electrodes namely the anode and the cathode and detection of charged particles is through the direct collection of charges created by the ionizing radiation. They operate in the ion saturation region shown in Figure 2.1 and can have various geometries like planar, cylindrical, grid etc. They are suitable for detecting low energy particles such as gamma, X-ray, neutrons and charged ions. Ionization chambers are usually operated in the current mode where the signal is the current measured in the external circuit - an indication of the rate of formation of charges by ionization in the detector. They can also be operated in the pulse mode when information about the energy
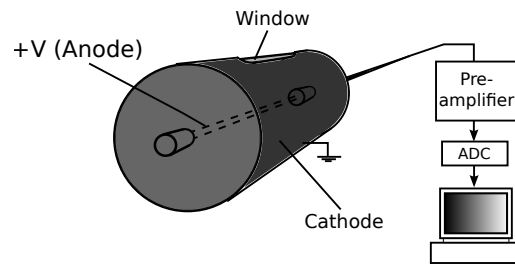
FIGURE 2.2: Illustration of the proportional counter.

of the incident radiation is needed. They are good detectors for dose measurements.

They require sophisticated electrometer circuitry. Noise becomes a problem when operating in the pulse mode.

Proportional counter

In its simplest construction, the proportional counter consists of a central anode wire surrounded by a cylindrical cathode. They are operated at a slightly higher voltage compared to the ion chambers so that avalanches are generated near the anode wire. The primary ion pair created by the incident radiation, in the presence of higher electric field cause further ionization and generates more ion electron pairs - charge multiplication. This multiplication eventually turns into an avalanche and the signal is proportional to the energy deposited by the incident radiation. Hence the name 'Proportional counter'. Its region of operation is the proportional region shown in Figure 2.1. Proportional Counters can be used for energy spectroscopy and particle discrimination.

Maintaining the tension of the anode wires is difficult. Also, material deposition may occur on the wires decreasing its efficiency over time.

GM counter

The GM counter or Geiger-Muller counter is similar in construction to the proportional counter. The difference lies in the choice of fill gas and the region of operation. It operates at an even higher voltage compared to the proportional counter as shown in Figure 2.1. Avalanche created by the primary ion pair release UV photons by ion recombination and multiple avalanches are created in the vicinity of the primary avalanche. A large current is generated. Signal is quite large and minimal processing electronics are required. They are suitable for radiation monitoring.

The signal does not possess any information of the energy deposited by the incident radiation. Hence it cannot be used for spectroscopic applications. Due to its dead time, it cannot be used in a high count rate environment.

Multi-Wire Proportional Chamber (MWPC)

To obtain both position and energy information of the incident radiation, MWPCs were developed by Georges Charpak at CERN. It is an extension of the proportional counter. Instead of a single wire, many thin wires are arranged parally in a form of a grid. The grid is symmetrically sandwiched by two plane electrodes. Any of the electrodes i.e. the wall or the wires is kept at a high voltage and the other is grounded. Like in the proportional counter, the radiation incident on the MWPC causes ionization in the gas or gas mixture and avalanche is generated close to the nearest wire. Using this information one can have the position information of the incident particle. Excellent position resolution of ~ 100 μm can be obtained using proper techniques.

Careful operation is needed. Due to the small spacing and high electric fields between wires, spark can be generated causing damage to the detector. Electronics need to have proper protection.∎

Gas detectors described above, mostly have one or more electrodes in the form of wires. Due to the radial dependence of the electric field, the timing performance of these detectors is average. Detectors with uniform electric fields can give better time resolution. Unlike the wire based detectors where the avalanche multiplication starts only near the vicinity of the wires, in a detector with parallel plate electrodes where the field is uniform, the avalanche multiplication starts immediately after the ionization of the gas mixture. Hence the timing performance of parallel plate detectors are better. Detectors with parallel electrodes were developed for this purpose.

Detectors which led to the development of the RPC were

Parallel Plate Counter (PPC)

The PPC [75] was a modified design of the GM counter to enable precise time measurements. It consisted of two metal electrodes spaced by a gap of around a few millimeter. Gas mixture would be flown inside the chamber at a low pressure. The detectors are operated in the streamer-spark regime. The response time of the detector is very fast. Remarkable time resolutions of few hundreds of picosecond can be obtained from these detectors.

They need an external quenching or switching off circuit to prevent it from going to the continuous discharge mode. Can only be used in low count rate experiments.

Planar Spark Chamber (PSC)

Around the 1970s, Pestov and group [76] reported the development of the Spark Counters with resistive electrodes which came to be known as Planar Spark Chamber or 'Pestov Counter'. One of the electrodes in this detector was made of semi conducting glass with bulk resistivity of $\sim 10^9 \Omega \cdot$cm. The advantage of this over the Parallel Plate counter was that, the resistive electrode provided a self quenching property to the detector. The discharge created by the incident radiation in the presence of electric field would be localized in an area of the order of the gap thickness. Only a small area of the counter would be rendered insensitive to the incident radiation. Detector dead time was reduced and the count rate handling capability increased maintaining the excellent timing characteristics. Time resolution of $\sim$25 ps is possible [77].

Gas has to be flown at a high pressure of around 1000-1200 hPa. Requires high mechanical precision in construction.

Resistive Plate Chamber (RPC)

RPC [3] was developed by R. Santonico and R. Cardarelli in the early '80s. It has a few simplifications compared to the PPC and the PSC. Both electrodes are resistive. They can be operated at normal atmospheric pressure. The coating of the conductive paint with a suitable resistivity allows capacitative coupling of readout to extract signals. Position information can be obtained and timing performance is very good.

The timing characteristics of the RPC in its usual construction is comparable to that of plastic scintillators. They provide a lower cost per channel. However,

they cannot provide energy information of the incident particle and are most suited for detecting MIP like muons, providing trigger and timing information. They can however be stacked in layers in an environment of high magnetic field to obtain energy of the incident radiation using the path and time information. Examples: CMS, ATLAS, INO etc.

Modifications of its design such as the multi-gap RPC can be used to obtain time resolutions of a few hundreds of picosecond.

2.2 Construction of RPC

An RPC consists of two planar electrodes made of resistive materials like bakelite or glass. The bulk resistivity of electrode varies from $10^{10} - 10^{12} \Omega \cdot$cm depending on the material. These electrodes are coated by a conductive paint like graphite for application of high voltage.

The electrodes are separated by a small gap of around 1 - 3 mm using cylindrical button spacers made of PVC or polycarbonate. The gap is filled by a suitable gas mixture. It is sealed from all the sides using edge spacers made of PVC or polycarbonate and nozzles are provided to enable gas flow. An illustration of the RPC is shown in Figure 2.3.
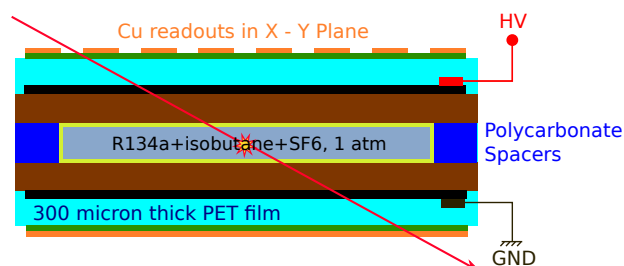
FIGURE 2.3: Illustration of the RPC.

To extract the signals, readouts made of copper strips are coupled capacitatively to the electrode using an insulator like a Mylar/PET sheet.

2.3   Signal production in RPC

The mean energy loss rate (MeV·g^{-1}·cm^2) or *mass stopping power*(MSP) for a charged particle passing through a medium is given by the Bethe-Bloch formula [54]

$$-\left\langle \frac{dE}{dx} \right\rangle = \frac{4\pi N_A r_e^2 m_e c^2}{A} z^2 \frac{Z}{\beta^2} \left[\frac{1}{2} \ln \frac{2m_e c^2 \beta^2 \gamma^2 W_{max}}{I^2} - \beta^2 - \frac{\delta(\beta\gamma)}{2} \right] \quad (2.1)$$

where,

$N_A = 6.02214129(27) \times 10^{23}$ mol^{-1} : Avogadro's number.

$r_e = 2.8179403267(27)$ fm : Classical electron radius.

Z : atomic number of the absorber.

A : atomic mass of the absorber (g·mol^{-1}).

z : charge number of the incident particle.

I : Mean excitation energy (eV).

W_{max} : Maximum energy transfer possible in a single collision.

$$W_{max} = \frac{2m_e c^2 \beta^2 \gamma^2}{1 + 2\gamma m_e/M + (m_e/M)^2}$$

$m_e c^2$: Electron mass (MeV/c^2).

M : Mass of the incident particle (MeV/c^2)

$\delta(\beta\gamma)$: Density effect correction to ionization energy loss.

$\beta = v/c$: where v is the velocity of the particle and c is the speed of light and $\gamma = 1/\sqrt{1 - \beta^2}$.

The MSP vs. the energy for some particles in a few materials is shown in Figure 2.4.
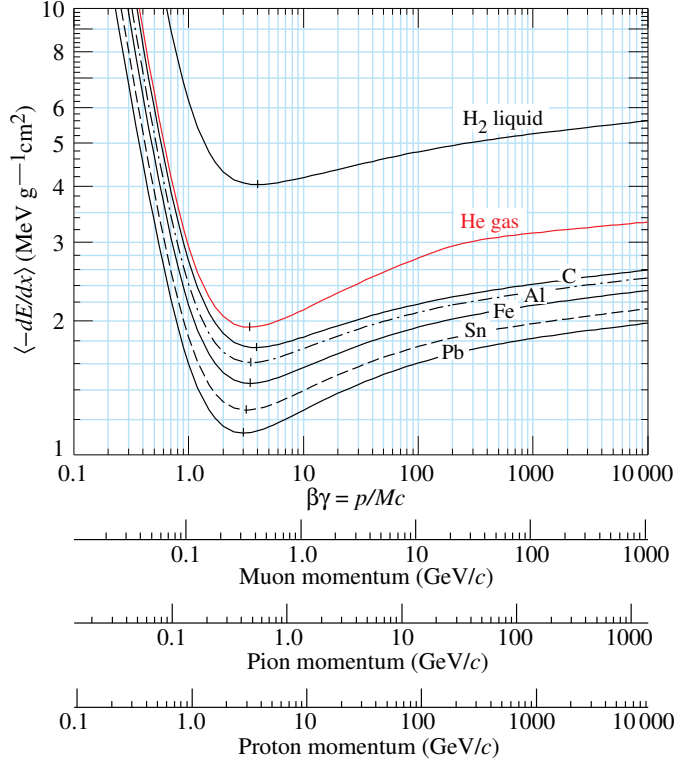
FIGURE 2.4: Mean energy loss rate $\langle -dE/dx \rangle$ for muon, pion and proton in few materials from [54]. Radiative corrections are not included.

When a charged particle enters the gas mixture in the RPC, it loses energy according to (2.1) and causes ionization and excitation of the molecules. The ionization can be due to the interaction of the electron of an atom with the coulomb field of the charged particle (distant) or due to the collision of the charged particle with the electron of the atom (close). If the atom is excited it may loose energy by emitting a photon or by emitting Auger electrons.

Signal in the RPC is through electron multiplication. As the incident particle passes through the gas mixture, primary electrons are created in clusters due to

ionization. In the presence of the high electric field, they drift towards the anode creating more electron and ion pairs. The avalanche formation in a gas detector can be explained through the Townsend's theory

$$n = n_0 \exp(\alpha - \beta)x \qquad (2.2)$$

where, n_0 is the number of electrons in the cluster, n is the number of electrons reaching the anode, α is the first Townsend coefficient which is the number of ionizations per unit length, β is the attachment coefficient which is the number of electrons captured by the gas molecules per unit length and x is the distance from the primary cluster to the anode. α and β are characteristic of the gases used. The gain is then the ratio $G = n/n_0$.

2.3.1 Modes of operation

RPCs can be operated in two modes

Avalanche : If the gas gain G is small ($< 10^8$), the Townsend avalanche formed is not capable of creating secondary avalanches. The signal strength of the RPC is quite low and low noise pre-amplification electronics are needed to utilize the signal without deteriorating the timing characteristics of the RPC. The area of the RPC which becomes insensitive to the incident radiation depends on the amount of charge that is produced in the gas. As the amount of charge generated is small, the RPC has good rate handling capability of ~1 kHz·cm^{-2}.

Streamer : If the voltage is increased, and gas gain $G > 10^8$ is obtained, photons created by excitation and recombination begin to contribute to the

multiplication process creating secondary avalanches. As a result a large current - streamer - is generated and a conductive channel is formed between the electrodes. The signal is quite strong and the RPC does not require any pre-amplification electronics. Due to the large amount of charge generated, dead time is more reducing the rate handling capability to $\sim$100 Hz$\cdot$cm^{-2}.

Table 2.1 shows the typical gas compositions used in RPCs operated in the avalanche and streamer modes.

TABLE 2.1: Typical gas mixture composition in RPCs.

Mode	Gas composition (%)			
	Argon	Freon-r134a	Iso-butane	SF$_6$
Avalanche	-	95.2	4.5	0.3
Streamer	30	60	8	2

2.3.2 Cluster density and gap thickness

Another important parameter of the fill gas is the cluster density denoted by $\bar{n}$. It defines the average number of primary ionizations caused by the incident particle. The timing performance of the RPC also depends on the gap thickness. The lower the thickness, better the timing; but, at the cost of signal strength. This makes it possible for the RPC to be optimized as a timing or trigger device by adjusting the gas composition and structural parameters.

For RPCs with small gap thickness (< 3 mm) gases with higher cluster density should be used so that sufficient primary clusters are created by the incident radiation for signal formation. The simulated values for cluster density of argon is around 2.5 mm^{-1} and freon is 5.5 mm^{-1} [78].

2.3.3   Role of the gases

Argon It is the main medium of interaction for incident radiation. It is used in RPCs operated in the streamer mode as shown in Table 2.1. Inert gas argon is usually used in gas detectors because, it is easily available, inexpensive, requires comparatively high ionization energy, and has good stopping power for incident radiation.

Freon-r134a It controls the avalanche development and is slightly electronegative. In the case of RPCs operating in the avalanche mode, Freon serves as the medium for the interaction of incident radiation.

It is to be noted that Freon-r134a is banned in the European union and would be phased out by 2017 due to its high Global Warming Potential (GWP) of ~1430. As ICAL would be running for around 20 years, an alternative gas having similar characteristics or freonless gas mixtures for RPCs must be explored. Efforts regarding this are already underway in the collaboration and around the world. A promising candidate as replacement for freon is 2,3,3,3-Tetrafluoropropene, or HFO-1234yf (GWP~4).

Iso-butane The signal ions and electrons created during ionization of predominantly freon may recombine and produce UV photons. These photons generate spurious pulses elsewhere in the detector. Iso-butane can absorb and convert the energy of the photons into vibrational states. Since iso-butane is a combustible gas, its concentration in the gas mixture always kept below the flammability limit.

SF_6 It is a strongly electronegative gas and helps in arresting the avalanche

development. It acts as a quenching gas and reduces the formation of streamers.

2.3.4 Bulk resistivity

The bulk resistivity of the electrodes plays a major role in the performance of the RPC. For glass the bulk resistivity ρ is $\sim 10^{12}\Omega$·cm and $\sim 10^{10}\Omega$·cm for bakelite. A charge Q_0 deposited on the electrode decays in time t through the relation

$$Q(t) = Q_0 \exp(-t/\tau) \quad \text{with} \quad \tau = \rho\epsilon_0\epsilon_r \tag{2.3}$$

where τ is the relaxation time, ϵ_0 is the absolute permittivity, ϵ_r is the relative permittivity of the electrode [79]. Typical values of ϵ_r for glass and bakelite are 8 and 5 respectively. Substituting the relevant values in (2.3) regarding τ, $\tau_{\text{glass}} \sim 1$ s and $\tau_{\text{bakelite}} \sim 10$ ms.

This time is very large compared to the discharge time which is only of the order of a few ns. Electrode behaves like an insulator for this amount of time and the electric field drops locally assimilating the discharge. The detector will remain inactive in this region for the time characterized by τ. Thus, bakelite RPCs can handle relatively higher count rates than glass.

As the electrodes are resistive in nature, to apply a uniform electric field over the gas gap, a conductive coating usually of graphite is applied on the outer surface of the electrode. The surface resistivity - resistance per unit area - of the coating should be high enough so that the charges generated in the gas gap as explained in the previous section induce electrical signals on metallic strips capacitatively coupled to the gap. Typical values of surface resistivity of the

graphite coating are 100 - 300 kΩ/□ (□ : per square) for bakelite and 1 MΩ/□ for glass RPCs. The '□' or 'square' here refers to the size of the jig used to measure the surface resistivity (typically of 10 cm × 10 cm area).

The capacitative coupling enables the placement of readouts orthogonal to each other on either side of the gap to obtain position information as X-Y coordinates.

2.4   RPCs at ICAL

The ICAL detector at INO described in Chapter 1, will be employing RPCs in a huge scale. It will be detecting neutrinos produced in the atmosphere indirectly by detecting the muons produced due to their interaction in the iron plates. The RPCs employed in this detector should have good position and time resolution. The strip width of these RPCs will be 2.8 mm. As ICAL will be huge with an area of 48 m × 16 m in each layer, the RPCs will be of 2 m × 2 m area making a total of 192 RPCs per layer. The RPCs will be operated in the avalanche mode.

Although streamer mode operation is possible since the experiment relies on cosmic events, due to the long duration of the experiment and aging concerns related to streamer mode operated RPCs, avalanche mode RPCs are being preferred. The gap thickness will be 2 mm and electrodes will be made of glass due to its ease of availability in India. However, bakelite RPCs have not been ruled out and are being explored.

RPC characterization using

Hodoscope and HMC based

pre-amplifiers

3.1 Assembly and testing of Glass RPC

A 1 m^2 square glass RPC was assembled with G10 readouts. The square gas gap
is 1 m^2 in area and has been procured from KODEL (KOrean DEtector Lab),
South Korea. Glass electrode is 3 mm thick and the gap thickness is 2 mm. The
spacing between the electrodes is maintained using ~1 cm (diameter) button
spacers arranged in a matrix of optimized spacing.

The surface resistance of conductive graphite coating is 1 MΩ/□. It has two
G10 based readouts. The gap is sandwiched between the readouts. The readouts
are placed orthogonal to each other so that one can have position information as

---

This chapter is based on [5]
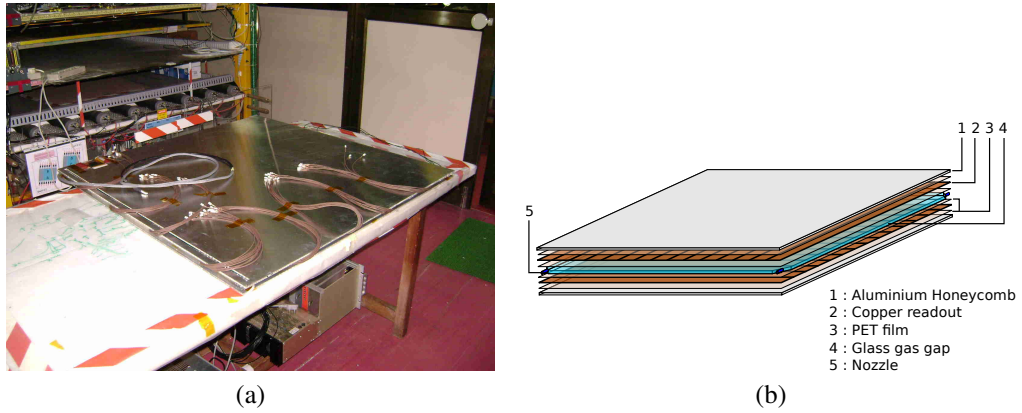
FIGURE 3.1: (a) The assembled G10 RPC. (b) The layered schematic of the RPC

XY coordinates.

The readouts are capacitatively coupled to the glass gas gap using 300 µm Mylar/PET sheet. A picture of the assembled RPC is shown Figure 3.1(a) and layered schematic of the assembled RPC is shown in Figure 3.1(b). The aluminium honeycomb is used for support.

3.1.1 Preliminary tests of the RPC

I-V characteristics

The gas gaps, glass or bakelite are first subjected to high voltage tests before being assembled in an RPC. High voltage is ramped in steps and the leakage current is monitored. If the leakage current is higher than expected, the gap is not suitable for use in an RPC.

The behavior of the RPC i.e. variation of the leakage current with the applied voltage can be understood with the help of the equivalent electrical circuit shown in Figure 3.2. The gas mixture is represented as a zener diode.

Typical values of the bulk resistivity are $\sim 10^{12}$ to $10^{13} \Omega \cdot$cm for glass and
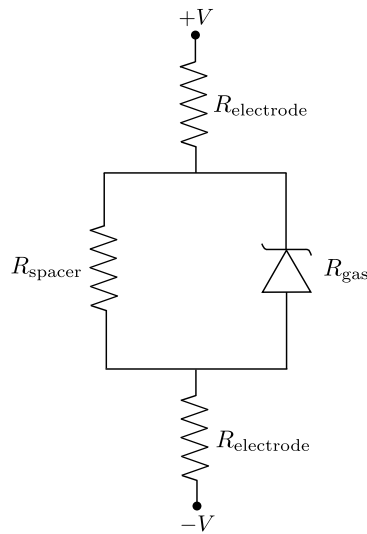
FIGURE 3.2: RPC electrical equivalent circuit.

~10^{11} to $10^{12}\Omega$·cm for bakelite. The bulk resistivity of the spacer is around ~$10^{13}\Omega$·cm. At low voltages, the resistance of the circuit is high and a small leakage current flows through the circuit. The behaviour is ohmic. As the voltage is increased, avalanche formation takes place and the gas becomes slightly conducting with a non linear increase in current. After a point, there is a drastic increase in the leakage current due to streamer discharges.

Figure 3.3 shows the plot of the HV scan of a glass gas gap. The plot shows the typical characteristic of an RPC. Two distinct regions can be noticed. The first region from 0 to 9000 V, is linear and ohmic. The gas mixture shows high resistance and therefore the leakage current is small.

At voltage >9000 V the avalanche formation begins and the curve becomes nonlinear. The region from ~10200 V and above the current drastically increases. It is linear and ohmic. From this point onwards, the gas mixture becomes conducting due to formation of streamers.

The voltage at which the streamer formation takes place depends on the gas

V-I Characteristics of 1 m^2 Glass RPC
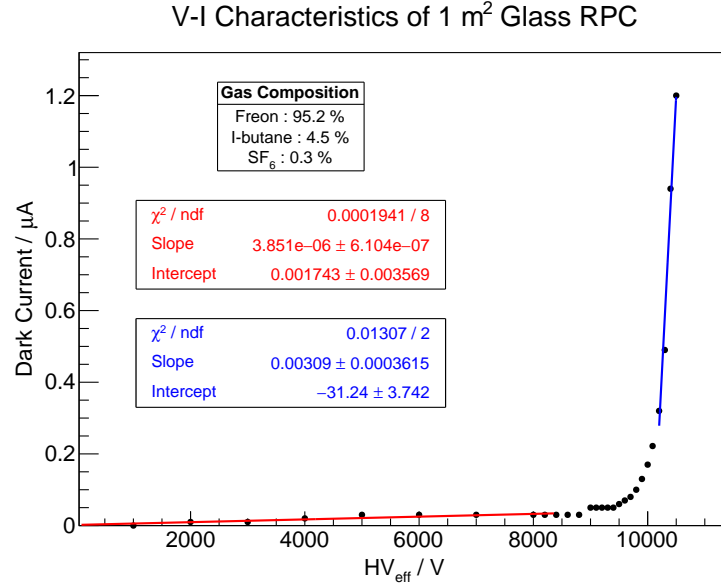
FIGURE 3.3: I-V characteristics of the RPC.

mixture and the thickness of the gas gap. Figure 3.3 is for a typical gas composition of Freon-r134a : isobutane : SF$_6$ :: 0.952 : 0.045 : 0.003 and gap thickness of 2 mm.

High voltage applied to the RPCs is scaled to a reference pressure and temperature using environmental conditions in the lab. This is done so that the measurements become independent of the site. The scaling relation [80, 81] is

$$HV_{\text{eff}} = HV_{\text{applied}} \times \frac{P_0}{P} \times \frac{T}{T_0} \tag{3.1}$$

where, P, T are the ambient pressure, temperature and $P_0 = 990$ mbar, $T_0 = 293$ K are the reference pressure, temperature respectively. The reference values can be arbitrary, but it would be preferrable to have typical values corresponding to the site where the detectors would be employed. While temperature in the lab is maintained at the reference temperature, pressure is slightly more (between 1000 to 1015 hPa).

Long term monitoring of glass RPC

RPC is subjected to long term high voltage test. This is to ensure that the assembly and high voltage connections are properly done. RPCs employed in the ICAL will have to function for years without any problem. This is a general quality control test employed for RPCs used in various experiments.
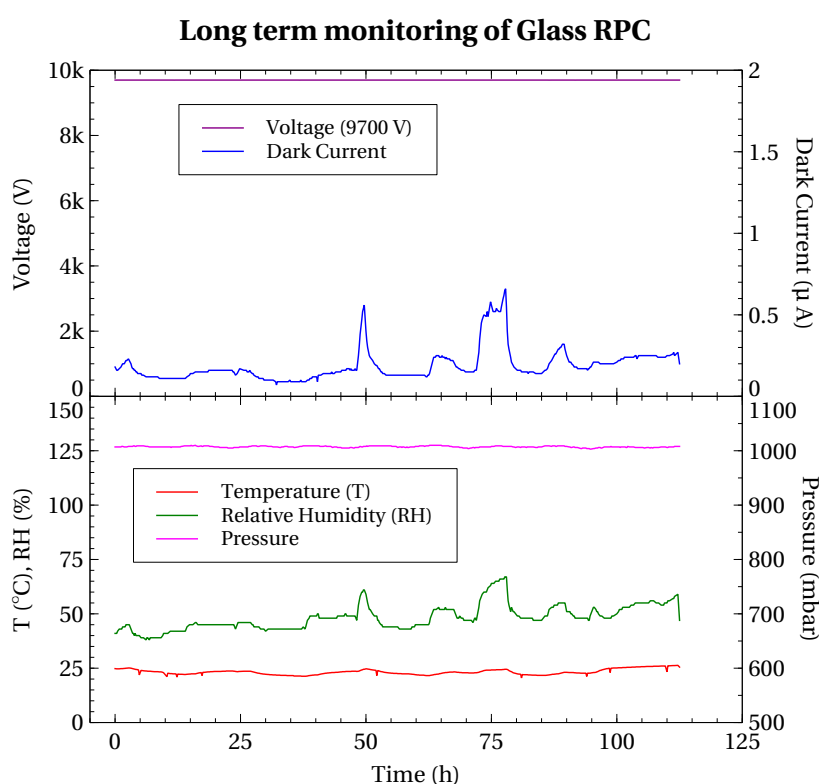
FIGURE 3.4: Long term monitoring of the RPC

The RPC is kept at a fixed high voltage say ~10 kV and is monitored for a period of five days. Figure 3.4 shows the variation of leakage current over the period of time. Also plotted are the environmental conditions. The variations in the leakage current are influenced strongly by the humidity in the environment. The correlation is clearly visible. If the humidity remains constant then

the current remains quite stable.

3.1.2   G10 Readout

Studies have been carried out with RPCs having two different kinds of readouts. One having the dielectric made of polycarbonate honeycomb and the other with G10 or FR4 material used in print circuit boards. While the honeycomb readout is lighter, it is around 5 mm thick. G10 based readout has a thickness of ~0.9 mm. Dimensions are listed in Table 3.1. The honeycomb readout RPCs were characterized using ANUSPARSH ASIC based preamplifiers and are discussed in the next chapter.

Readout Type	G10
Total Readout area (m^2)	1
No. of readout strips	32
Strip thickness (μm)	35
Strip width (mm)	28
Strip spacing (mm)	2
Readout thickness (mm)	5
Dielectric constant	~ 4.2

TABLE 3.1: Dimension and properties of the G10 readout.

G10 readout used in the RPC are shown in Figure 3.5(a) and 3.5(b). The readouts were fabricated by a local vendor in Mumbai. There are 32 readout strips. To make collection of signals easier from the readout, the signals from eight strips are grouped and concentrated at four points using extended tracks as shown in Figure 3.5(c) and 3.5(d). A microstrip of width ~2 mm runs all around the readout close to the edges to be used as a connection to ground.

(a) Front   (b) Back

(c) Front   (d) Back
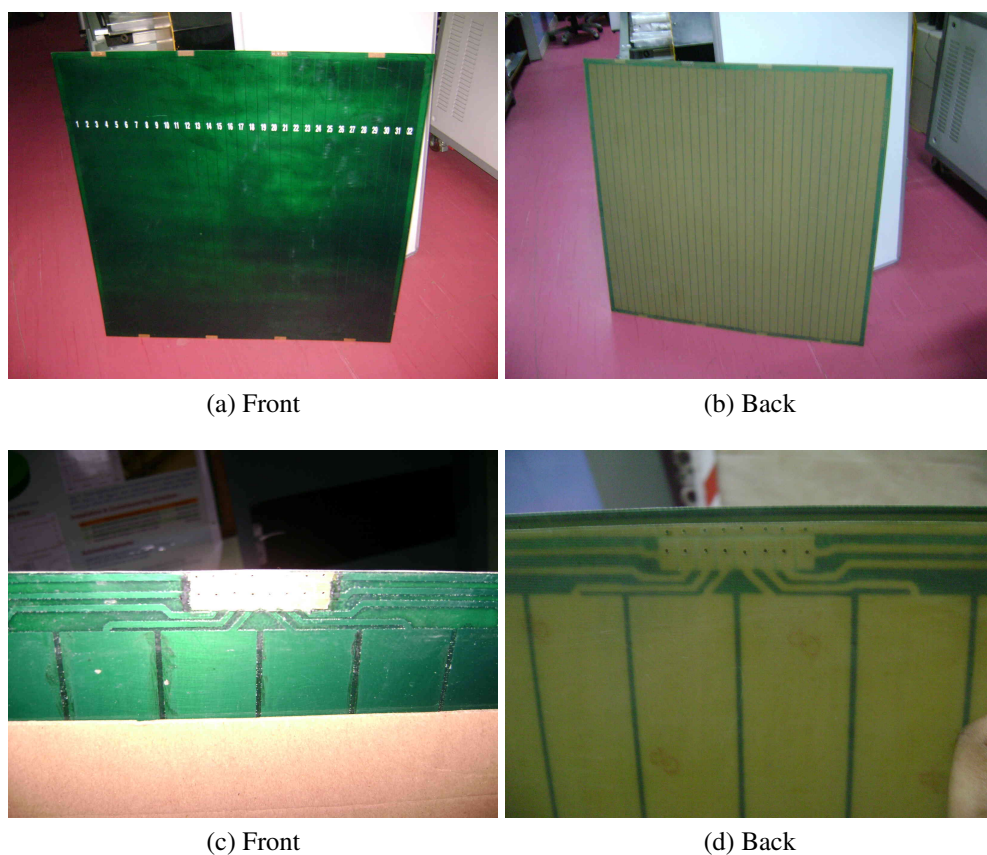
FIGURE 3.5: (a - b) Front and back view of the G10 readouts. (c - d) Front and back view of the zoomed portion of the extended tracks.

Coaxial cables of 50 Ω (At GHz frequencies [82]) impedance were soldered at the extraction points on the readout and the signals were observed on the oscilloscope. The pulses are shown in Figure 3.6. A lot of ringing and signal distortion can be seen.

The strip acts as a transmission line for the signal generated in the RPC. There are two problems

1. The readout strip is an inhomogeneous transmission line.

2. For the available voltage preamplifiers to be used, their input impedance

of 50 Ω has to be matched with that of the readout strip.
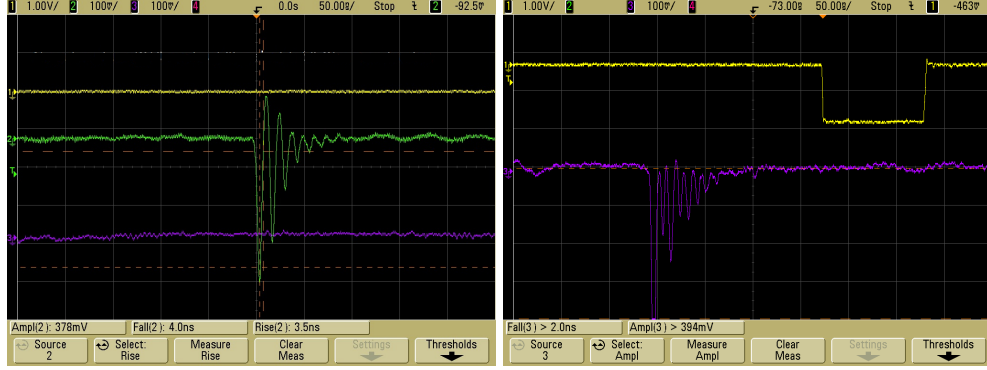
(a) Coaxial cable soldered on extended track of readout strip

(b) Coaxial cable directly soldered on readout strip.

FIGURE 3.6: Pulses seen with the initial configuration of G10 readout

To address these problems, we separated the strip from the their extensions using a knife. Cables were directly soldered on the readout strips using a resistive circuit.

Characteristic impedance of readout strip

The characteristic impedance Z_0 of the readout strip can be theoretically calculated using the formula [83]

$$Z_0 = \frac{120\pi}{\sqrt{\epsilon_{\text{eff}}} \left(\frac{W}{h} + 1.393 + 0.677 \ln \left(\frac{W}{h} + 1.444 \right) \right)}$$

$$\text{and } \epsilon_{\text{eff}} = \frac{\epsilon_r + 1}{2} + \frac{\epsilon_r - 1}{2} \left[\frac{1}{\sqrt{1 + \frac{12h}{W}}} \right]$$

(3.2)

where, W is the width of the strip, h is the thickness of the dielectric and ϵ_r is the dielectric constant of the strip. Plugging the values for the relevent parameters using Table 3.1, we find that the characteristic impedance for the G10 readout strip turns out to be 4.87 Ω.

Impedance matching

Impedance matching is very important when the time period of the signal being transmitted is smaller than the propagation time. If a signal is transmitted from one medium to the other, the reflection coefficient η is given by the relation

$$\eta = \frac{R - Z}{R + Z} \tag{3.3}$$

where, Z is the impedance of the first medium and R the impedance of the second medium. So, when $R = Z$ there is no reflection. If $Z > R$, η is negative. The reflected signal will be inverted. If $Z < R$, η is positive. The reflected signal will be of the same polarity.

The readout strip impedance is ~5 Ω. Signals from the readout are fed to the preamplifier using 50 Ω coaxial cables. If the cables are directly soldered on the readout strip, the reflection coefficient is 0.81 and at the other end it is close to 1 without any termination.
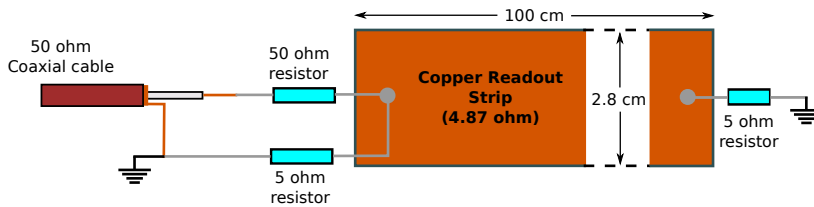
FIGURE 3.7: Circuit used to match the impedance of the readout strip.

A resistive circuit has been used to match the impedances. It is shown in Figure 3.7.

Towards the electronics side, the 50 Ω coaxial cable connecting the preamplifier with the strip appears to the signal induced on the readout strip as a path with 5 Ω impedance because of the presence of a 5 Ω resistor in parallel con-
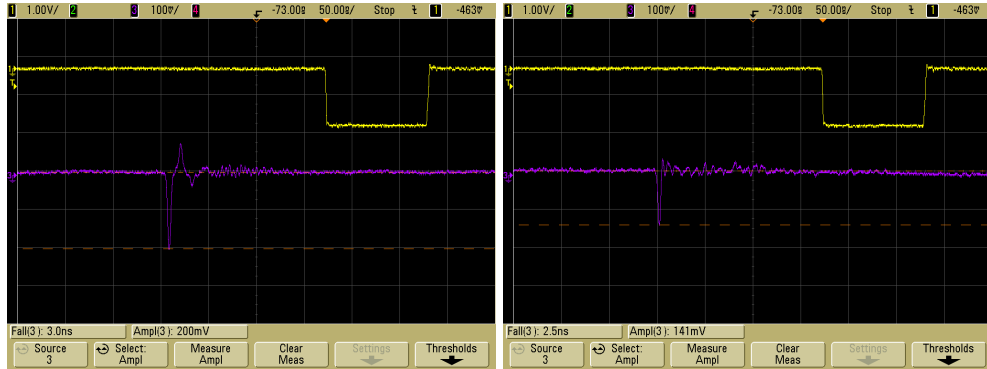
(a) Signal without 5 Ω termination.   (b) Signal with 5 Ω termination.

FIGURE 3.8: Signals after employing the impedance matching circuit

necting the ground. The other end appears to be an infinite transmission line for the signal due to termination by a 5 Ω resistor.

The pulses observed on the oscilloscope after using the resistive circuit is shown in Figure 3.8. Figure 3.8(a) shows the pulse when the strip is not terminated by a 5 Ω resistor and 3.8(b) shows the pulse when the strip is terminated by a 5 Ω resistor at the other end. There is good matching. Pulse distortion and ringing has reduced drastically.

3.2 Hodoscope

There are around 1000 RPCs in the CMS detector [84] including the endcap and barrel regions and the proposed Iron Calorimeter detector (ICAL) at INO [4] would require approximately 30000 RPCs of ~4 m^2 area. These experiments are built underground and operate over long periods of time. If detectors develop problems when these experiments are running, it is not possible to service or replace them. Therefore, RPCs need to be tested thoroughly before being

employed. The dimension and number of RPCs needed for these experiments, requires a setup which can characterize each RPC in a reasonable amount of time for functional parameters such as efficiency, cluster size, strip profile and noise rate. A cosmic muon hodoscope is a suitable option.

Hodoscope is an instrument which is used to detect the path of the particle. The hodoscope at NPD-BARC was constructed to characterize RPCs with cosmic muons, both for the RE4 (4th RPC Endcap disk) upgrade for the CMS experiment during the long shutdown (LS1) and also for the R & D related to glass RPCs for INO, muon tomography and related experiments. India had been mandated to build and characterize 50 RE4/2 (2 refers to the inner ring of the endcap disk) RPCs for the RE4 upgrade which was done during the long shutdown LS1 (2013-2014). The Hodoscope contains sixteen large area scintillators for characterization of RPCs using cosmic muons as triggers. These large area scintillators have been fabricated to fully characterize RPCs in one go covering the entire active area. At the surface of earth the average energy of muon is 3 - 4 GeV with an average flux of 1 $cm^{-2} \cdot min^{-1}$.

The scintillators are arranged in two layers, each consisting of eight scintillators. The two layers are separated by a vertical distance of 210 cm between which RPCs can be stacked in seperate shelves for characterization. Each of the scintillator (Bicron BC-408) measuring 180 cm $\times$ 18 cm $\times$ 1 cm, were cut and polished (up to 10 µm levels) in the Centre for Design and Manufacture-BARC. Each of these scintillators is coupled to a separate PMT (Photo Multiplier Tube) at each end. The PMTs were procured from Electron Tubes (ET-9814B, 51 mm diameter, QE $\sim$30% and gain $\sim10^6$). As the length of these scintillators is quite long, it was decided to have two PMTs at either end, so that the efficiency of the

scintillator is not compromised, over its length. Figure 3.9 shows the schematic

of the scintillator, light guide, cookies, PMT and the HV divider.
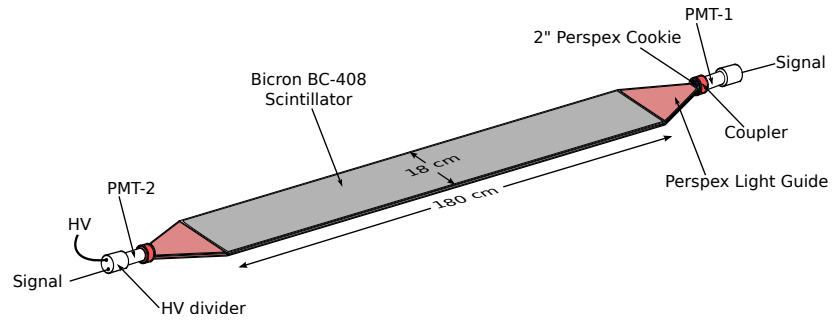
FIGURE 3.9: Schematic of a long scintillator paddle.

(a)   (b)
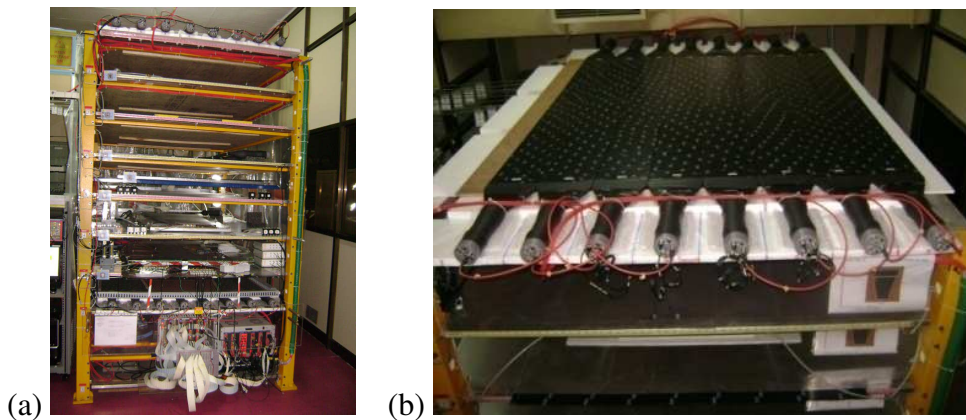
FIGURE 3.10: (a) The Hodoscope. (b) The top plane having 8 scintillators.

The whole assembly was then wrapped by a reflector in the inside and doubly

wrapped with black PVC tape on the outside. To localize the region of the RPC

while characterizing them, two portable scintillator paddles of smaller dimension

(40 cm × 18 cm × 1 cm) with a single PMT at one end were also fabricated in a

similar way using the same scintillator sheets and light guides.

The hodoscope is shown in Figure 3.10(a). Figure 3.10(b), shows the eight

scintillators lined side by side in the top layer shelf #9 of the cosmic stand in the

RPC Lab. The bottom layer of scintillators is configured similarly in shelf #2.

The coincidence of these scintillator signals will provide us the cosmic trigger to evaluate the performance characteristics of the RPCs. The hodoscope along with RPCs will also be very helpful for the proposed muon tomography programme.

3.3 DAQ and trigger

The signals of the PMTs are brought to the electromics through 10.5 m cables to ensure equal delay (~50 ns).

Electronics is composed both of NIM and VME standards. The VME controller is CAEN Mod. V2718. It communicates to the PC through an Optical Link Bridge. It can generate a clock of 20 MHz and is used to synchronize the TDCs. The TDC (Multihit) we are using is CAEN Mod. V1190A having 128 Channels. Its maximum resolution is 100 ps (with 40 MHz clock). It accepts either ECL or LVDS signals only. The V1190A is being operated in the so called 'straddling' mode [85] where, the trigger window is straddled around the trigger, so that events occurring both before, and after the trigger are recorded; provided they are within the window width. The trigger matching mode can be decided by setting different programmable parameters [85].

The signals from the strips of the RPC are first amplified using 8 channel HMC (Hybrid Micro Circuit) based preamplifier boards, discriminated using commercial NIM Leading Edge Discriminators and fed to NIM-ECL translators. The ECL output is then fed to the TDC. Signals of the scintillators coming from the NIM electronics are converted to ECL signals using ECL to NIM translators

as well.

3.3.1   HMC based preamplifiers

HMC preamplifier boards mentioned previously have an input impedance of 50 Ω. The HMCs BMC-1513, BMC-1595 and BMC-1597 have been developed by Electronics Division-BARC and are produced by BEL (Bharat ELectronics) laboratories, India [86, 87]. Some of its features are listed in Table 3.2. The polarity of the RPC signals is positive on the negative electrode and negative

TABLE 3.2: HMC specifications.

HMC	Rise time (ns)	Input impedance (Ω)	Gain	Polarity	
				Input	Output
BMC - 1595	2.4	50	10	$-$ve	$+$ve
BMC - 1597	2.5	50	10	$+$ve	$\pm$ve
BMC - 1513	2	50	10	$-$ve	$-$ve

on the positive electrode. Therefore to account for the polarity and have a gain of ~100, BMC-1597 and BMC-1595 are cascaded with BMC-1513 for positive and negative polarity respectively on different boards. The gain is adjustable.■

The way the trigger is generated is illustrated in the block diagram in Figure 3.11.

Each scintillator is coupled to two photomultipliers. The logical OR of the two photomultiplier signals after discrimination forms the scintillator signal. We will have 8 such signals from both top and bottom planes. 8-fold logical OR of signals in one plane forms the plane signal. Therefore, we will have two signals: one from the bottom plane and one from the top plane. The logical AND of these two signals in coincidence with a paddle forms the trigger. Trigger, top, bottom
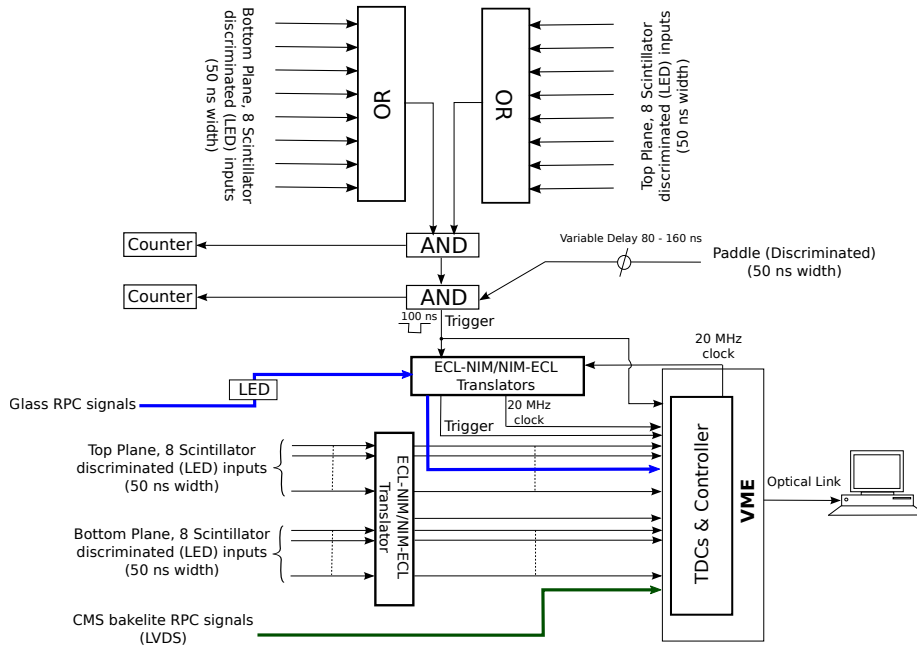
FIGURE 3.11: Block diagram of the hodoscope setup [5].

plane scintillator and paddle signals are also fed to the TDCs after discrimination and translation. Software developed at CERN for DAQ which stores data in the ROOT format [88] has been adapted to the hodoscope.

The coincidence pattern of the top and bottom plane scintillators observed for 100 000 events is shown in Figure 3.12. The pattern peaks along the diagonal. This is expected as the cosmic muon flux is not uniform over the zenith angles.

3.4   Characterization of RPC

The assembled glass RPC with the G10 readouts was placed inside the hodoscope. Illustration of the setup is shown in Figure 3.13.

4 middle scintillators of the top and bottom planes were used in coincidence with two small paddles described in Section 3.2 each of dimension (40 cm × 18
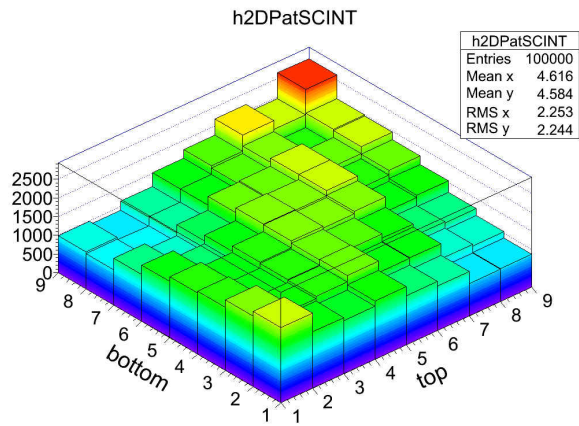
FIGURE 3.12: Coincidence plot of top and bottom plane scintillators. Top 1-8 and Bottom 1-8 are the numbers corresponding to the scintillators in the top and bottom planes of the hodoscope [5].
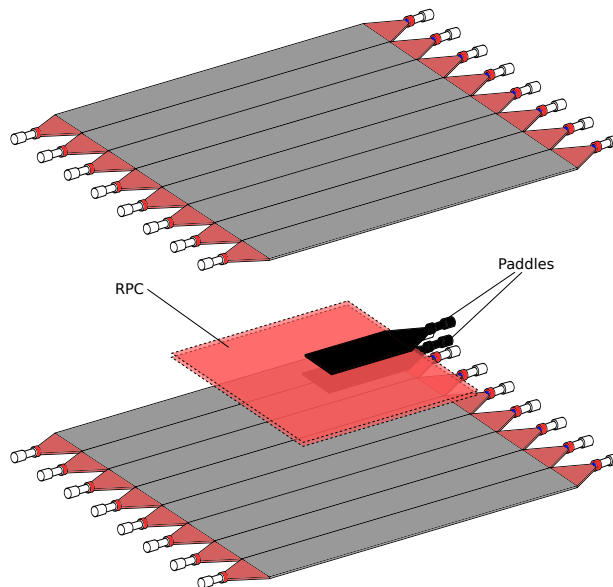
FIGURE 3.13: Glass RPC in the hodoscope.

cm × 1 cm) for trigger. Other hodoscope scintillator paddles were turned off. Paddles were placed one above and below the RPC. As the paddle width is only 18 cm, inclusion of a second paddle of same dimension constrains the geometry to 6 strips.

After amplification from the HMC preamplifier, signal threshold was set at 30 mV and gain was adjusted to be ~80.

The RPC has total of 64 strips - 32 on the X and 32 on the Y. The bulk of electronics, especially commercial NIM discriminators and translators needed for only a stack of 6 such RPCs = 6 × 64 = 384 channels will be too much. So instead of the HMC based preamplifiers, an ASIC (Application Specific Inte-
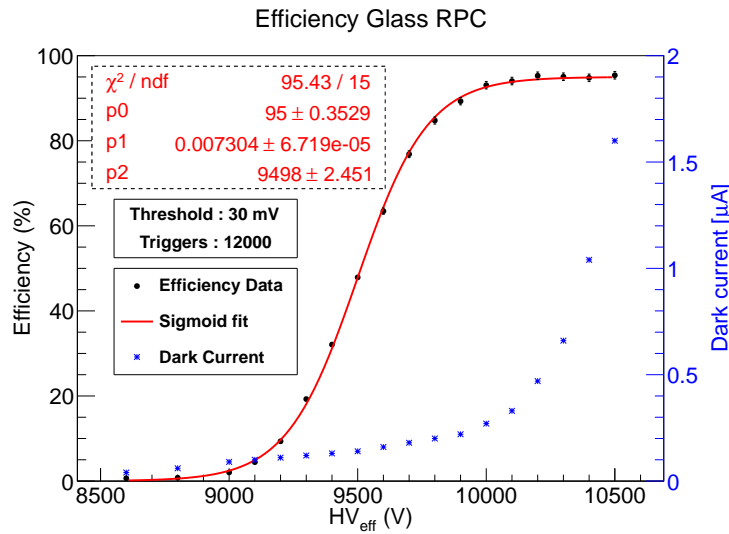
FIGURE 3.14: Efficiency of the glass RPC at a threshold of 30 mV [5].

grated Circuit) based frontend solution called ANUSPARSH has been developed indegenously by Electronics Division - BARC, which will amplify, discriminate and provide output from the RPC directly in the LVDS or ECL format. They are discussed in the next chapter.

Efficiency plot for the glass RPC is shown in Figure 3.14. A sigmoid function [80, 81] of the form

$$f(x) = \frac{a}{1 + \exp[b(c - x)]} \tag{3.4}$$

is used to fit the data where, a is the maximum efficiency, b is the slope and c is

the voltage at 50% efficiency.

From the figure, we can notice that the plateau occurs at the knee region of
the rising dark current which is expected. The RPC shows an efficiency of 95%.
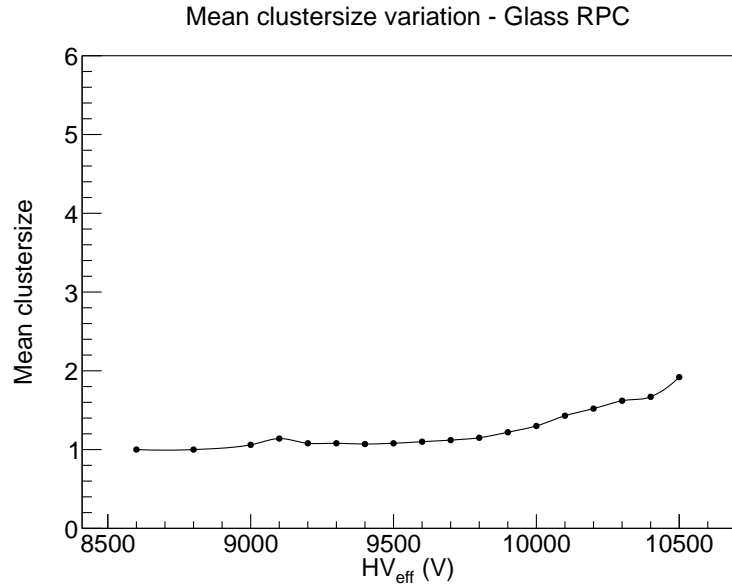
FIGURE 3.15: Variation of mean cluster size of Glass RPC with high voltage [5].
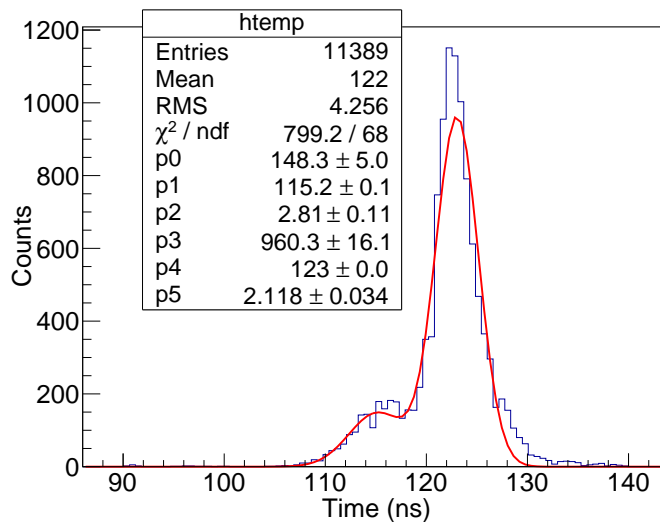
FIGURE 3.16: Time distribution between trigger and RPC strip signals.

The average number of strips firing for a given event i.e the mean cluster size is an important parameter of an RPC. In the ICAL, cosmic showers or neutrino interactions in iron generate hadrons like pions that fire multiple strips in the RPC. If they are to be distinguished from a muon event generated by the neutrino interaction, the clustersize for muon events must be as small as possible. If it is large, then false identification of a muon as a hadron is possible. The clustersize plot for the RPC is shown in Figure 3.15. 2 strips fire on an average for a given muon event.

Distribution of the difference in time between the signal of the RPC and trigger is shown in Figure 3.16. The strip (transmission line) is not purely resistive. Perfect impedance matching cannot be achieved due to contributions from reactive components. Moreover, resistors with exact resistance values cannot be obtained. A small peak occurs due to this reason. This does not affect the efficiency since only one hit is counted in the region of interest in the RPC with respect to the trigger. The distribution is fitted with two gaussian distributions and the width of the larger peak is ~2 ns. Small variations of the delay in the readout strips, field non uniformities (spacers), electronic jitter and walk and variation in the muon interaction position contribute to the broadening of the distribution. The width of ~2 ns is the combined effect of all these parameters.

3.5 Summary

The Hodoscope composed of 16 scintillators with double PMTs is fully operational. VME DAQ system has been implemented by adapting the CERN based software.

Good preliminary results have been obtained from glass RPC with G10 readouts. The RPC shows an efficiency of 95%. The mean clustersize is also less than 2. Time distribution width between the time of the trigger and RPC signal is around 2 ns including the effect from readout strip delay, electronic jitter and walk, field non uniformities and muon interaction position. The operating point of the RPC is around 10200 V_{eff} with a threshold of 30 mV.

Full area of the square RPC could not be characterized using the hodoscope due to insufficient electronics. Once sufficient electronics are available, full RPC characterization can be performed. The hodoscope was used to characterize 50 RE4/2 RPCs of the CMS endcap for the RE4 Upgrade during the first Long Shutdown (LS1) of the LHC. Some details are discussed in Appendix A.

RPC characterization using

Anusparsh

4.1 The ANUSPARSH ASIC

The ANUSPARSH ASIC Version I, II and III have been designed and developed by Electronics Division, BARC as a multichannel, low power and fast amplifier-discriminator solution for front-end readout of RPCs in the ICAL.

Based upon the progressively evolving front-end readout requirements of INO-ICAL RPCs, ANUSPARSH ASIC evolution has happened in three stages

4.1.1 ANUSPARSH-I

The first version of ANUSPARSH ASIC was designed and fabricated in 0.35 μm mixed CMOS process in year 2010. It had eight front-end channels. Each front-end channel consisted of regulated cascode trans-impedance pre-amplifier, two stages of differential amplifier followed by a fast leading edge discriminator with

LVDS output. A multiplexed fast analog buffer capable of driving a 50 Ω cable was also incorporated in this ASIC. The regulated cascode trans-impedance pre-amplifier topology was used due to its inherent low input impedance over wide frequency range leading to good impedance matching with the RPC pick up strip impedance of ~50 Ω, besides providing large trans-impedance gain and lower power consumption.

4.1.2   ANUSPARSH-II

Gain was lowered for optimum noise performance (4 mV·μA^{-1} instead of 7 mV·μA^{-1}) and at higher threshold to overcome DC bias spread across front-end channels. Common Mode Feedback (CMFB) in the differential amplifier stages of each channel and Dynamic DC Offset Compensation (DCOC) in the input stage was implemented to minimize the channel gain variations. Layout design and pin assignment was optimized.

4.1.3   ANUSPARSH-III

A two chip (two amplifiers and one discriminator) solution has been designed separating the amplifier and discriminator. ASIC packages have been revised to meet the space constraints of the ICAL final Front-end setup. The amplifier ASIC is designed with four channels to minimize routing lengths between detector pickup strips and the amplifier in order to improve detector signal integrity. Amplifier ASICs are now voltage amplifiers.

ANUSPARSH-I and II are both trans-impedance amplifiers. They are sensitive to the current flowing in the detector readout. ANUSPARSH-III is a voltage

TABLE 4.1: Version details of ANUSPARSH.

ASIC specifications	ANUSPARSH		
	I	II	III
Amplifier type	Trans-impedance		Voltage
Total channel gain	6 mV·μA^{-1}	4 mV·μA^{-1}	
Linear input dynamic range	±100 μA	±100 μA	±100 μA
LVDS common mode voltage range	0.8 V to 1.6 V	0.8 V to 1.6 V	0.8 V to 1.6 V
Timing Accuracy	~72 ps	~72 ps	~72 ps
Power Consumption/Channel	~45 mW	~45 mW	
Die Area and Package	3.5 mm by 3.5 mm; CLCC48	4 mm by 4 mm; CLCC68	

amplifier ASIC and sensitive to the voltage at the detector readout.

4.2 Test setup

4.2.1 RPC

We have tested RPCs with ANUSPARSH - II and III boards. ANUSPARSH - II is the improved version of ANUSPARSH-I. The amplification method of ANUSPARSH - II and ANUSPARSH - III boards are different (trans-impedance and voltage amplifiers respectively). So we have tested RPCs with both these boards.

4.2.2 Polycarbonate honeycomb readout

G10 readouts of the 1 m × 1 m RPC described in the previous chapter were replaced by polycarbonate honeycomb readouts also having 32 strips. ANUS-

PARSH ASIC front-end had been used to test glass RPCs at TIFR, Mumbai. They had polycarbonate honeycomb readouts. For consistency, we did tests on RPCs assembled with the same readouts using ANUSPARSH at RPC lab, NPD-BARC. Honeycomb readouts are being considered for the RPCs at ICAL. They are ~5 mm thick and have a strip impedance of ~39 Ω.

Dielectric is made of a polycarbonate honeycomb sandwich. It has copper strips on one side and aluminum sheet on the other for ground. The dimension and details are given in Table 4.2. Front and back views of the readout are shown in Figure 4.1(a) and Figure 4.1(b) respectively.

TABLE 4.2: Dimension and properties of the Polycabonate honeycomb readout.

Readout Type	Polycarbonate Honeycomb
Total Readout area (m^2)	1
No. of readout strips	32
Strip thickness (μm)	35
Strip width (mm)	28
Strip spacing (mm)	2
Readout thickness (mm)	5
Dielectric constant	~ 1.4

Using Equation (3.2), the characteristic impedance of the readout strips is calculated to be ~39 Ω. Since this value is close to the input impedance of the pre-amplifier, no circuits have been used to match the impedance. The strips have been terminated using 50 Ω resistors. Coaxial cables are directly soldered on the strips.
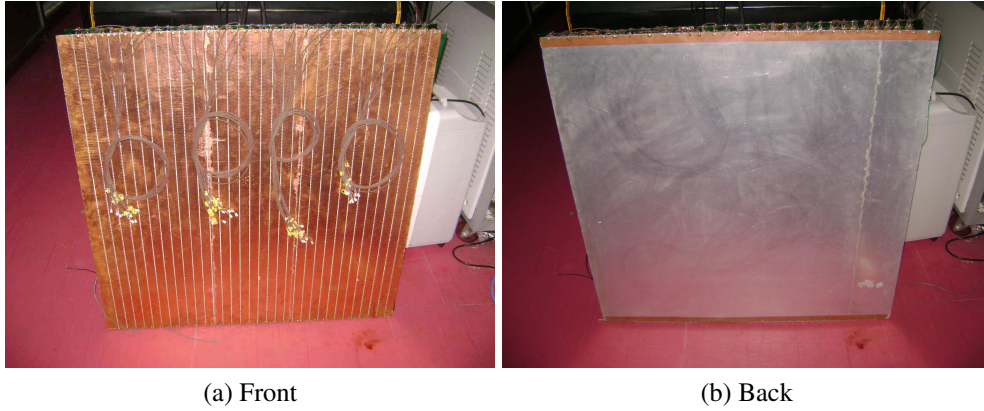
| (a) Front | (b) Back |

FIGURE 4.1: (a) Front view of the polycarbonate honeycomb readout. (b) Back view of the polycarbonate honeycomb readout.

4.2.3 Electronics

Discriminator LVDS data from the ANUSPARSH front-end electronics was acquired and processed by a portable data acquisition module [89] comprising of ANUPAL ASIC [90], an FPGA and a micro-controller with serial interface to the PC. NIM level trigger is supplied to the module using coaxial LEMO cable. The details of the DAQ are given in table 4.3.

TABLE 4.3: ANUPAL ASIC based portable DAQ features.

No. of Channels	4
Dynamic range	1.8 μs
Resolution	126 ps
Readout Interface	SPI
Power Consumption	~45 mW @ 3.3 V supply
Die Area	1.5 mm × 1 mm

To compare the timing performance of the ASIC, data was also acquired using CAEN Mod. V1190A, VME based TDC with a resolution set to 200 ps.

4.2.4 Setup

Signals from the strips of the RPC were taken to the ANUSPARSH front-end
using 50 Ω coaxial cables with relimate connectors. On the other end, strips
were terminated with a 50 Ω resistor. The standard avalanche mode gas mixture
of Freon-r134a : Isobutane : SF_6 :: 95.2 : 4.5 : 0.3 was used.

Due to the frequent need of fine tuning the parameters of ANUSPARSH
front-end board, we did not use the hodoscope to test the RPC. Instead, the
validating trigger was generated using two-fold telescopic coincidence of only
two plastic scintillator paddles of dimension 40 cm $\times$ 18 cm $\times$ 1 cm each. The
ANUPAL DAQ could only accept 5 inputs from LVDS. So, the paddles were
placed such that they covered five six pick-up strips completely and half of the
strips on either side.
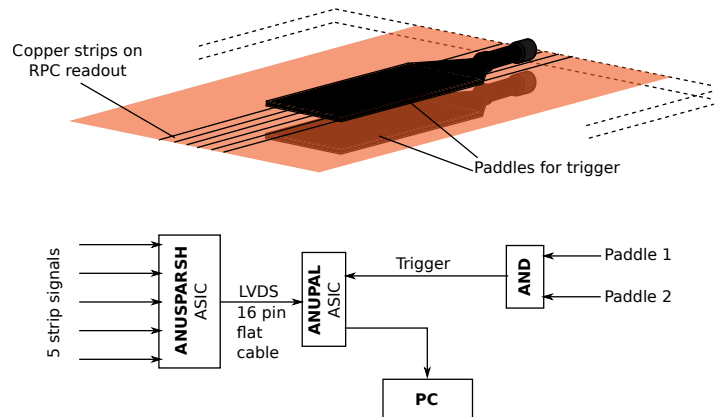
FIGURE 4.2: Schematic of the RPC characterization setup

Pictures of the front-end boards are shown in Figure 4.3(a) and Figure 4.3(b).

The strip signals were amplified and discriminated using ANUSPARSH pre-
amplifier and the LVDS output was fed to ANUPAL DAQ.

<center>(a) (b)</center>
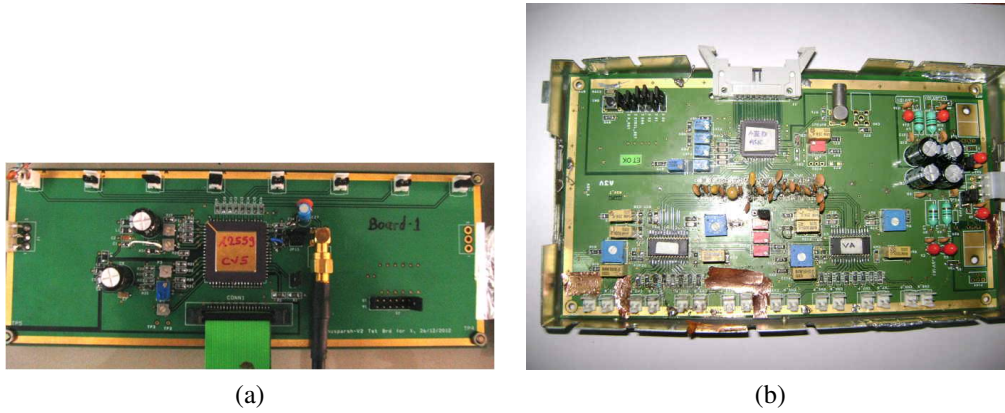
FIGURE 4.3: (a) ANUSPARSH - II ASIC based pre-amplifier board. (b) ANUSPARSH - III ASIC chipset based pre-amplifier board.

4.3 Measurements and results

Efficiency, timing and noise rate measurements of the RPC were done using ANUSPARSH - II and III ASIC based front-end boards.

The efficiency of the RPC detector was calculated with respect to the logical 'OR' of five pick-up strip signals and two-fold coincidence signal of the paddles.

ANUSPARSH - II: HV was increased from 9 kV to 9.9 kV in steps of 200 V from 9 kV to 9.4 kV and 100 V from 9.4 kV to 9.9 kV. Discriminator threshold was set at ~35 mV.

ANUSPARSH - III: HV was increased from 8 kV to 10 kV in steps of 200 V from 8 kV to 8.8 kV and in steps of 100 V from 9.1 kV to 10 kV. Discriminator threshold was set at ~40 mV.

4.3.1 Efficiency

RPC efficiency was measured as a function of HV.
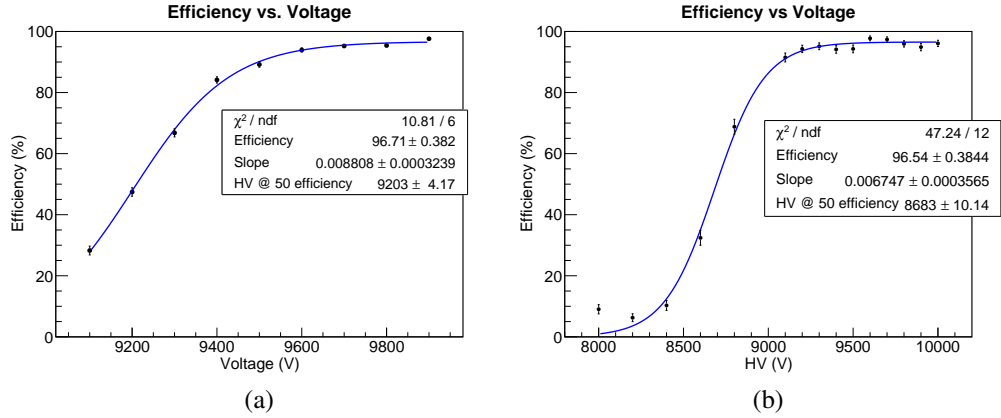
FIGURE 4.4: Efficiency of RPC. (a) ANUSPARSH-II. (b) ANUSPARSH-III

Plot of efficiency vs. high voltage for ANUSPARSH - II and III are shown in Figure 4.4. Equation (3.4) has been used to fit the data. The performance of the RPC is similar to that obtained using using HMC based pre-amplifier board discussed in the previous chapter.

The HV @ 50% efficiency in the case of ANUSPARSH - III appears 600 V before the same in ANUSPARSH - II.

4.3.2   Noise rate

Noise rate - number of signals above the threshold - was also measured during the HV sweep. Noise rate as a function of time and voltage is shown in Figure 4.5.

The occasional spikes seen in the noise rate correspond to the time when high voltage is being ramped up in the RPC.
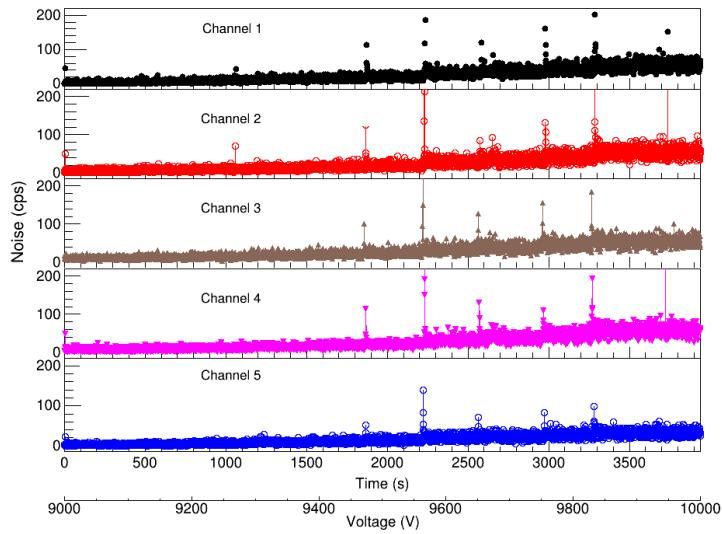
(a)
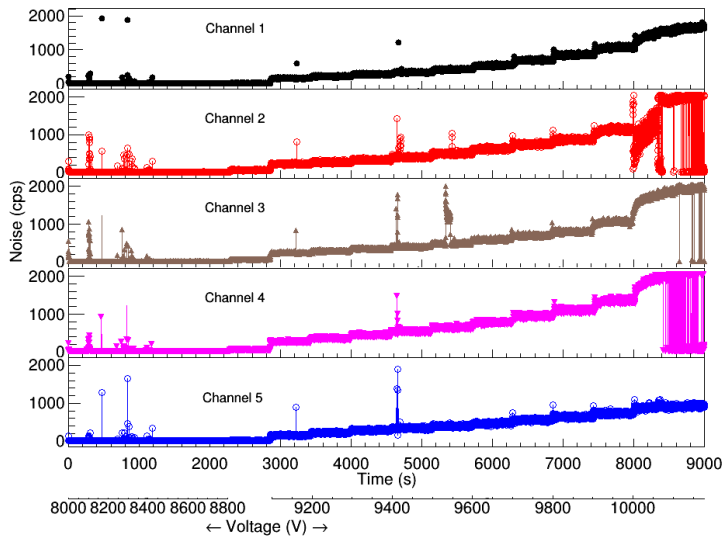
(b)

FIGURE 4.5: Channel noise rate. (a) ANUSPARSH-II. (b) ANUSPARSH-III

4.3.3   Timing

Time distribution of the difference of the time between the trigger and RPC are shown in Figure 4.6.

Figure 4.6(a) shows the time distribution of ANUSPARSH-II. ANUSPARSH - III performance was compared with both ANUPAL TDC and CAEN Mod. V1190A TDC. Figure 4.6(b) shows the measurement using ANUPAL ASIC based DAQ and Figure 4.6(c) shows the measurement using V1190A TDC.
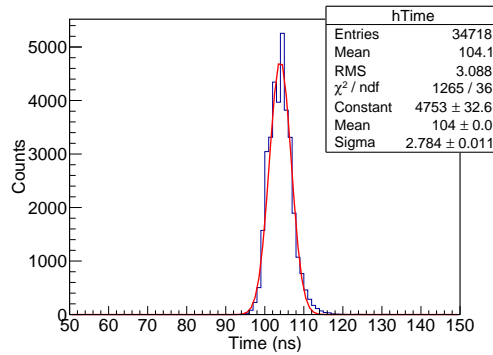
(a) ANUSPARSH - II with ANUPAL TDC.
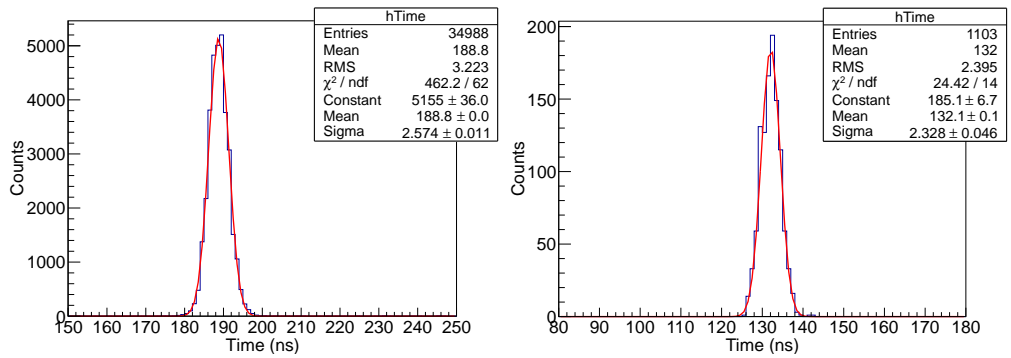
(b) ANUSPARSH - III with ANUPAL TDC.   (c) ANUSPARSH - III with V1190A VME TDC.

FIGURE 4.6: RPC time distributions measured using ANUSPARSH ASICs.

All the time distributions have been measured at an RPC high voltage of 9700 V. It is the combined effect of all the six strips.

4.4 Summary

RPCs have been characterized using ANUSPARSH - II and ANUSPARSH - III ASICs. Tests have been done using polycarbonate honeycomb readouts so that results may be compared with that obtained at TIFR, Mumbai. The RPCs characterized using both the front-end boards show similar efficiencies of ~96 %. The efficiency measured using HMC based pre-amplifiers ~95 % is comparable with this value.

1. Half the maximum efficiency is reached around 8600 V for ANUSPARSH - III compared to ANUSPARSH - II. This could be due to the fact that the principle of amplification is different (voltage and trans-impedance). Efficiency plateau measured using HMC pre-amplifiers shown in Chapter 3 (Figure 3.14) starts even later with half the maximum efficiency reaching at ~9500 V. The resistive circuit used to match the impedances has a significant loss factor. The signal is attenuated while reaching the pre-amplifier. Therefore there is a shift in the plateau.

2. Width of the time distribution between the time of the trigger and RPC signals, measured using ANUSPARSH - II and III using two different TDCs has a value around ~2.5 ns at 9700 V. This includes the uncertainty due to the position of muon interaction, electronic jitter and walk, strip delays and field non-uniformities.

3. Noise rate was higher in the case of ANUSPARSH - III compared to ANUSPARSH - II. To reduce it, certain settings on the board need to be optimized.

Due to the difficulty in availability of ANUSPARSH ASICs and shortage of time, we have not been able to do cluster size measurements. More ASICs have been ordered and front-end boards will be fabricated. Further studies using ANUSPARSH ASICs can then be performed once they are available.

Part II

Studies on scintillators for reactor

antineutrino detection

Scintillators for reactor $\bar{\nu}_e$ - A comparison

5.1 Organic Scintillators

As mentioned in Chapter 1, organic scintillator based detectors are excellent choices for detecting antineutrinos from reactors. Detectors can be constructed either with liquid or with plastic scintillators.

5.1.1 Advantages

Liquid

1. Liquid scintillators can be filled in large volumes. They are comparitively less expensive.

2. They have pulse shape discrimination property. This is useful in separating neutrons from gamma or electrons.

This chapter is based on [14]

3. Doping technology is well established. Liquids can be doped with dopants such as Gd, ^{6}Li etc. to increase probability of neutron capture. Doping is uniform enabling effective neutron capture.

Plastic

1. Plastic scintillators have to be made granular as large volume fabrication is difficult. Because of this, detectors can be modular making handling easier.

2. They are safe and easily portable.

3. Cosmic muons can be used for calibration.

4. In case of antineutrino detection, the prompt and delayed events due to positron and neutron respectively can be distinguished to certain extent using event topology.

5.1.2 Disadvantages

Liquid

1. Liquid scintillators have toxicity and flammability concerns. They have a low flash point. Reactivity of the liquid with material of containment vessel has to taken into account while building large detectors.

2. They are very sensitive to moisture in the air. A small leak can cause the liquid to become turbid and lose its properties. Occasional flushing with inert gases are required.

3. The above points make its handling difficult.

Plastic

1. Doping in case of plastic scintillators is not established. Materials with high thermal neutron absorption cross section have to be wrapped in the form of foils on each detector. This make concentration of the neutron capturing elements non uniform.

2. Due to its modular structure number of readout channels are more. Hence, they are slightly expensive.

If the detector is to be mounted on a mobile unit, so that it can be taken to various reactor sites for monitoring or for proliferation checks, then plastic scintillators would be preferrable.∎

As part of a feasiblity study for setting up ISMRAN at the Dhruva (100 MW$_{th}$) research reactor facility at BARC, we have performed simulations on organic scintillation detectors using the GEANT4 [13] simulation package. The detector designs are based on existing experiments like NUCIFER [10], PANDA [11] and Ref. [12].

5.2 Description of materials and Geometry

We model detector geometries with liquid scintillator based on Ref. [10] and Plastic scintillators based on Ref. [11, 12]. Commercially equivalent plastic

scintillators and Gadolinium (Gd) doped liquid scintillators available from Saint-Gobain Ceramics and Plastics Inc. (BC) and Eljen Technology Ltd. (EJ) have been considered. There are slight differences in the parameters listed in the respective data sheets. In such cases, the values have been considered from only one of the companies.

5.2.1   Liquid scintillator

The geometry for the liquid scintillator based detector is shown in Figure 5.1. It has a 1 t liquid scintillator (sand color) doped with Gd (0.25 %, w/w) in a stainless steel cylindrical tank coupled to 37, 5″ PMTs (brown color) [91] arranged in a hexagonal array. An acrylic disk (pink color) of 25 cm thickness couples the liquid to the PMTs. The diameter of the tank is 1.05 m and height is 1.35 m. The height of the liquid is 1.1 m amounting to an approximate volume of 0.95 m^3. EJ-331/BC-521 and EJ-335/BC-525 [92, 93] have been considered for
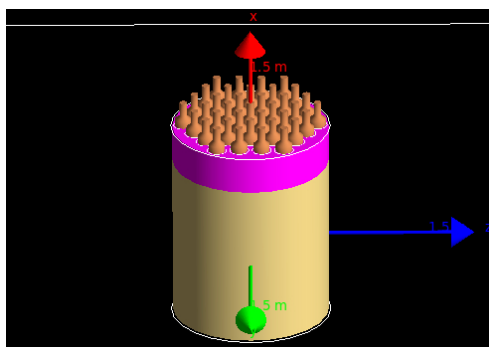
FIGURE 5.1: Liquid scintillator geometry.

liquid scintillator. The optical coupling between the acrylic disk and the PMTs is considered to be done using EJ-500 optical cement [92].

5.2.2 Plastic scintillator

Plastic scintillator geometry is modular. We consider two different configurations of the matrix with variation in granularity.
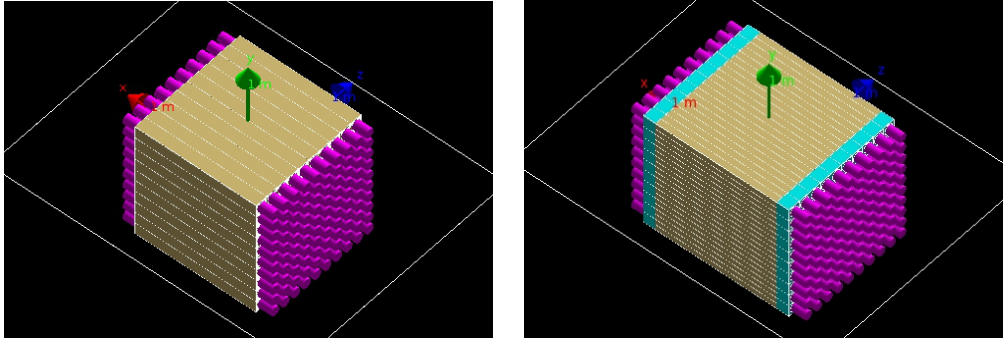
FIGURE 5.2: Plastic scintillator configurations. *Left*: Plastic Mono. *Right*: Plastic Quad.
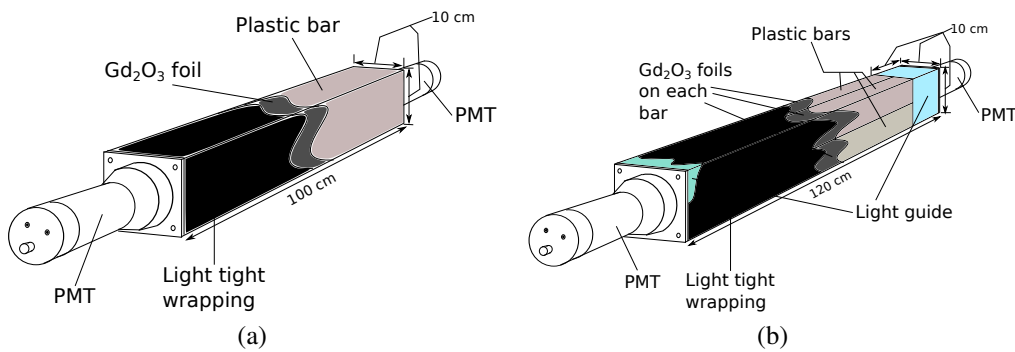
FIGURE 5.3: Illustration of plastic scintillator units. (a) Mono. (b) Quad.

1. *Matrix of single bars* : shown in Figure 5.2(Left), consists of a matrix of 100 plastic scintillator bars (Sand color) of dimension $(100 \times 10 \times 10)$ cm^3. Each bar is coupled directly to two 3″ PMTs (Dark Pink color) [91] on both sides. The active scintillator region forms a cube of side 1 m. Each bar is wrapped with aluminized mylar coated with Gd paint having a Gd$_2$O$_3$ density of 4.8 mg·cm^{-2} to facilitate neutron capture. Illustration of

the scintillator unit is shown in Figure 5.3(a). The total Gd content in the 1 t matrix would be approximately 0.17%, w/w. This configuration will be referred to as "Plastic Mono".

2. *Matrix of composite bars* : shown in Figure 5.2(Right), also is a matrix of 100 plastic scintillator units (Sand color). But here however, each unit is a composite made of four bars of plastic scintillators of dimension (100 $\times$ 5 $\times$ 5) cm^3 coupled to two 3″ PMTs with the help of (10 $\times$ 10 $\times$ 10) cm^3 acrylic light guides (Light blue color). Each of the four bars in a unit is wrapped with aluminized mylar coated with Gd paint with either 2.4 mg·cm^{-2} or 4.8 mg·cm^{-2} Gd$_2$O$_3$ density. Illustration of the scintillator unit is shown in Figure 5.3(b). We will refer to the configurations with 2.4 mg·cm^{-2} and 4.8 mg·cm^{-2} Gd$_2$O$_3$ densities as "Plastic Quad I" and "Plastic Quad II" respectively. The total Gd content in the 1 t array would be approximately 0.17%, w/w and 0.33%, w/w respectively.

We have taken EJ-200/BC-408 [92, 94] as reference for the plastic scintillator. Optical couplings for Scintillator-PMT in the first case and Scintillator-light guide, light guide-PMT in the second case are considered to be done using EJ-500 optical cement.

Important parameters used in simulation for liquid and plastic scintillators are listed in Table 5.1. The parameters listed in the first four rows of Table 5.1 are taken from the data sheets of the respective scintillators. For BC-408, the Birks constant has been measured by Zhang et al [96]. For, the liquid scintillators, we consider the values of the Birks constant determined for BC-505 [93] in Ref. [95]. For scaling the light output of the scintillators with respect to anthracene,

TABLE 5.1: Important parameters used in simulation [14].

Parameter	Liquid		Plastic			Ref.
			Mono	Quad I	Quad II	
Scintillator variant	EJ-331/ BC-521	EJ-335/ BC-525	EJ-200/ BC-408			
Gd conc. (%, w/w)	0.25	0.25	0.17	0.17	0.33	-
Scintillator free proton content ($\times10^{22}$/cm^3)	5.25	6.00	5.23			
Light Output (% Anthracene)	68	55	64			[93, 94]
Bulk light attenuation (m)	4.0	4.5	3.8			
Density (g/cm^3)	0.89	0.88	1.032			
Birks const ($\times10^{-3}$g·cm^{-2}·MeV^{-1})	9.4, 42		11.5			[95]
Detector Mass (tonne)	~0.84		~1			-
Detector volume (m^3)	0.95		1			-
No. of PMT, Diameter (inches)	37, 5		200, 3			-
Photocathode	KCs		KCs			[91]

light output of anthracene has been considered to be 19550 photons/MeV [97].

Quantum efficiency of the photocathode as a function of wavelength has been extracted from the datasheets of photomultiplier tubes from ET Enterprises Ltd. [91]. It is shown in Figure 5.4. Refractive index of the photocathode (KCsSb), both real and imaginary, have been measured by Ref. [98] as a function of wavelength. We have included these values in the simulation to model the detector more accurately. GEANT4 calculates the reflectivity from these values. Scintillator emission spectrum has been extracted from their respective datasheets (Figure 5.4). Bulk light attenuation lengths used for the scintillators have been listed in Table 5.1. The walls of the liquid scintillator tank is considered to be
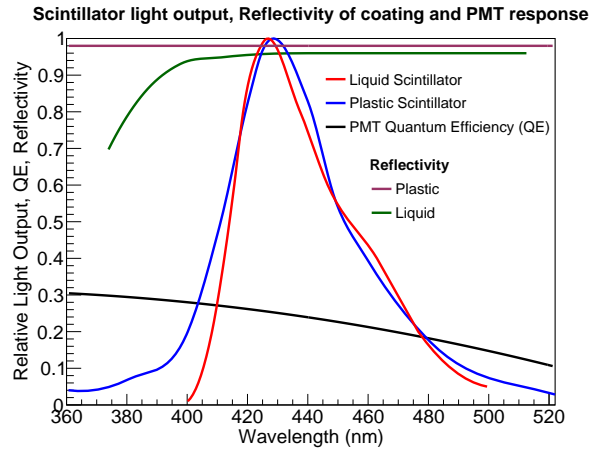
FIGURE 5.4: Light output of scintillators and Quantum Efficiency of PMT Photocath-
ode(QE) used in simulation [14].

coated with a reflective paint BC-622A from Saint-Gobain [99]. Its reflectivity

as a function of wavelength has been included in the simulation. For the plastic,

each bar is considered to be wrapped with a diffuse reflector of 98% reflectivity.

5.3   Simulations

The contribution from each isotope to the total number of fissions occuring in a

reactor at a given instant is given by the fission fraction. For a typical 1 GW_e

power reactor, the fission fraction of the isotopes as a function of the fuel burnup

for a 1 yr cycle is shown in Figure 5.5(a), with data extracted from Ref. [100].

The burnup of a reactor is usually expressed in units of GWd·tHM^{-1}. If a re-

actor operates at a thermal power of 3.125 GW for one year and the total fuel

consumed is 30 t, then the burnup is 3.125 GW × 365 d/30 t = 38 GWd·tHM^{-1}

(gigawatt-day per metric tonne heavy metal), where tHM refers to the mass of

actinides such as Uranium, Plutonium etc.
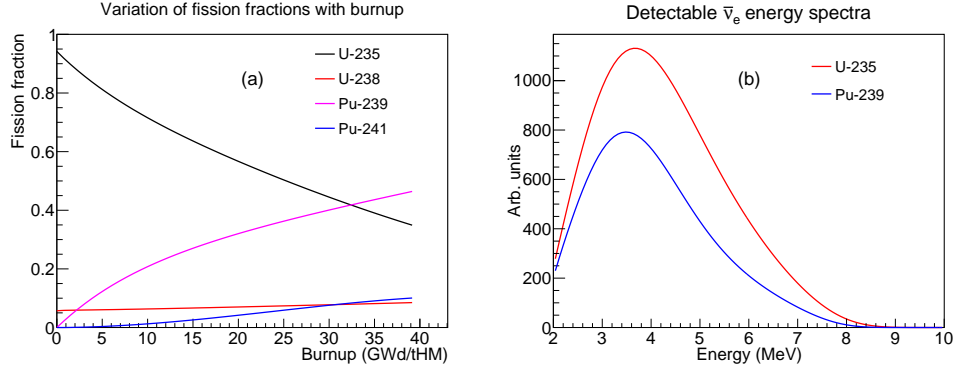
FIGURE 5.5: (a) The fission rate fractions of a typical 1 GW$_e$ reactor with 4% enriched uranium. (b) Energy spectra of neutrinos from ^{235}U and ^{239}Pu detectable by a scintillator detector [14].

Eq. (1.17) can be expanded as

$$N_{\bar{\nu}_e} = \frac{N_p \eta t}{4\pi D^2} \frac{P_{th} \bar{\sigma}_f}{\bar{E}_f} \tag{5.1}$$

to give the total number of neutrino interactions in a given volume of a scintillator detector where, N_p is the number of free protons, η is the efficiency, t is the time interval, D is the source to detector distance, P_{th} is the reactor thermal power. $\bar{\sigma}_f$ is the average cross section and $\bar{E}_f$ is the average energy per fission given by

$$\bar{\sigma}_f = \sum_i \alpha_i \sigma_i \quad \bar{E}_f = \sum_i \alpha_i E_i \tag{5.2}$$

where, $i = 5, 8, 9, 1$ corresponds to the 4 fissioning isotopes, α_i are the fission fractions, E_i is the energy released per fission of each isotope and σ_i the cross section for each isotope [73, 9, 101].

Using the parameterization of neutrino spectrum from Ref. [7] and calculating the cross sections according to Ref. [9, 102], the neutrino spectra detectable by a scintillator detector for a reactor burning pure ^{235}U and pure ^{239}Pu is shown in Figure 5.5(b). As can be seen from Figure 5.5(b), the number of antineutrinos

emitted from the fission of ^{235}U is about ~40% higher than ^{239}Pu at the peak. Depending on the fuel composition, this change of flux as the reactor operates can give information of the state of the fuel burnup in the reactor.

First, we look at the detectors for their ability to capture and detect neutrons. Second, assuming an ideal no background situation we see how the detectors respond to cuts for detecting neutrinos. And lastly we look at the resolution of the detectors. Optical processes are not enabled when we do the first two simulations. Simulated data has been stored and analyzed using the ROOT framework [88].

5.3.1   Neutron capture

The ability of the detectors to capture neutrons is compared by randomly generating neutrons in the active volumes of the geometries. The energy of the neutrons generated are randomly sampled from the neutrino energy spectrum. Fission fractions at the mid point of the reactor power cycle (Figure 5.5(a)) are considered. The neutron capture pattern in the cross sectional view as obtained from GEANT4 is shown in Figure 5.6. Gadolinium doping in liquid scintillators is uniform. In the case of plastic, it is mostly concentrated at the edges of the scintillators where the Gadolinium wrapping exists. The quad variants have a smaller square pattern and is not shown.

Electron antineutrino event after the inverse beta decay reaction (1.16) is characterized by a prompt signal due to the positron (kinetic energy of positron + energy of annihilation gamma) which happens in a very short time, followed by a delayed signal due to the cascade of gamma (upto energy of ~8 MeV)
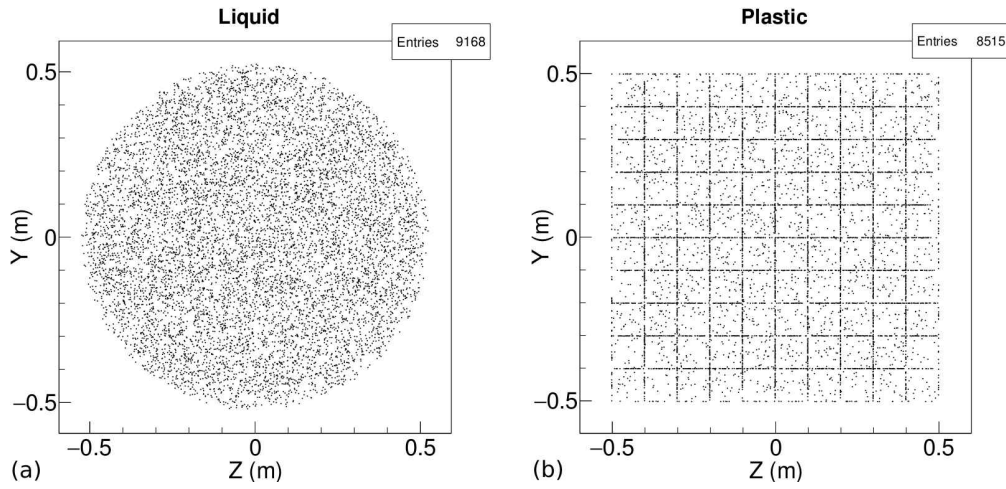
FIGURE 5.6: Neutron capture profile. (a) Liquid. (b) Plastic [14].
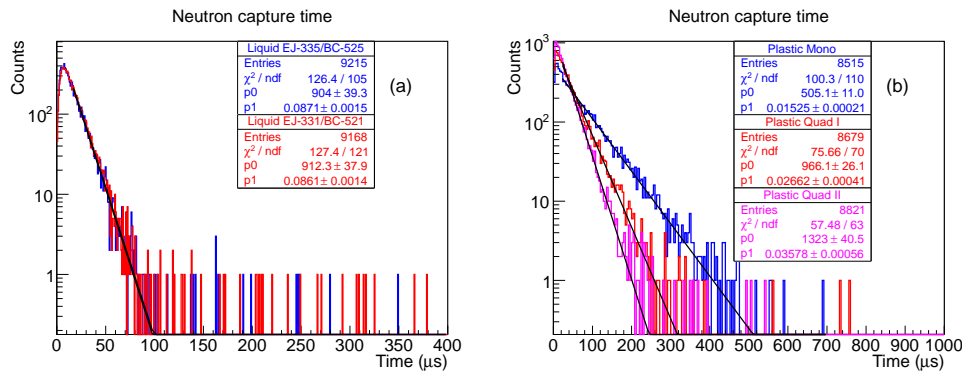
FIGURE 5.7: Mean capture time from exponential fit: (a) Liquid. (b) Plastic [14].

generated by the thermalization and capture of neutron on a high neutron capture cross section element such as 'Gd' or 'H'. The capture of neutron on 'H' would give a single 2.2 MeV gamma ray. The capture time largely depends on the concentration of 'Gd' in the detector. It also depends on its uniformity. 10000 events are generated in the detector volumes. The number of neutron captures and the mean capture time are compared. The comparison is shown in Table 5.2. Neutron capture time distributions are shown in Figure 5.7. To extract the mean

TABLE 5.2: Neutron capture comparison [14].

Neutrons Captured	Liquid		Plastic		
			Mono	Quad I	Quad II
	EJ-331/BC-521	EJ-335/BC-525	EJ-200/BC-408		
Total	9168	9215	8515	8679	8821
Gd	8662	8616	6209	7222	7755
	(94.48 %)	(93.49 %)	(72.91 %)	(83.21 %)	(87.91 %)
H	500	594	2247	1349	1008
	(5.45 %)	(6.44 %)	(26.38 %)	(15.54 %)	(11.42 %)
Time	11.6 μs	11.4 μs	65.6 μs	37.5 μs	27.9 μs

capture time, the distributions are fit with a function of the form

$$P(t) = p_0 \exp(-p_1 t). \tag{5.3}$$

The reciprocal of the parameter p_1 gives the mean capture time. Liquid scintillators show a small mean capture time. Looking at the plastics, the capture time is large in the case of the Mono design and moderate in the case of the Quad variants. The probability of neutron capture increases with increase in granularity and Gd_2O_3 concentration. It also reduces the mean capture time. The probability of capture by hydrogen is more significant in the case of plastic geometry. Commercially available Gadolinium coated aluminized mylar foils come in two types: 2.4 mg·cm^{-2} (single coat) and 4.8 mg·cm^{-2} (double coat) Gd_2O_3 densities.

5.3.2   Neutrino detection efficiency

One of the important tasks in reactor antineutrino experiments is to minimize fake events due to accidental coincidences which may be due to cosmic muons or background radioactivity. Passive shielding for gamma with lead and hydrogenous materials for neutrons will reduce background considerably. However,
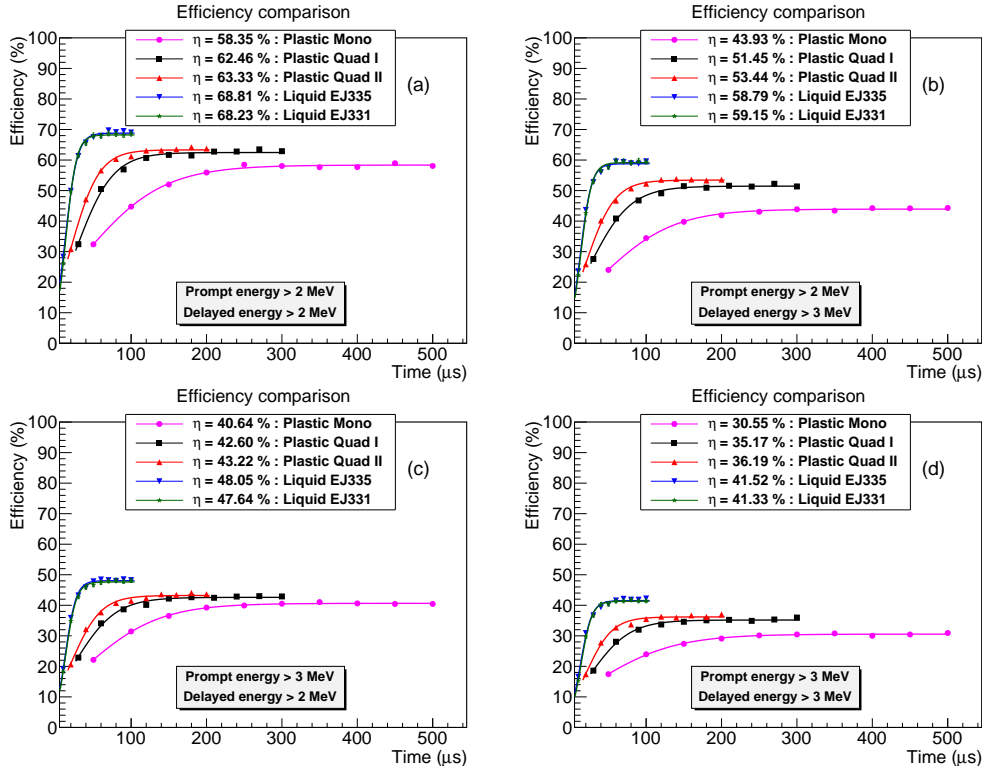
FIGURE 5.8: Variation of neutrino detection efficiency with delayed energy threshold and neutron capture time window [14].

given the distance at which these detectors would be placed, i.e. around tens of meters from the reactor, even when looking for correlated events, the background would be high when compared to the neutrino interaction rate. The correlated time window has to be kept as small as possible to minimize accidental coincidences and not compromise on the efficiency of detection.

As in the previous section, the fission fraction of the isotopes at the mid point of the cycle is considered. Antineutrino event vertex is generated randomly inside the active detector volumes with the antineutrino energy derived randomly from the detectable spectrum of each isotope (Figure 5.5(b)) considering their contribution according to their fractions. The energies of the positron and neu-

tron are obtained from kinematics [102]. The energy deposited by the positron, neutron and their secondaries is then calculated.

Variation of the neutrino detection efficiency with delayed energy threshold (neutron capture gamma + secondaries) and neutron capture time window for 2 MeV and 3 MeV prompt energy thresholds (positron + annihilation gamma and secondaries) are shown in Figure 5.8(a-d). The data points are fit to a sigmoid function to calculate the maximum efficiency. Liquid shows higher efficiency compared to the plastics. The capture of neutron by Gadolinium in liquid is ~20% more than the Plastic Mono and ~8-10% more than the Plastic Quad designs. Also the total number of neutrons captured is higher.

TABLE 5.3: Correlated time window comparison [14].

	Liquid		Plastic		
			Mono	Quad I	Quad II
Scintillator variant	EJ-331/BC-521	EJ-335/BC-525	EJ-200/BC-408		
Prompt energy threshold (MeV)	3				
Delayed energy threshold (MeV)	3				
Maximum Efficiency (%)	41.33	41.52	30.55	35.17	36.19
Minimum correlated time window	60 μs	60 μs	250 μs	140 μs	120 μs

From the plots in Figure 5.8 we should choose a point where the efficiency saturation begins, so that we have the smallest correlation window without compromise in efficiency. The approximate values are listed in Table 5.3. Chance coincidences would be higher in the case of plastic when operating very close to the reactor for physics studies. Fast neutrons from muon spallation also induce correlated neutrino-like signatures. They are usually reduced using muon veto
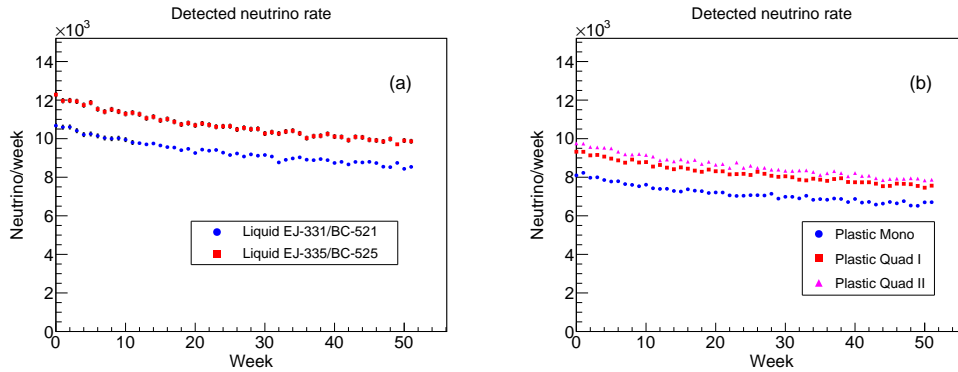
FIGURE 5.9: Variation of neutrino rate with time. (a) Liquid Scintillators (b) Plastic Scintillators [14]. (Error bars are statistical only.)

detectors. Depending on the background at a given place, further cuts will need to be employed reducing the efficiency of both kind of detectors further. Liquid scintillators have higher free proton content compared to plastic scintillators (Table 5.1). More number of antineutrino interactions are possible. Taking these values and substituting into (5.1), the expected neutrino rate over one typical power reactor cycle for the scintillator configurations kept at a distance of 25 m for monitoring purposes is shown in Figure 5.9. The prompt and delayed energy thresholds are kept at 3 MeV and the minimum correlated window from Table 5.3 have been considered. Typically the fuel rods in a Pressurised Water Reactor (PWR) have a length of ∼4 m and the footprint of the assembly is usually less or of the same dimension. So we consider the core as a point isotropic source at a distance of 25 m.

5.3.3 Resolutions

We calculate the energy resolution of the detectors by simulating an isotropic gamma source at the center. The distribution of the total number of photoelec-

trons from all the photomultipliers is fit using the 'Crystal Ball function' [103] which is composed of a Gaussian with a power law tail, to obtain the width σ. Figure 5.10 shows the plot of the resolutions (sigma). Birks constant k_B, is

Scintillator resolutions

Legend:
- *Liquid EJ-331/BC-521 (k_B=42×10^{-3} g cm^{-2} MeV^{-1})*
- *Liquid EJ-335/BC-525 (k_B=42×10^{-3} g cm^{-2} MeV^{-1})*
- *Liquid EJ-331/BC-521 (k_B=9.4×10^{-3} g cm^{-2} MeV^{-1})*
- *Liquid EJ-335/BC-525 (k_B=9.4×10^{-3} g cm^{-2} MeV^{-1})*
- *Plastic Mono*
- *Plastic Quad I*
- *Plastic Quad II*

$\frac{\sigma}{E}\sqrt{\frac{\gamma^2}{E^2}+\frac{\beta^2}{E}+\alpha^2}$
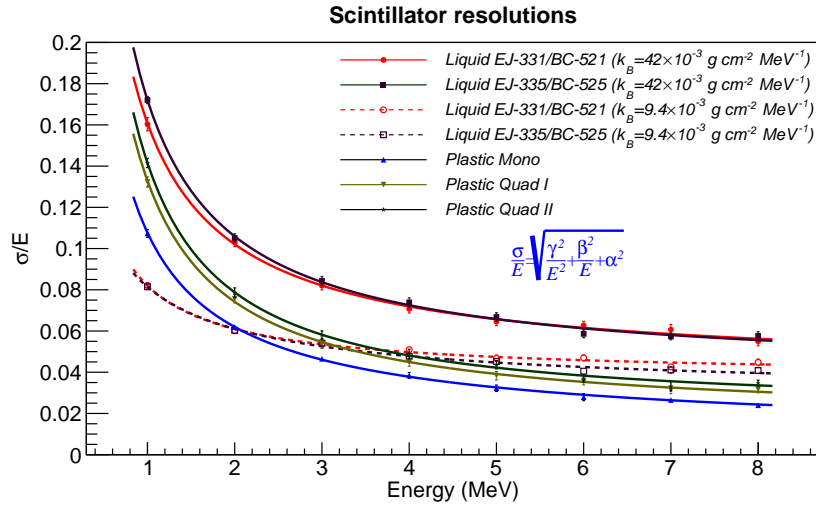
FIGURE 5.10: Detector resolutions [14].

also an important parameter in organic scintillators. It has the effect of reducing the light yield and therefore altering the calibration of detectors. Two different values of k_B have been calculated in Ref. [95] for BC-505 liquid scintillator (Section 5.2, Table 5.1). The resolutions have been simulated for both these values. Resolution function of the form

$$\frac{\sigma}{E} = \sqrt{\frac{\gamma^2}{E^2} + \frac{\beta^2}{E} + \alpha^2} \qquad (5.4)$$

has been used to fit the data where, α is related to the geometrical influences, β the statistical fluctuation of the light production and γ to electronic noise [104].

Coverage area for the liquid design considered (6.5 %) is less than the plastic (12.8 %). So, for energies greater than 3 MeV, the Plastic Mono design shows the best resolution. Resolution function plotted for the liquid design for

both scintillator variants show comparable resolutions with the plastics when $k_B = 9.4 \times 10^{-3}$ g·cm^{-2}·MeV^{-1}. It is worse with $k_B = 42 \times 10^{-3}$ g·cm^{-2}·MeV^{-1}. Increased Gd_2O_3 concentration in the foils, reduces resolution of the plastic designs.

5.3.4   Expected count rate with ISMRAN at Dhruva

Dhruva research reactor has a designed capacity to operate at 100 MW$_{th}$. The fuel is natural Uranium. Fission fractions at the mid point of the cycle in the case of a cylindrical natural uranium reactor as extracted from Ref. [100] are

$\alpha_5 : \alpha_8 : \alpha_9 : \alpha_1 :: 0.5276 : 0.0546 : 0.4023 : 0.0146.$

Considering the reactor as a point source, detector efficiency $\eta = 0.30$, distance $D = 13$ m, $t = 86400$ s, and using equations (5.1) and (5.2), the calculated event rate with ISMRAN is ~115 events per day.

5.4   Summary

Performance of liquid and plastic scintillator detector designs for detecting antineutrinos have been compared using GEANT4 simulation package. Owing to the higher proton content, the event rate in liquid scintillator detectors are higher compared to the plastic. More statistics can be achieved for the same duration. Most of the scintillation detectors employed around the world for neutrino physics are liquid based and have large volumes. They are cheaper compared to the plastic array and have pulse shape discrimination ability. However, they have toxicity, long term stability and flammability concerns.

In the case of reactor monitoring and very short baseline neutrino physics, a ton scale detector would be sufficient. Although a little expensive, measurements with the plastic scintillator are feasible. They do not have flammability concerns. They are easy to handle and have no stability issues. These factors are very important if the detector is to be mounted on a mobile unit. The Quad plastic design reduces the correlated time window thereby reducing accidental backgrounds. However, with a wrapping of 4.8 mg·cm^{-2} of Gd_2O_3 density, there is further reduction in the time window, but at the expense of resolution. The neutrino detection efficiency is somewhat lower than that of the liquid scintillator but manageable.

A prototype called 'Mini ISMRAN' (India's Scintillator Matrix for Reactor AntiNeutrino) will be setup near the research reactor at BARC, with 20 plastic bars of Mono Design at a distance of ~13 m with the aim towards setting up a 1 t detector.

Background measurements

Knowledge of the background and its reduction is of paramount importance in neutrino experiments. The major sources of background for reactor anti-neutrino experiments are from natural gamma radioactivity, cosmic rays and neutrons both thermal and fast. In the case of sterile neutrino search where the detector has to be placed a few tens of meters from the reactor, the background is very high and needs lot of shielding.

6.1 Sources of background

6.1.1 Gamma

Naturally occurring radioactive elements are present as impurities in structural materials. The most important components are potassium, thorium, uranium and the members of the long decay chains of uranium and thorium. Natural potassium contains a few percent of ^{40}K, which beta decays subsequently emitting a characteristic gamma ray of energy 1460 keV. It also has a long half life of ~ 1.2

billion years.

The daughters in the decay chains of thorium - ^{228}Ac, ^{224}Ra, ^{212}Tl, and ^{208}Tl and uranium - ^{226}Ra, ^{214}Pb and ^{214}Bi contribute to the background [105]. A prominent gamma ray of 2614 keV usually observed during background measurements is from ^{208}Tl. Both the ^{40}K and ^{208}Tl lines serve as natural calibration points for detectors.

Apart from the gamma rays described above, background at nuclear reactors contains much more gamma radioactivity extending beyond 3 MeV up to 10 MeV. These gamma rays are produced by the radiative capture of neutrons on various materials in the surrounding environment such as support structures, claddings, walls, shielding and instruments.

6.1.2   Cosmic

Cosmic Muons

Cosmic rays are predominantly composed of protons (~90 %). When they pass through the earths atmosphere, their collisions with the atmospheric atoms and molecules, produces hadrons like pions ($\pi^{\pm,0}$) and kaons ($K^{\pm,0}$). Decay of these pions and kaons produce muons. The average energy and number of cosmic muons falling at sea level is roughly ~4 GeV and 1 cm^{-2}·min^{-1} respectively. Muons are unstable and decay with a mean lifetime of 2.2 μs producing electrons and neutrinos.

Muons decay almost always at rest (small fraction can decay in flight). Due to the large size of ISMRAN (~1 ton and 1 m^3) and its dense shielding (Lead and Borated Polyethylene), its decay probability increases inside the detector

volume. A muon entering ISMRAN will give a prompt signal and the electron after its decay can provide a delayed signal. These correlated events will mimic anti-neutrino signals from the reactor. So extreme care has to be taken to filter out muon events from the anti-neutrino events.

6.1.3   Neutron

Neutrons can be classified based on their energy range. It is shown in Table 6.1. Reactor anti-neutrino experiments are concerned about neutrons in the range from thermal to fast.

TABLE 6.1: Terminology and energy range of neutrons [106].

Energy Range	Name
0.0 - 0.025 eV	Cold neutrons
0.025 eV	Thermal neutrons
0.025 - 0.4 eV	Epithermal neutrons
0.4 - 0.6 eV	Cadmium neutrons
0.6 - 1 eV	Epicadmium neutrons
1 - 10 eV	Slow neutrons
10 - 300 eV	Resonance neutrons
300 eV - 1 MeV	Intermediate neutrons
1 - 20 MeV	Fast neutrons
> 20 MeV	Ultrafast neutrons

Cosmogenic neutrons

Neutrons are produced when muon and the nuclei in the surrounding materials undergo spallation reaction. In this reaction, a muon exchanges a virtual photon with a nucleus. The nucleus then emits hadrons such as neutrons and pions. Secondary neutrons are also emitted by the interaction of the primary pions and

neutrons with nuclei. Feynman diagram for the interaction is shown in Figure
6.1.
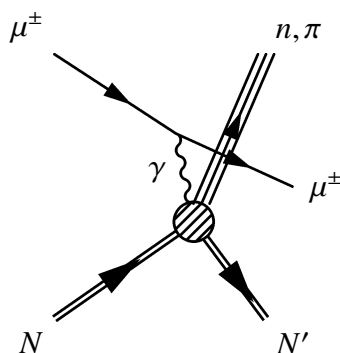
FIGURE 6.1: Feynman diagram for the muon spallation reaction.

The neutrons range in energy from thermal to GeVs with a flux sharply de-
creasing. It becomes a concern for detectors with a lot of shielding as the proba-
bility of muon spallation will be more. Fast neutrons scatter elastically with free
protons transferring most of their energy to the proton. If the energy of the pro-
tons is enough, they could appear as a prompt event. The neutron subsequently
thermalizes and gets captured radiatively giving a delayed signal.

Reactor correlated fast neutrons

Reactor correlated fast neutron backgrounds can also be present. They are neu-
trons which escape the shielding of the reactor and are usually small in number.
They are directly related to the fission processes happening in the core and have
energies lesser than 10 MeV. Before coming out of the biological shield, they
loose a significant amount of energy and are not of much concern for correlated
signatures if proper thresholds are applied. However, they can still contribute to
accidental singles rate.

6.2 Measurements

The site for the proposed ISMRAN at Dhruva reactor hall is shown in Figure 6.2. Distance from the center of the core is ~13 m. A total footprint of 3 m × 3 m has been allotted. A bar to denote the orientation of the setup and references to certain positions which will be used later are shown. 'N'(Near) represents the side near to the neutron guide tube 'GT'. 'F'(Far) represents the side far from GT. 'M'(Middle) represents the position in between F and N.
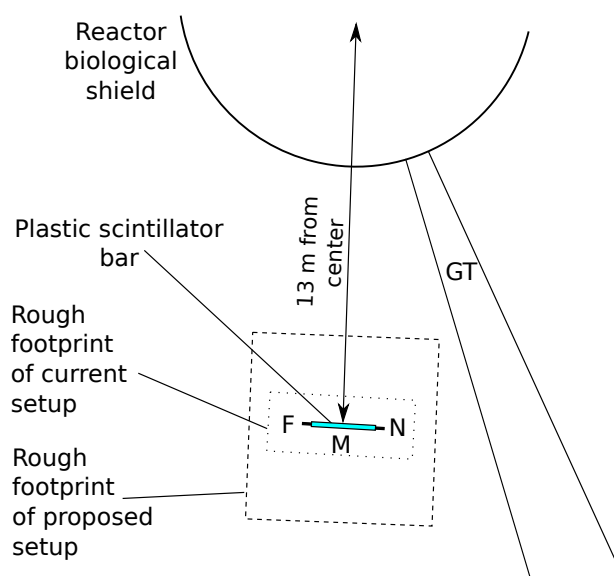
FIGURE 6.2: The proposed site at the Dhruva reactor hall for ISMRAN.

12 Plastic scintillator bars similar to the proposed design but smaller in size $(100 \times 6 \times 6)$ cm^3 were used in an experiment at BARC-TIFR Pellertron Linac facility at TIFR for neutron TOF measurements. They were shifted to Dhruva to perform preliminary measurements. Since these bars did not have Gadolinium coated mylar foils, they were procured from Euro Collimators, UK. Each of the bars were wrapped with these foils. Initial setup was with 5 cm lead shielding

with a single bar inside it. The current setup is shown in Figure 6.3(a, b).

<div align="center">(a)   (b)</div>

FIGURE 6.3: The current setup with 12 plastic scintillator bars, lead and borated rubber
            shielding

Gamma, neutron and correlated event measurements were done using differ-
ent detectors.

6.2.1   Gamma

To have an idea about the gamma background at the site, a BGO detector was
used. The crystal was 6.3 cm thick with a regular hexagonal cross section, having
width of 5.6 cm between opposite faces. Detector assembly was from Scionix
Ltd.

Data was acquired with the BGO kept at the proposed site on the table shown
in Figures 6.3 when the reactor power was 70 MW. The detector had been cali-
brated using standard sources such as ^{60}Co, ^{22}Na and ^{137}Cs. High energy gamma
background beyond 3 MeV are observed. It is shown as a black histogram in
Figure 6.4.
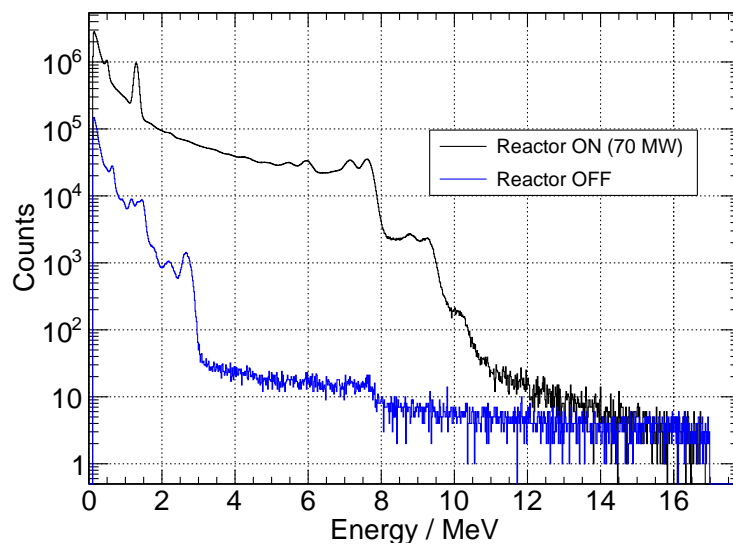
FIGURE 6.4: Gamma background when the reactor is ON and OFF. (*Duration: 5 hrs*)
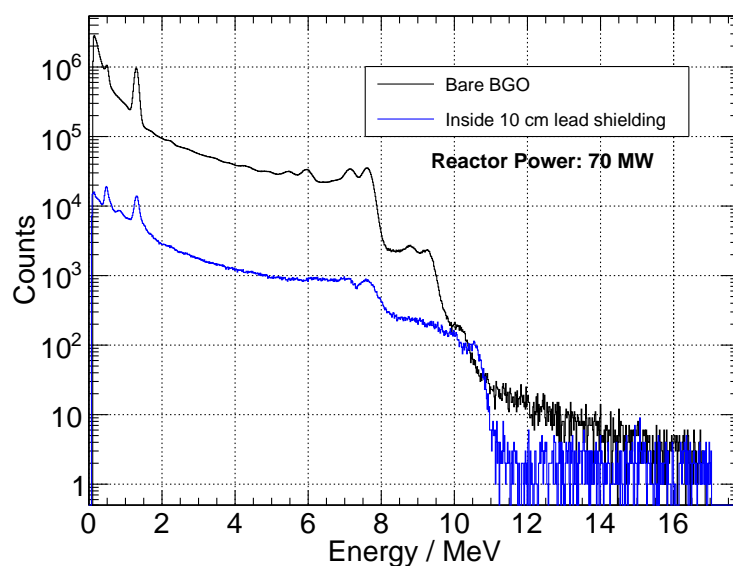
FIGURE 6.5: Gamma background with and without shielding. (*Duration: 5 hrs*)

These gamma rays are due to the radiative capture of thermal neutron on various elements in the environment as mentioned in Section 6.1.1. Most of the peaks are from neutron capture on iron present in support structures, equipment

and walls. Gamma background in the reactor off condition was also measured.

The blue histogram in Figure 6.4 shows the spectrum when the reactor is OFF. The gamma background is drastically reduced. High energy gamma beyond 3 MeV are almost gone.

BGO detector in lead shielding

A lead castle of 10 cm thickness was made, and the BGO detector was placed inside it. The spectrum is shown in Figure 6.5.

An order of magnitude reduction in the yield was observed.

Variation of gamma background with position

To see if there is any variation in the gamma background at different positions, the BGO detector without any shielding was placed at Near, Far and Middle positions of the setup as denoted in Figure 6.2. The spectra are shown in Figure 6.6.

It can be seen that the gamma rate is more at the 'Near' position compared to 'Far' and 'Middle'. The gamma background at reactor hall does not appear to be uniform near the setup.

Since the resolution of BGO is poor, improved measurements need to be done using detectors like HPGe or LaBr$_3$ (Lanthanum Bromide).

6.2.2   Thermal neutrons

To understand the thermal neutron background, measurements were done using a cerium doped Lithium Yttrium Borate (LYBO) - Li$_6$Y(BO$_3$)$_3$:Ce(0.2%) -
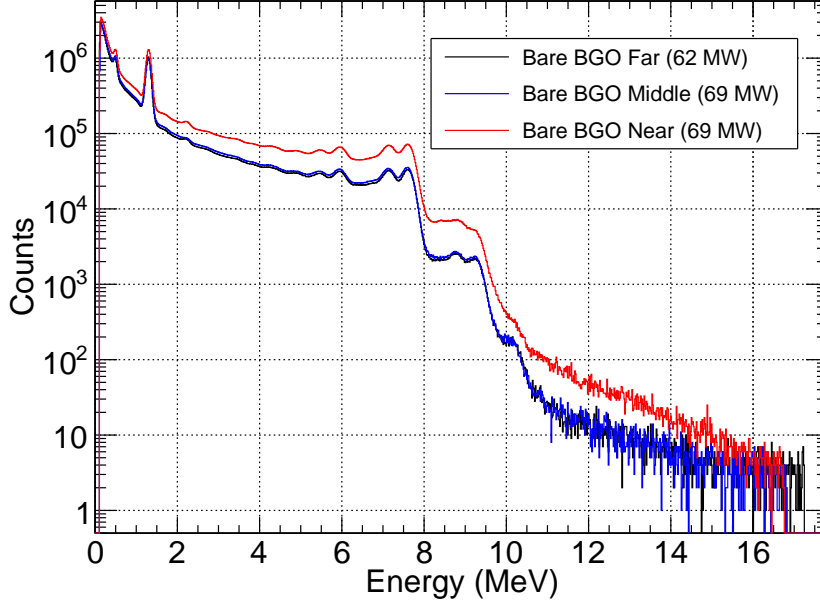
FIGURE 6.6: Gamma spectra at various positions near the setup. (*Duration: 5 hrs*)

detector. The crystal of 1 mm thickness and 10 mm diameter was developed at Crystal Technology Lab, Technical Physics Division, BARC [107]. Lithium and boron both have high thermal neutron absorption cross section. The detector has an efficiency >85 % for thermal neutrons. Neutron capture reactions are [107]

1. On Boron (^{10}B) :

$$^{10}_{5}\text{B} +^{1}_{0} n \rightarrow^{7}_{3} \text{Li} +^{4}_{2} \alpha \ (Q\text{-value} = 2.79 \text{ MeV, ground state})$$

$$^{10}_{5}\text{B} +^{1}_{0} n \rightarrow^{7}_{3} \text{Li}^* +^{4}_{2} \alpha \ (Q\text{-value} = 2.310 \text{ MeV}) \tag{6.1}$$

$$^{7}_{3}\text{Li}^* \rightarrow \gamma \ (0.48 \text{ MeV})$$

2. On Lithium (^{6}Li) :

$$^{6}_{3}\text{Li} +^{1}_{0} n \rightarrow^{3}_{1} \text{H} \ (2.75 \text{ MeV}) +^{4}_{2} \text{He} \ (2.05 \text{ MeV}). \tag{6.2}$$
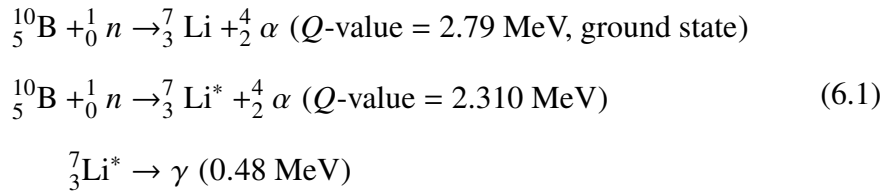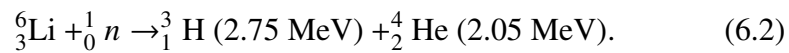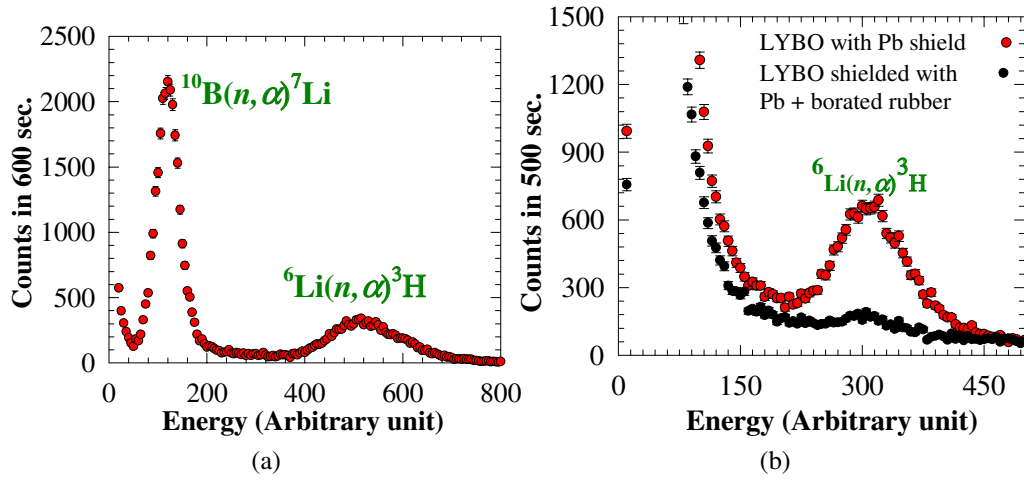
FIGURE 6.7: (a) LYBO response to a calibrated thermal neutron source. (b) Effect of borated rubber. [108]

Natural abundance and thermal neutron absorption cross sections of ^{10}B, ^{6}Li are 7.4% and 0.940 kb, 20% and 3.835 kb respectively. An average energy of 2.5 MeV is deposited in the case of capture on Boron and 4.8 MeV of energy is deposited in the case of capture on Lithium. Due to the formation of two lighter particles in (6.2), the number of scintillation photons generated is more in the case of capture on Lithium as compared to Boron [107]. This can be seen in Figure 6.7(a).

LYBO detector was placed near a thermal neutron beam port at Dhruva reactor which provides a thermal neutron flux of $\sim 10^6$ cm^{-2}·s^{-1}. Due to the large gamma background the detector was placed behind a 20 cm thick lead wall. Figure 6.7(b) shows the peak due to the thermal neutron capture on lithium and the effect when 3 mm thick borated rubber (40% boron) is placed in front of it. After calibration, the detector was placed at Near, Far and Middle position of the setup. No variation in the thermal neutron flux was observed within ±5 %. The

spectra are shown in Figure 6.8. Thermal neutron rate in the reactor environment is roughly ~5-7 cm^{-2}·s^{-1} at ~85 MW reactor power and appears to be uniform.
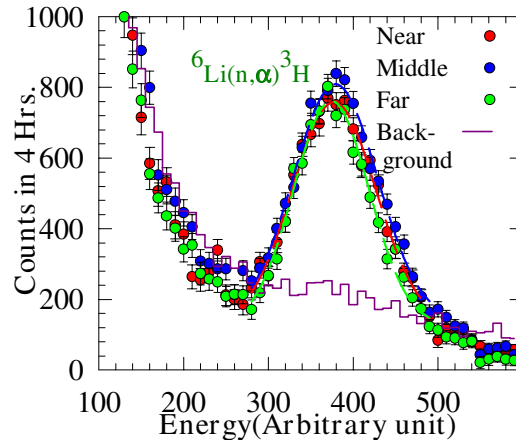
FIGURE 6.8: Thermal neutron spectra measured using LYBO detector at Far, Near and Middle positions. [108]

6.2.3 Correlated events

In the setup shown in Figure 6.3, two bars in the middle were used to do correlated time measurements or neutrino event like measurements [109]. A Time to Amplitude Converter (TAC) was used. Logical AND of the signals from two PMTs of the top bar was connected to the START and the same of the bottom bar was connected to the stop. TAC was calibrated with the help of an oscilloscope and a function generator with coupled channels.

Data was recorded both in the reactor ON and OFF conditions. When the reactor is OFF, singles rate due to ambient gamma radiation is lesser. Hence an exponential form of the time distribution over a constant background can be easily noticed as shown in Figure 6.9(a). When the reactor is ON, the gamma background is overwhelming. The same nature cannot be observed due to in-

creased accidental coincidences. The TAC distribution when reactor is ON is
shown in Figure 6.9(b).
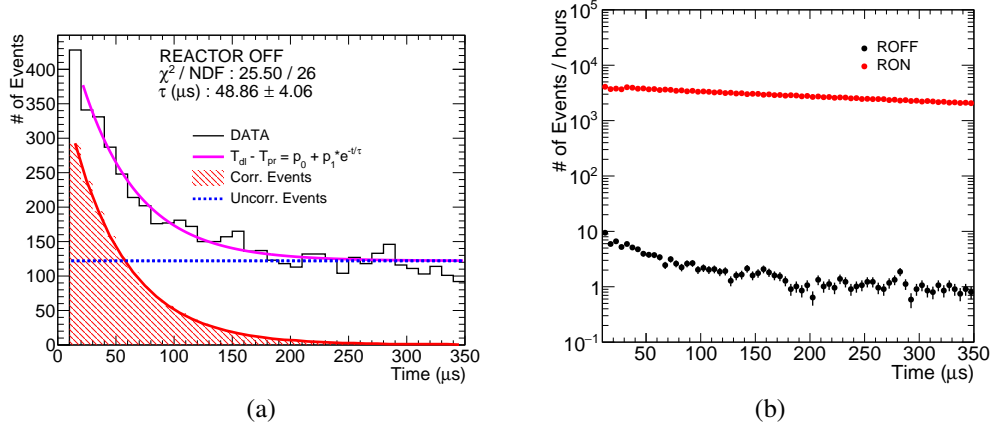
FIGURE 6.9: (a) Time distribution of correlated events when reactor is OFF. (b) Time
distribution of correlated events when reactor is ON.

In Figure 6.9(a), the red curve with the shaded region shows the correlated
events. It is obtained by subtracting the uncorrelated events (random coinci-
dences) shown as the blue dotted line, from Data - black histogram. The time
difference between START (prompt) and STOP (delayed) shown in Figure 6.9(a)
is fitted with an exponential function (pink color)

$$T_{\mathrm{dl}} - T_{\mathrm{pr}} = p_0 + p_1 \exp(-t/\tau) \tag{6.3}$$

where, T_{dl} is the STOP (delayed) time, T_{pr} is the START (prompt) time, p_0, p_1
are constants and τ is the mean decay time. p_0 characterizes the uncorrelated
events. The correlated events in the reactor OFF case may be due to spallation
neutrons and cosmic muons.

Background reduction with coincidence and shielding

The event rate in the bars were compared in different conditions. Logical AND was done between the 2 PMTs of the bar and count rates with Pb and Borated Rubber (BR) shielding are shown in Table . No threshold cuts were applied.

TABLE 6.2: Reduction in background with coincidence and shielding.

Reactor Power (80 - 85 MW)	Count Rate (Hz)
No Shielding (single bar)	30000
10 cm Pb (single bar)	2000
10 cm Pb (Coincidence 2 bars)	300
10 cm Pb + 1 cm (5 mm + 5 mm) BR both inside and outside	70

Around an order of magnitude reduction is observed in each case going from one condition to the other. Borated Rubber has a doping of 50 % boron.

In the actual experiment, a spectrum comparable to that shown in Figure 6.9(a) has to be achieved in the reactor ON condition. Efficient shielding, threshold cuts, multiplicity and proper event logic will help in reducing the background.

6.2.4 Fast neutrons

A liquid scintillator was used to estimate the fast neutron background. The detector had a diameter of 5″ containing EJ-301 (NE-213) liquid scintillator. Pulse shape discrimination technique was used to differentiate between gamma and neutrons. Data was acquired using CAEN 1730 digitizer with DPP-PSD (Digital Pulse Processing - Pulse Shape Discrimination) firmware [110]. The digitizer has a sampling rate of 500 MS/s and a resolution of 14 bit. Data was acquired by

placing the detector with and without lead shielding. Charge integration method
was used to perform PSD.

The PSD parameter is defined as

$$\text{PSD} = 1 - \frac{Q_S}{Q_L} \tag{6.4}$$

where, Q_S is the charge integrated in the short gate and Q_L is the charge inte-
grated in the long gate. The gates were optimized using an Am-Be source in
a non reactor environment at the lab. It was calibrated using ^{60}Co and Am-Be
sources.

When the detector was placed without shielding, the gamma background was
large, contaminating the neutron part of the PSD spectrum. When the detector
was placed inside lead shielding, reduction in both gamma and neutron rate was
observed. Lesser gamma contamination in the neutron region is seen. A change
in the PSD parameter is also seen. The PSD parameter under both conditions as
a function of electron equivalent energy is shown in Figure 6.10(a,b).
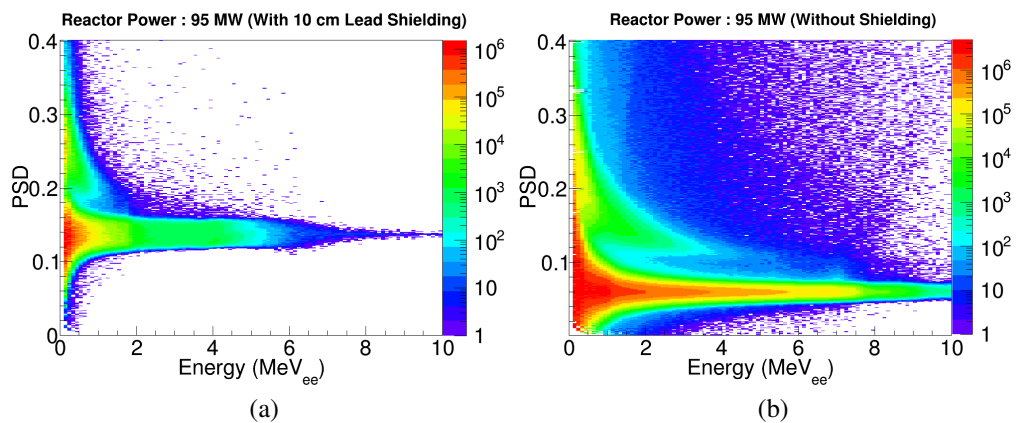
FIGURE 6.10: PSD parameter as a function of energy. (a) Inside lead shielding. (b) Out-
side lead shielding.

Background rate with reactor power

Data was acquired over extended period of time of around 2 weeks so that the reactor ON and OFF cycle could be included. Figure 6.11 shows the variation of neutron and gamma rate with the reactor power. Well defined steps corresponding to the power ramp up can be seen.
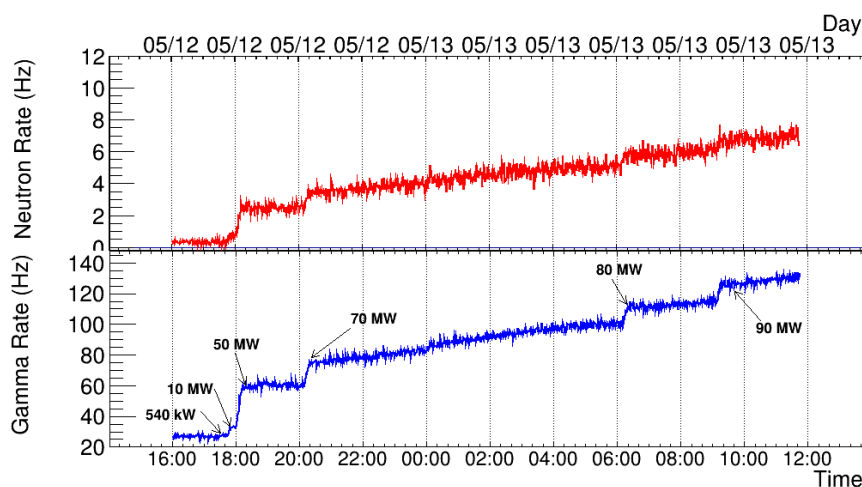
FIGURE 6.11: Correlation of background with the operator reported reactor power.

Background rate with threshold cut

Figure 6.12 shows the background rate at the reactor. Rate at three different threshold cuts of 0.12, 1.8 and 2.6 MeV_{ee} are shown. The detector was placed on the table without any shielding and the reported reactor power was 95 MW. The square shaped dip in the spectra correspond to the reactor ON-OFF cycle.

At the same reactor power of 95 MW, the detector was placed in a castle of lead of 10 cm thickness + 1 cm of borated rubber. Background rates for gamma and neutron in this condition are shown in Figure 6.11(a) and Figure 6.11(b) respectively.
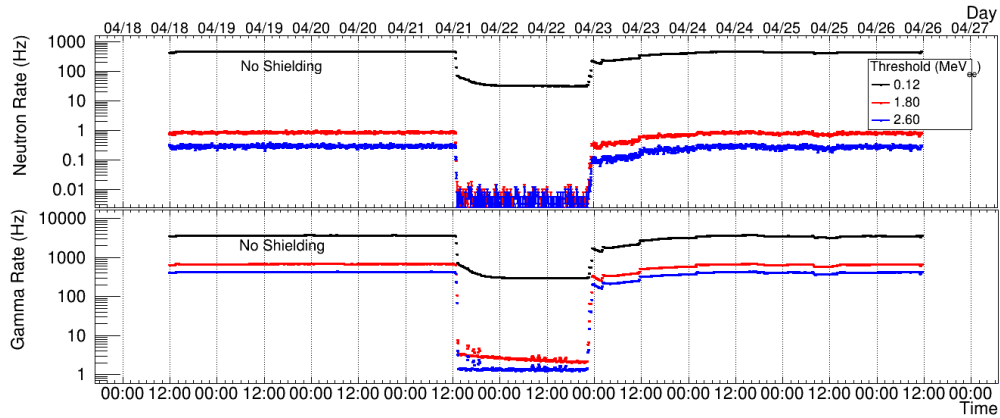
FIGURE 6.12: Gamma and neutron background rate at different threshold cuts.

The total surface area of the scintillator is ~450 cm^2. Using a cut of PSD> 0.185 on the PSD parameter in Figure 6.10(a), the rough fast neutron rate is estimated to be ~4 ×10^{-6} Hz·cm^{-2} at a thermal power of 95 MW. It is to be noted that this number has not been corrected for the efficiency of the detector. Also, at a threshold of 2.6 MeV$_{ee}$, both gamma and neutron rate do not depend on reactor power profile.

Again, by shielding the detector with lead, BR and applying threshold cuts, substantial background reduction is seen.

6.3   Summary

Gamma, thermal and fast neutron background and also correlated event measurements have been performed using various detectors. The gamma background at the reactor site measured using BGO detector shows gamma radiation upto 10 MeV energy. Shielding with 10 cm lead reduces the total background by a little more than an order of magnitude. Non uniformity in the gamma background was observed when the detector was placed at various positions.
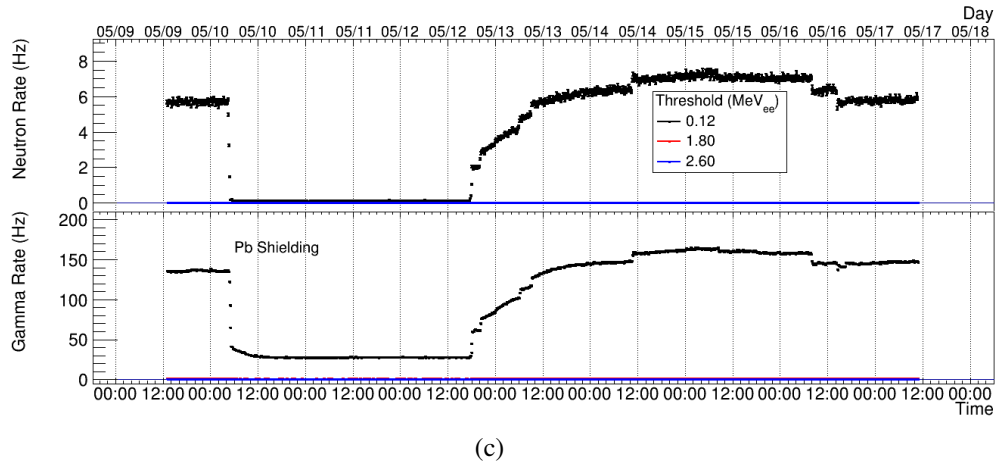
(c)
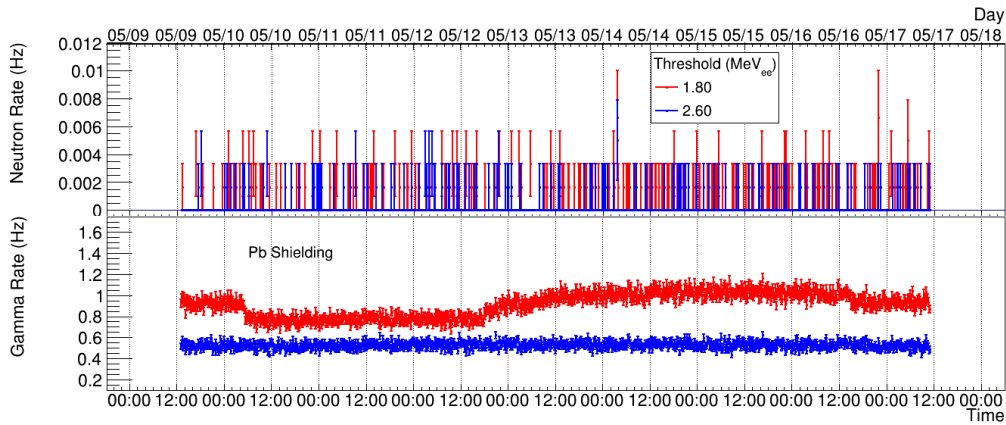
(d)

FIGURE 6.11: Reduction in background with threshold cut. (a) With Lead Shielding. (b) With Lead Shielding (Zoomed)

Thermal neutron background in the reactor hall has been measured using LYBO detector. The thermal neutron rate in the hall is roughly around 5 neutrons $cm^{-2} \cdot s^{-1}$ at a power of ~80 MW. The thermal neutron background appears to be uniform near the setup with no positional variation.

Correlated event measurements were done using plastic scintillator bars of smaller dimension wrapped with Gadolinium foils. In the reactor OFF condition, correlated events could be observed with a mean decay time of ~48 µs.

Using combinations of shielding and bringing more bars in coincidence background reduction of ~3 orders of magnitude from a condition without shielding is observed.

Fast neutron measurements were done using 5″ EJ-301/NE-213 liquid scintillation detector. Digitizer based acquisition with DPP-PSD firmware was used. Reactor correlated neutrons are observed. Correlation in the background rate with reactor power is seen over a reactor ON-OFF cycle. Efficiency uncorrected fast neutron count rate at a threshold of 2.6 MeV is ~4 $\times 10^{-6}$ Hz·cm^{-2}. Using proper threshold cuts, substantial reduction of fast neutron background can be done.

Conclusions and Future scope

CHAPTER 7

Conclusions

Neutrinos are messengers of physics beyond the standard model. The phenomenon of neutrino oscillation has been confirmed but precision measurement of the oscillation parameters need to be done. Precision measurements can help us deduce neutrino mass ordering and also help us understand the matter-antimatter asymmetry in the universe. The 50 kt magnetized ICAL detector at INO aims to do the same using atmospheric neutrinos. When fully built, it would be the largest electromagnet in the world. RPCs are the elements of this detector. Approximately 30000 RPCs would be needed for the ICAL detector.

RPCs are fast and efficient detectors (>95 %). They can cover large areas, inexpensive and simple to construct.

Neutrinos can be used to monitor reactors remotely and check nuclear proliferation. Due to results from experiments [68] and certain anomalies such as the Reactor Anti-neutrino Anomaly [9], the existence of sterile neutrino is a possibility. Research in this direction may lead to its discovery or better understanding of reactor physics.

Studies on RPCs

Hodoscope

A plastic scintillator based hodoscope has been instrumented. Using this hodoscope multiple RPCs can be characterized for functional parameters such as efficiency, clustersize, strip profile and timing characteristics. Maximum dimension of the RPCs that can be handled by this hodoscope is 1 m × 2 m. Hodoscope is equipped with gas lines, HV cables and shelves for placement of RPCs for simultaneous characterization. For an experiment like ICAL at INO, hodoscopes such as this at multiple centres are necessary because of the unprecedented scale of deployment of RPCs.

RPCs with G10 readouts

The space allocated for RPCs in the ICAL detector at INO is 4 cm. Readouts based on polycarbonate honeycomb sandwich that is being considered for RPCs at ICAL is 5 mm thick. With the gas gap of 8 mm thickness and supporting trays, the total thickness could reach up to 3 cm. This could create problems in handling. To find a thinner solution, G10 readouts of 1 m × 1 m area with thickness of ~1 mm was obtained from a local vendor in Mumbai.

RPC with G10 readout has been characterized and its performance is good. To match the impedance of the readout strips with the front-end electronics based on HMCs, resistive circuit has been employed. RPCs with these readouts show an efficiency of 95% and a mean clustersize of 2 strips. A time distribution width of ~2 ns between the time of the trigger and RPC signals including the variation due to strip and cable delays, field non-uniformities and muon interaction posi-

tion is obtained.

ANUSPARSH ASIC

RPC assembled with polycarbonate honeycomb readouts have also been tested
with ANUSPARSH ASIC based front-end electronics developed by Electronics
Division, BARC for fast detectors. The results are comparable with that mea-
sured with G10 and Hybrid Micro Circuit (HMC) based pre-amplifiers. RPC
efficiency of 96 % has been obtained using the two variants of ANUSPARSH:
ANUSPARSH - II trans-impedance amplifier and ANUSPARSH - III voltage
amplifier. Time distribution width of 2.5 ns between the time of the trigger and
RPC signals has been observed.∎

The operating point of the RPC depends on the gas composition, discrimina-
tor threshold, and the type of readout (transmission loss, impedance matching
etc.). Higher voltage increases the noise rate but improves the time resolution of
the RPC when operated in the avalanche mode. Considering the gas composition
to be the same, the operating point for RPC using the different electronics and
readouts are given in Table 7.1.

TABLE 7.1: Operating point of RPC with different electronics and readouts.

Electronics	HMC	ANUSPARSH - II	ANUSPARSH - III
Readout	G10	Polycarbonate honeycomb	
Operating Point (V_{eff})	10200	9700	9400

G10 readouts are expensive compared to polycarbonate readouts being con-
sidered for ICAL at INO. Since a huge number of RPCs are required for the
ICAL detector, their cost could be reduced considerably. Dimension of G10

readouts that can be manufactured in India are limited to 1 m × 1 m. For a dimension that is needed for ICAL at INO i.e. 2 m × 2 m, procedures have to be developed.

Studies for reactor anti-neutrino

Simulations on Liquid and Plastic scintillation detectors

Liquid and plastic scintillation detectors have been compared through simulations using the GEANT4 framework. Different designs and scintillator variants have been considered.

Plastic scintillator based detector shows a maximum efficiency of 30% at prompt and delayed thresholds of 3 MeV. Liquid scintillator variant shows 40% efficiency at the same threshold. However, the granular variants of the plastic design i.e. Plastic Quad I and Quad II show ~35 % efficiency. The correlated time window in the case of plastics is more compared to that of liquid. The Plastic Mono, Quad I and Quad II designs require a minimum correlated time window of 250 μs, 140 μs, and 120 μs; whereas, liquid designs require a minimum correlated window of only 60 μs.

Among the designs considered, due to the larger coverage area, plastic scintillators show better resolutions compared to the liquid.

Plastic scintillator based detectors are preferable when it comes to safety and mobility. Their performance is slightly poor compared to liquid but manageable. Due to the mobile nature of the proposed detector, its proximity to the reactor, and simplicity, we will be setting up a detector with the plastic mono design.

Background Measurements

Preliminary background measurements have been done at the proposed site for the reactor anti-neutrino detector. The sources of background is mainly due to gamma generated after the radiative capture of neutrons in the surrounding support structures and walls.

Gamma background at the reactor site has been measured using BGO detectors. Variation of the gamma rate at few positions near the proposed site has been observed.

Thermal neutron measurements have been done using LYBO detector developed by Crystal Technology Lab, Technical Physics Division, BARC. No variation in thermal neutron background with respect to position is seen. The thermal neutron rate is roughly estimated to be 5-7 $cm^{-2} \cdot s^{-1}$ at a reactor power of 85 MW.

Correlated event measurements were done using smaller plastic scintillator bars kept in a lead shielding of 10 cm thickness. In the reactor OFF condition, correlated events were observed above background due to random coincidences with mean decay time of 48 μs.

Fast neutron measurements have been done using 5″ EJ-301/NE-213 liquid scintillator with digitizer based acquisition system. Reactor correlated neutron background is seen when the detector is shielded by lead. The fast neutron rate without efficiency correction has been estimated to be ~4×10^{-6} Hz·cm^{-2} at an energy threshold of 2.6 MeV and reactor power of 95 MW.

Future Scope

ICAL and RPCs

Bakelite RPCs: Bakelite is another material used in RPCs. They have certain advantages when compared to glass. They are lighter, relatively flexible and have bulk resistivity an order of magnitude lesser. Handling is easier. The scale of RPC deployment is enormous in the case of ICAL at INO. So it would be worthwhile to explore the possibility of using bakelite RPCs in INO. This would require the identification and collaboration with Indian bakelite industries, testing and benchmarking of bakelite RPCs produced in India.

In this regard 1 m × 2 m bakelite RPCs shown in Figure 8.1 have been procured from General Tecnica, Italy for benchmarking. Parallely, bakelite procured in India are being fabricated into gas gaps for RPCs by a local company in Mumbai to be assembled and tested. The resistivity of Indian bakelite samples have been measured and found to be 10^{11} Ω·cm [111]. The setup and resistivity graph are shown in Figure 8.2(a) and Fig-

FIGURE 8.1: Gas gaps being made in Italy.

ure 8.2(b) respectively.

G10 readouts: Large area fabrication of the current G10 readout is diffi-
cult. Also G10 readouts are costlier than the polycarbonate honeycomb
readouts being considered for ICAL at INO. Looking at the large volume
fabrication needed for ICAL, the cost could be reduced considerably. If
G10 readouts are to be used for RPCs of the size of RPC being considered
for INO (2 m × 2 m), the technique of fabricating atleast 1 m × 2 m read-
outs must be established or a method to combine smaller readouts to cover
the whole are has to be devised; keeping in mind that number of electronic
channels are not increased.

ANUSPARSH: Only few boards of ANUSPARSH ASICs have been fabri-
cated. So it was difficult to have access to them to perform RPC charac-
terization. Systematic measurements have to be performed. Clustersize
measurements using ANUSPARSH need to be done.

Muon Tomography: RPCs are potential candidates for use as detectors for
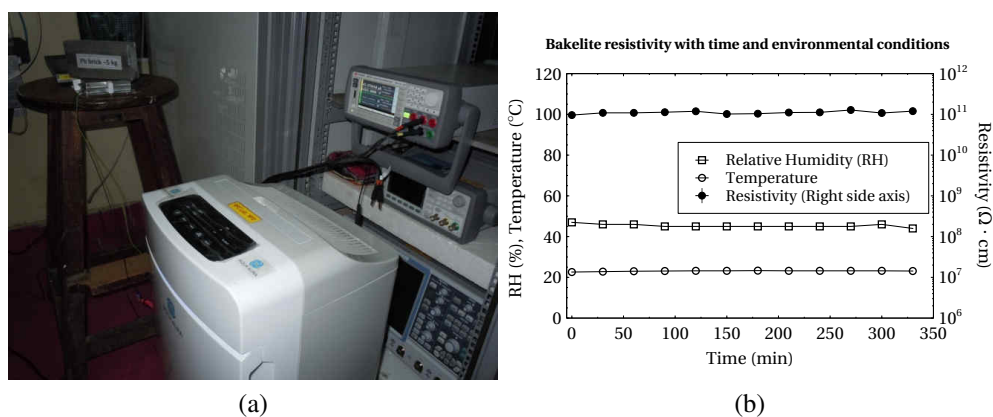
FIGURE 8.2: (a) Resistivity of Indian bakelite being measured. (b) Resistivity of Indian bakelite sample.

detecting contraband materials utilizing the principle of muon tomography. Due to their large area and relatively lower cost they can be used to check for illegal transportation of contraband materials through cargo at seaports and airports.

Muon tomography utilizes muon scattering for identification of materials. If a material has high Z elements the scattering is more.

Alternative gas for Freon-r134a: Freon-r134a is banned in the European union and could be phased out by 2017. It is high time an alternative gas mixture is found for RPCs. R & D in this direction needs to be done. The refrigerant HFO-1234yf is a promising gas in place of freon.

Reactor Anti-neutrino

Detector Simulations: Detector simulations done so far need to be extended to calculate the multiplicities of positron and neutron events in ISMRAN.

These would help in threshold optimization and event logic assessment. Spallation and fast neutron background simulation need to be done.

Background measurements: The BGO detector used in gamma background measurements has a low resolution. It is also sensitive to neutrons in the background. To understand the background properly, measurements with gamma detectors having better resolution such as HPGe or LaBr$_3$ have to be done.

ISMRAN prototype: At the time of writing this thesis, 20 plastic scintillator bars of the plastic mono type have arrived at BARC. A small prototype with these bars called 'Mini-ISMRAN' will be assembled at the Dhruva research reactor hall with shielding for both gamma and neutrons. Neutrons will be shielded using Borated rubber or polythene and lead will be used to shield from gamma. For cosmic muon shielding, active veto detectors will be used.

Shielding design is in the evaluation stage and approval is awaited.

Expected neutrino flux: Reactor burn-up simulation in detail has to be performed to calculate the expected anti-neutrino flux at ISMRAN. Situation in Dhruva is special as ISMRAN would be detecting anti-neutrinos from a natural uranium reactor. Isotopic evolution needs to be determined accurately.

Characterization of CMS RE4/2 bakelite RPCs using Hodoscope

RPCs of the CMS end cap are trapezoidal in shape. RPCs were kept in shelves between the top and bottom plane scintillators of the hodoscope. Schematic of a CMS end cap RPC is shown in Figure A.1. It has two layers of Bakelite gas
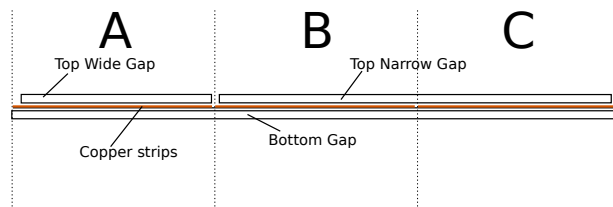
FIGURE A.1: Side view of the RE4-2 RPC illustrating double layered gas gaps.

gaps. The readout of a CMS RE4-2 RPC has a total of 96 strips from three sections (32 strips in each section). The sections are denoted as η = A, B and C which correspond to the different pseudorapidity[1] regions covered by the RPC

---

[1]Pseudorapidity η is a parameter which describes the angle of a particle with respect to the beam axis given by $\eta = -\ln(\tan(\theta/2))$, where θ is the angle between the particle's momentum and positive beam direction.

when employed in the endcap of the CMS detector [84]. The bottom layer has a large gas gap called the BOTTOM gap (covers all sections), and the top layer has two smaller gaps called, TOP WIDE (covers only section A) and TOP NAR-ROW (covers section B and C). The readout, which is also segmented according to the sections, has 32 copper strips in each section longitudinal to the length of the trapezoid. It is sandwiched between the two layers of gas gaps. The trigger
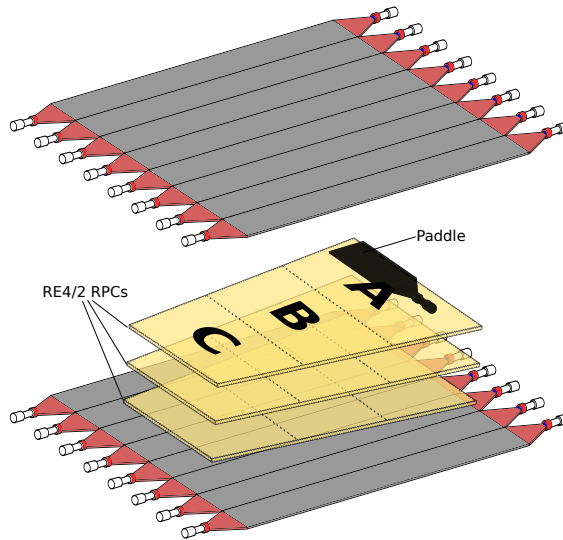
FIGURE A.2: Geometry for the RE4-2 RPC.

geometry is confined to each section by keeping a paddle over the required section using a movable stand (Figure A.1(b)). The dimension of the paddle is 40 cm × 18 cm × 1 cm. Three RPCs are stacked below the paddle in consecutive shelves to be characterized simultaneously.

The gas mixture is composed of Freon-R134a: 95.2%, I-butane: 4.5%, SF6: 0.3%, with ~40% R.H (Relative Humidity).

Sample efficiency plot for the RPC for η = A section using the paddle is shown in Figure A.3.   Efficiency is the No. of counts registered in the RPC section divided by the No. of triggers. Trigger filtering is done at the time of
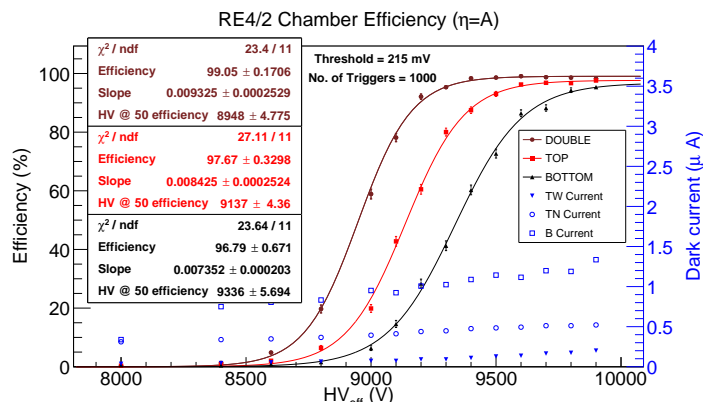
FIGURE A.3: Sample efficiency plot for an RE4/2 RPC using the paddle covering the A section (η = A), for the DOUBLE, TOP and BOTTOM configurations.

analysis neglecting shower events. If more than one scintillator in the top or bottom plane fires for an event, the event is not considered. The No. of triggers shown in Figure A.3 is the hardware trigger. Since the RPC is composed of two layers of gas gaps, efficiency TOP, BOTTOM and DOUBLE correspond to the efficiency of the RPC when the TOP, BOTTOM and both TOP and BOTTOM layers of gaps are powered respectively. The sigmoid function described in Chapter 3 is used to fit the data.

Strip profile and cluster size plots are shown in Figure A.4. They are for the DOUBLE configuration. In Figure A.4(a), the strip channel from 0-31 corresponds to the A section, 32-63: B, and 64-91: C respectively. When we keep the paddle on A section, we observe all counts in that section. Cluster size shown in Figure A.4(b) shows that at a voltage of 9400 V, two strips fire on an average, for a muon event. The variation of the mean cluster size with voltage is shown in Figure A.4(c).

Figure A.4(d) shows the distribution of time of the signals from the 12th strip of the CMS RE4-2 RPC in A section with respect to the time of the trigger.
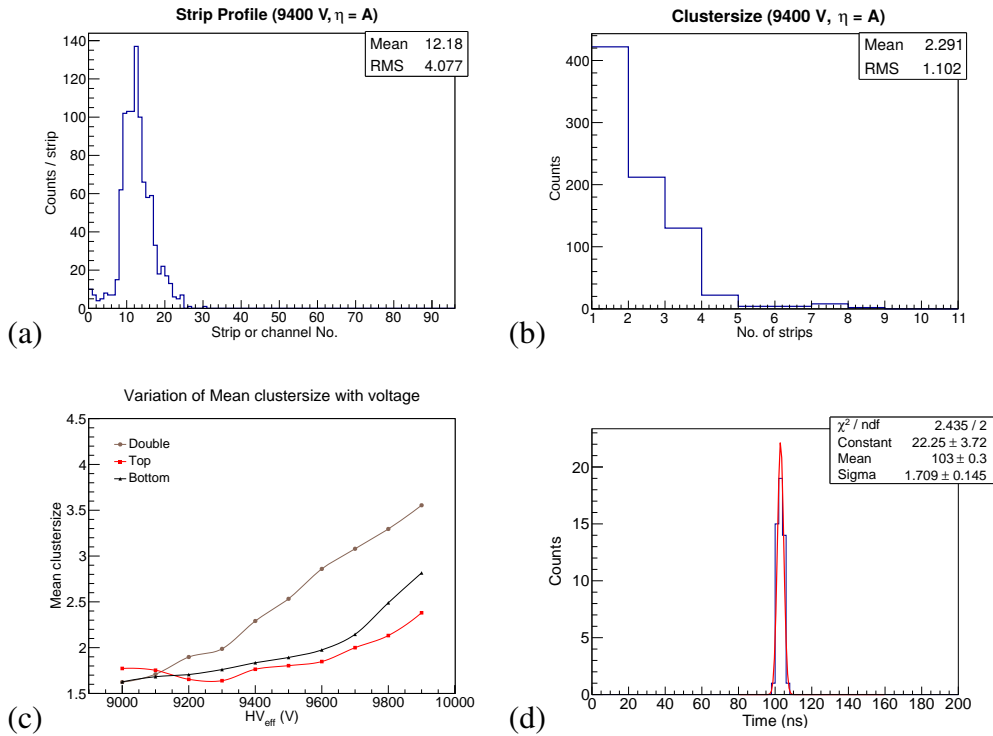
FIGURE A.4: (a) Strip profile for the RPC in the A section at 9400 V. (b) Cluster size for the RPC at 9400 V. (c) Variation of mean cluster size with voltage. (d) The distribution of the time of the signals from the 12th strip to the time of the trigger. All the plots are for the η = A, and DOUBLE configurations.

The value of sigma is ~1.7 ns. From Figure A.5, we can see different regions corresponding to the signals. An interval which spans the RPC signal region is chosen and the hits occuring outside the interval are considered as noise for that particular strip or channel. Noise rate is expressed per unit area of the RPC and is typically < 1 Hz·cm^{-2} at an effective voltage of 9.4 kV.

All the CMS RPCs assembled, and characterized show similar behaviour in terms of efficiency, clustersize, strip profile and noise rate. More information regarding the QC proctocols and chamber performance statistics is given in Ref. [81].
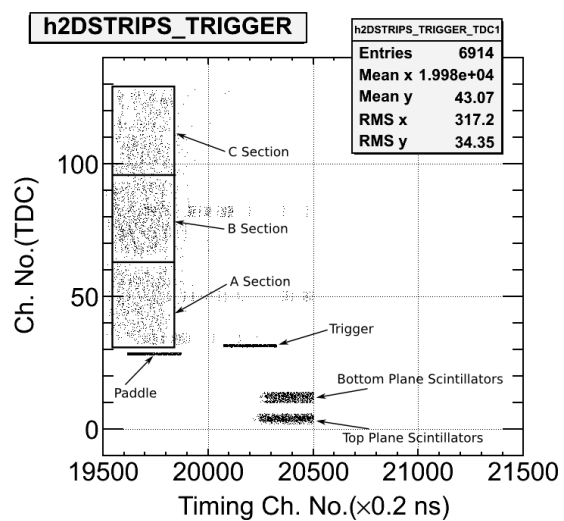
FIGURE A.5: Timing distribution of signals.

Bibliography

[1] INO (ICAL) Collaboration. "Physics Potential of the ICAL detector at the India-based Neutrino Observatory (INO)". In: (May 2015). To be published in Pramana J. Phys. arXiv: `1505.07380v1 [nucl-ex]`.

[2] V.A. Korovkin et al. "Measuring nuclear plant power output by neutrino detection". English. In: *Soviet Atomic Energy* 65.3 (1988), pp. 712–718. ISSN: 0038-531X. DOI: `10.1007/BF01123011`.

[3] R. Santonico and R. Cardarelli. "Development of resistive plate counters". In: *Nuclear Instruments and Methods in Physics Research* 187.2-3 (1981), pp. 377 –380. ISSN: 0167-5087. DOI: `http://dx.doi.org/10.1016/0029-554X(81)90363-3`.

[4] The INO Collaboration. *A Report of the INO Feasibility Study*. Report INO/2006/01. 2006.

[5] V. K. S. Kashyap et al. "Plastic scintillator based hodoscope for characterization of large area RPCs". In: *Pramana J. Phys.* (). Accepted.

[6]   "G-10 read out panel 1 m × 1 m as an option for RPCs in INO". In: *Proceedings of 59th DAE-BRNS Symp. on Nucl. Phys.* 2014, p. 922.

[7]   Th. A. Mueller et al. "Improved predictions of reactor antineutrino spectra". In: *Phys. Rev. C* 83.5 (May 2011), p. 054615. DOI: `10.1103/PhysRevC.83.054615`.

[8]   Patrick Huber. "Determination of antineutrino spectra from nuclear reactors". In: *Phys. Rev. C* 84.2 (Aug. 2011), p. 024617. DOI: `10.1103/PhysRevC.84.024617`.

[9]   G. Mention et al. "Reactor antineutrino anomaly". In: *Phys. Rev. D* 83.7 (Apr. 2011), p. 073006. DOI: `10.1103/PhysRevD.83.073006`.

[10]   A. Porta et al. "Reactor Neutrino Detection for Non Proliferation with the NUCIFER Experiment". In: *Advancements in Nuclear Instrumentation Measurement Methods and their Applications (ANIMMA), 2009 First International Conference on*. June 2009, pp. 1–8. DOI: `10.1109/ANIMMA.2009.5503653`.

[11]   Y. Kuroda et al. "A mobile antineutrino detector with plastic scintillators". In: *Nuclear Instruments and Methods in Physics Research Section A: Accelerators, Spectrometers, Detectors and Associated Equipment* 690.0 (2012), pp. 41 –47. ISSN: 0168-9002. DOI: `http://dx.doi.org/10.1016/j.nima.2012.06.040`
S. Oguri et al. "Reactor antineutrino monitoring with a plastic scintillator array as a new safeguards method". In: *Nuclear Instruments and Methods in Physics Research Section A: Accelerators, Spectrometers, Detec-*

tors and Associated Equipment 757.0 (2014), pp. 33 –39. ISSN: 0168-9002. DOI: `http://dx.doi.org/10.1016/j.nima.2014.04.065`.

[12] M. Battaglieri et al. "An anti-neutrino detector to monitor nuclear reactor's power and fuel composition". In: *Nuclear Instruments and Methods in Physics Research Section A: Accelerators, Spectrometers, Detectors and Associated Equipment* 617.1-3 (2010). 11th Pisa Meeting on Advanced Detectors Proceedings of the 11th Pisa Meeting on Advanced Detectors, pp. 209 –213. ISSN: 0168-9002. DOI: `http://dx.doi.org/10.1016/j.nima.2009.09.031`.

[13] S. Agostinelli et al. "Geant4 - a simulation toolkit". In: *Nuclear Instruments and Methods in Physics Research Section A: Accelerators, Spectrometers, Detectors and Associated Equipment* 506.3 (2003), pp. 250 –303. ISSN: 0168-9002. DOI: `http://dx.doi.org/10.1016/S0168-9002(03)01368-8`.

[14] V. K. S. Kashyap et al. "Simulation results of liquid and plastic scintillator detectors for reactor antineutrino detection - A comparison". In: *Journal of Instrumentation* 11.03 (2016), P03005.

[15] J. C. Street and E. C. Stevenson. "New Evidence for the Existence of a Particle of Mass Intermediate Between the Proton and Electron". In: *Phys. Rev.* 52.9 (1937), pp. 1003–1004. DOI: `10.1103/PhysRev.52.1003`.

[16] Seth H. Neddermeyer and Carl D. Anderson. "Note on the Nature of Cosmic-Ray Particles". In: *Phys. Rev.* 51.10 (1937), pp. 884–886. DOI: `10.1103/PhysRev.51.884`.

[17]   C. L. Cowan et al. "Detection of the Free Neutrino: a Confirmation". In: *Science* 124.3212 (1956), pp. 103–104. ISSN: 0036-8075. DOI: `10.1126/science.124.3212.103`. eprint: `http://science.sciencemag.org/content/124/3212/103.full.pdf`.

[18]   C. S. Wu et al. "Experimental Test of Parity Conservation in Beta Decay". In: *Phys. Rev.* 105.4 (1957), pp. 1413–1415. DOI: `10.1103/PhysRev.105.1413`.

[19]   Richard L. Garwin, Leon M. Lederman, and Marcel Weinrich. "Observations of the Failure of Conservation of Parity and Charge Conjugation in Meson Decays: the Magnetic Moment of the Free Muon". In: *Phys. Rev.* 105.4 (1957), pp. 1415–1417. DOI: `10.1103/PhysRev.105.1415`.

[20]   G. Danby et al. "Observation of High-Energy Neutrino Reactions and the Existence of Two Kinds of Neutrinos". In: *Phys. Rev. Lett.* 9.1 (1962), pp. 36–44. DOI: `10.1103/PhysRevLett.9.36`.

[21]   M. L. Perl et al. "Evidence for Anomalous Lepton Production in $e^+ - e^-$ Annihilation". In: *Phys. Rev. Lett.* 35 (22 1975), pp. 1489–1492. DOI: `10.1103/PhysRevLett.35.1489`.

[22]   K. Kodama et al. "Observation of tau neutrino interactions". In: *Physics Letters B* 504.3 (2001), pp. 218 –224. ISSN: 0370-2693. DOI: `http://dx.doi.org/10.1016/S0370-2693(01)00307-0`.

[23]   Peter W. Higgs. "Broken Symmetries and the Masses of Gauge Bosons". In: *Phys. Rev. Lett.* 13.16 (1964), pp. 508–509. DOI: `10.1103/PhysRevLett.13.508`.

[24] F. Englert and R. Brout. "Broken Symmetry and the Mass of Gauge Vector Mesons". In: *Phys. Rev. Lett.* 13.9 (1964), pp. 321–323. DOI: `10.1103/PhysRevLett.13.321`.

[25] G. S. Guralnik, C. R. Hagen, and T. W. B. Kibble. "Global Conservation Laws and Massless Particles". In: *Phys. Rev. Lett.* 13.20 (1964), pp. 585–587. DOI: `10.1103/PhysRevLett.13.585`.

[26] G. Aad et al. "Observation of a new particle in the search for the Standard Model Higgs boson with the ATLAS detector at the LHC". In: *Physics Letters B* 716.1 (2012), pp. 1 –29. ISSN: 0370-2693. DOI: `http://dx.doi.org/10.1016/j.physletb.2012.08.020`.

[27] S. Chatrchyan et al. "Observation of a new boson at a mass of 125 GeV with the CMS experiment at the LHC". In: *Physics Letters B* 716.1 (2012), pp. 30 –61. ISSN: 0370-2693. DOI: `http://dx.doi.org/10.1016/j.physletb.2012.08.021`.

[28] P. Anselmann et al. "Solar neutrinos observed by GALLEX at Gran Sasso". In: *Physics Letters B* 285.4 (1992), pp. 376 –389. ISSN: 0370-2693. DOI: `http://dx.doi.org/10.1016/0370-2693(92)91521-A`.

[29] J.N. Abdurashitov et al. "Results from SAGE (The Russian-American gallium solar neutrino experiment)". In: *Physics Letters B* 328.1 (1994), pp. 234 –248. ISSN: 0370-2693. DOI: `http://dx.doi.org/10.1016/0370-2693(94)90454-5`.

[30] The NUSEK Collaboration, M. Aglietta et al. "Experimental Study of Atmospheric Neutrino Flux in the NUSEX Experiment". In: *EPL (Europhysics Letters)* 8.7 (1989), p. 611.

[31]   Ch. Berger et al. "Study of atmospheric neutrino interactions with the
       Fréjus detector". In: *Physics Letters B* 227.3 (1989), pp. 489 –494. ISSN:
       0370-2693. DOI: `http://dx.doi.org/10.1016/0370-2693(89)`
       `90968-4`.

[32]   W.W.M. Allison et al. "Measurement of the atmospheric neutrino flavour
       composition in Soudan 2". In: *Physics Letters B* 391.3–4 (1997), pp. 491
       –500. ISSN: 0370-2693. DOI: `http://dx.doi.org/10.1016/S0370-`
       `2693(96)01609-7`.

[33]   J Boger et al. "The Sudbury Neutrino Observatory". In: *Nuclear Instru-
       ments and Methods in Physics Research Section A: Accelerators, Spec-
       trometers, Detectors and Associated Equipment* 449.1–2 (2000), pp. 172
       –207. ISSN: 0168-9002. DOI: `http://dx.doi.org/10.1016/S0168-`
       `9002(99)01469-2`.

[34]   Q. R. Ahmad et al. "Measurement of the Rate of $\nu_e + d \rightarrow p + p + e^-$
       Interactions Produced by ^8B Solar Neutrinos at the Sudbury Neutrino
       Observatory". In: *Phys. Rev. Lett.* 87.7 (2001), p. 071301. DOI: `10.1103/`
       `PhysRevLett.87.071301`.

[35]   K. Abe et al. "Indication of Electron Neutrino Appearance from an Accelerator-
       Produced Off-Axis Muon Neutrino Beam". In: *Phys. Rev. Lett.* 107.4
       (2011), p. 041801. DOI: `10.1103/PhysRevLett.107.041801`.

[36]   D. G. Michael et al. "Observation of Muon Neutrino Disappearance with
       the MINOS Detectors in the NuMI Neutrino Beam". In: *Phys. Rev. Lett.*
       97.19 (2006), p. 191801. DOI: `10.1103/PhysRevLett.97.191801`.

[37] F. P. An et al. "Observation of Electron-Antineutrino Disappearance at Daya Bay". In: *Phys. Rev. Lett.* 108.17 (2012), p. 171803. DOI: `10.1103/ PhysRevLett.108.171803`.

[38] Y. Abe et al. "Reactor $\overline{\nu}_e$ disappearance in the Double Chooz experiment". In: *Phys. Rev. D* 86.5 (2012), p. 052008. DOI: `10.1103/PhysRevD. 86.052008`.

[39] J. K. Ahn et al. "Observation of Reactor Electron Antineutrinos Disappearance in the RENO Experiment". In: *Phys. Rev. Lett.* 108.19 (2012), p. 191802. DOI: `10.1103/PhysRevLett.108.191802`.

[40] B. Pontecorvo. "Neutrino Experiments and the Problem of Conservation of Leptonic Charge". In: *Soviet Journal of Experimental and Theoretical Physics* 26 (May 1968), p. 984.

[41] Ziro Maki, Masami Nakagawa, and Shoichi Sakata. "Remarks on the Unified Model of Elementary Particles". In: *Progress of Theoretical Physics* 28.5 (1962), pp. 870–880. DOI: `10.1143/PTP.28.870`. eprint: `http:// ptp.oxfordjournals.org/content/28/5/870.full.pdf+html`.

[42] John N. Bahcall and Steven C. Frautschi. "Neutrino Astronomy and Intermediate Bosons". In: *Phys. Rev.* 135.3B (1964), B788–B791. DOI: `10. 1103/PhysRev.135.B788`.

[43] H. Fritsch and P. Minkowski. "Vectorlike weak currents, massive neutrinos, and neutrino beam oscillations". In: *Physics Letters B* 62.1 (1976), pp. 72 –76. ISSN: 0370-2693. DOI: `http://dx.doi.org/10.1016/ 0370-2693(76)90051-4`.

[44]   Shalom Eliezer and Arthur R. Swift. "Experimental consequences of $\nu_e \to \nu_\mu$ mixing in neutrino beams". In: *Nuclear Physics B* 105.1 (1976), pp. 45–51. ISSN: 0550-3213. DOI: `http://dx.doi.org/10.1016/0550-3213(76)90059-6`.

[45]   C. Giunti and C. W. Kim. *Fundamentals of Neutrino Physics and Astrophysics*. Oxford University Press, 2007. ISBN: 978–0–19–850871–7 (Hbk).

[46]   L. Wolfenstein. "Neutrino oscillations in matter". In: *Phys. Rev. D* 17.9 (1978), pp. 2369–2374. DOI: `10.1103/PhysRevD.17.2369`.

[47]   S. P. Mikheev and A. Yu. Smirnov. "Resonance enhancement of oscillations in matter and solar neutrino spectroscopy". In: *Soviet Journal of Nuclear Physics* 42.6 (1985), pp. 913–917.

[48]   W. H. Furry. "On Transition Probabilities in Double Beta-Disintegration". In: *Phys. Rev.* 56 (12 1939), pp. 1184–1193. DOI: `10.1103/PhysRev.56.1184`.

[49]   C Arnaboldi et al. "CUORE: a cryogenic underground observatory for rare events". In: *Nuclear Instruments and Methods in Physics Research Section A: Accelerators, Spectrometers, Detectors and Associated Equipment* 518.3 (2004), pp. 775 –798. ISSN: 0168-9002. DOI: `http://dx.doi.org/10.1016/j.nima.2003.07.067`.

[50]   K. H. Ackermann et al. "The Gerda experiment for the search of $0\nu\beta\beta$ decay in 76Ge". In: *The European Physical Journal C* 73.3 (2013), pp. 1–29. ISSN: 1434-6052. DOI: `10.1140/epjc/s10052-013-2330-0`.

[51] W Xu et al. "The Majorana Demonstrator: A Search for Neutrinoless Double-beta Decay of 76 Ge". In: *Journal of Physics: Conference Series* 606.1 (2015), p. 012004.

[52] S. Andringa, E. Arushanova, S. Asahi, et al. "Current Status and Future Prospects of the SNO+ Experiment". In: *Advances in High Energy Physics* 2016.6194250 (2016), p. 21. DOI: `10.1155/2016/6194250`.

[53] V. Singh et al. "Simulation studies for Tin Bolometer Array for Neutrinoless Double Beta Decay". In: (July 2015). arXiv: `1408.4520 [physics.ins-det]`.

[54] K. A. Olive et al. "Review of Particle Physics". In: *Chin. Phys.* C38 (2014), p. 090001. DOI: `10.1088/1674-1137/38/9/090001`.

[55] Kajita T. "Atmospheric neutrinos and discovery of neutrino oscillations". In: *Proceedings of the Japan Academy. Series B, Physical and Biological Sciences*. Vol. 86. 4. Apr. 2010, pp. 303–321. DOI: `http://doi.org/10.2183/pjab.86.303`.

[56] D. Ayres et al. "Letter of Intent to build an Off-axis Detector to study numu to nue oscillations with the NuMI Neutrino Beam". In: (Oct. 2002). arXiv: `hep-ex/0210005 [hep-ex]`.

[57] K. Abe et al. "Letter of Intent: The Hyper-Kamiokande Experiment — Detector Design and Physics Potential —". In: (Sept. 2011). arXiv: `1109.3262 [hep-ex]`.

[58] The IceCube-PINGU Collaboration. "Letter of Intent: The Precision IceCube Next Generation Upgrade (PINGU)". In: (Jan. 2014). arXiv: `1401.2046 [physics.Ins-det]`.

[59]   The LBNE Collaboration, T. Akiri et al. "The 2010 Interim Report of
        the Long-Baseline Neutrino Experiment Collaboration Physics Working
        Groups". In: (Oct. 2011). arXiv: `1110.6249` `[hep-ex]`.

[60]   LAGUNA-LBNO Collaboration, S. K. Agarwalla et al. "The mass-hierarchy
        and CP-violation discovery reach of the LBNO long-baseline neutrino
        experiment". In: (Jan. 2014). arXiv: `1312.6250` `[hep-ph]`.

[61]   Yu-Feng Li. "Overview of the Jiangmen Underground Neutrino Obser-
        vatory (JUNO)". In: *International Journal of Modern Physics: Confer-
        ence Series* 31 (2014), p. 1460300. DOI: `10.1142/S2010194514603007`.
        eprint: `http://www.worldscientific.com/doi/pdf/10.1142/`
        `S2010194514603007`.

[62]   The T2K Collaboration, K. Abe, et al. "Neutrino oscillation physics po-
        tential of the T2K experiment". In: *Progress of Theoretical and Exper-
        imental Physics* 2015.4 (2015). DOI: `10.1093/ptep/ptv031`. eprint:
        `http://ptep.oxfordjournals.org/content/2015/4/043C01.`
        `full.pdf+html`.

[63]   D. Buskulic et al. "A direct measurement of the invisible width of the
        Z from single photon counting". In: *Physics Letters B* 313.3 (1993),
        pp. 520 –534. ISSN: 0370-2693. DOI: `http://dx.doi.org/10.1016/`
        `0370-2693(93)90027-F`.

[64]   R. Akers et al. "Measurement of single photon production in e^+e- col-
        lisions near the Z_0 resonance". In: *Zeitschrift für Physik C Particles
        and Fields* 65.1 (1995), pp. 47–65. ISSN: 1431-5858. DOI: `10.1007/`
        `BF01571303`.

[65]   DELPHI Collaboration. "Search for new phenomena using single photon events at LEP1". In: *Zeitschrift für Physik C Particles and Fields* 74.4 (1997), pp. 577–586. ISSN: 1431-5858. DOI: `10.1007/s002880050421`.

[66]   M. Acciarri et al. "Determination of the number of light neutrino species from single photon production at LEP". In: *Physics Letters B* 431.1–2 (1998), pp. 199 –208. ISSN: 0370-2693. DOI: `http://dx.doi.org/10.1016/S0370-2693(98)00519-X`.

[67]   The ALEPH Collaboration, The DELPHI Collaboration, The L3 Collaboration, The OPAL Collaboration, The SLD Collaboration, The LEP Electroweak Working Group, The SLD Electroweak and Heavy Flavour Groups. "Precision electroweak measurements on the Z resonance". In: *Physics Reports* 427.5–6 (2006), pp. 257 –454. ISSN: 0370-1573. DOI: `http://dx.doi.org/10.1016/j.physrep.2005.12.006`.

[68]   A. Aguilar et al. "Evidence for neutrino oscillations from the observation of $\overline{\nu}_e$ appearance in a $\overline{\nu}_\mu$ beam". In: *Phys. Rev. D* 64.11 (2001), p. 112007. DOI: `10.1103/PhysRevD.64.112007`.

[69]   A. A. Aguilar-Arevalo et al. "Event Excess in the MiniBooNE Search for $\overline{\nu}_\mu \rightarrow \overline{\nu}_e$ Oscillations". In: *Phys. Rev. Lett.* 105 (18 2010), p. 181801. DOI: `10.1103/PhysRevLett.105.181801`.

[70]   K. N. Abazajian et al. "Light Sterile Neutrinos: A White Paper". In: (Apr. 2012). arXiv: `1204.5379v1` [`hep-ph, astro-ph.CO, hep-ex, nucl-ex, nucl-th`].

[71]   N. S. Bowden et al. "Observation of the Isotopic Evolution of Pressurized Water Reactor Fuel using an Antineutrino Detector". In: (Oct. 2008). arXiv: `0808.0698v2` `[nucl-ex]`.

[72]   Carlo Bemporad, Giorgio Gratta, and Petr Vogel. "Reactor-based neutrino oscillation experiments". In: *Rev. Mod. Phys.* 74.2 (Mar. 2002), pp. 297–328. DOI: `10.1103/RevModPhys.74.297`.

[73]   Yu.V. Klimov et al. "Neutrino method remote measurement of reactor power and power output". English. In: *Atomic Energy* 76.2 (1994), pp. 123–127. ISSN: 1063-4258. DOI: `10.1007/BF02414355`.

[74]   N.S. Bowden et al. "Experimental results from an antineutrino detector for cooperative monitoring of nuclear reactors". In: *Nuclear Instruments and Methods in Physics Research Section A: Accelerators, Spectrometers, Detectors and Associated Equipment* 572.2 (2007), pp. 985 –998. ISSN: 0168-9002. DOI: `http://dx.doi.org/10.1016/j.nima.2006.12.015`.

[75]   J. Warren Keuffel. "Parallel-Plate Counters". In: *Review of Scientific Instruments* 20.3 (1949), pp. 202–208. DOI: `http://dx.doi.org/10.1063/1.1741489`.

[76]   V.V. Parkhomchuk, Yu.N. Pestov, and N.V. Petrovykh. "A spark counter with large area". In: *Nuclear Instruments and Methods* 93.2 (1971), pp. 269 –270. ISSN: 0029-554X. DOI: `http://dx.doi.org/10.1016/0029-554X(71)90475-7`.

[77]   Yu.N. Pestov. "Status and future developments of spark counters with a localized discharge". In: *Nuclear Instruments and Methods in Physics*

Research 196.1 (1982), pp. 45 –47. ISSN: 0167-5087. DOI: `http://dx.doi.org/10.1016/0029-554X(82)90614-0`.

[78] Giacomo Luca Bruno. "The RPC detectors and the muon system for the CMS experiment at the LHC". PhD thesis. Università degli Studi di Pavia, 2000-2001.

[79] Christian Lippmann. "Detector Physics of Resistive Plate Chambers". PhD thesis. CERN, 2003.

[80] M. Abbrescia et al. "Cosmic ray tests of double-gap resistive plate chambers for the CMS experiment". In: *Nuclear Instruments and Methods in Physics Research Section A: Accelerators, Spectrometers, Detectors and Associated Equipment* 550.1-2 (2005), pp. 116 –126. ISSN: 0168-9002. DOI: `http://dx.doi.org/10.1016/j.nima.2005.06.074`.

[81] S. Colafranceschi et al. "Resistive plate chambers for 2013-2014 muon upgrade in CMS at LHC". In: *Journal of Instrumentation* 9.10 (2014), p. C10033.

[82] URL: `http://www.jensign.com/RG58U/`.

[83] Rick Hartley. *RF / Microwave PC Board Design and Layout*. [Online; accessed 23-May-2015]. 2015.

[84] The CMS Collaboration. *CMS, the Compact Muon Solenoid*. Muon Technical Design Report CERN-LHCC-97-32. 1997.

[85] CAEN. *Technical Information Manual, Revision n. 13*. 00104/03: V1X90.MUTx/13. 2012.

[86]   *Hybrid Micro Circuit, BMC-1513, Fast Amplifier*. Bharat Electronics Ltd. Feb. 2002.

[87]   V. B. Chandratre et al. *A short report on the Performance of BARC HMCs for INO detectors*. Report. Mar. 2008.

[88]   Rene Brun and Fons Rademakers. "ROOT - An object oriented data analysis framework". In: *Nuclear Instruments and Methods in Physics Research Section A: Accelerators, Spectrometers, Detectors and Associated Equipment* 389.1-2 (1997). New Computing Techniques in Physics Research V, pp. 81 –86. ISSN: 0168-9002. DOI: `http://dx.doi.org/10.1016/S0168-9002(97)00048-X`.

[89]   K. Hari Prasad, V. B. Chandratre, et al. "Design and development of portable DAQ system for RPC readout". In: *DAE-BRNS National Symposium on Nuclear Instrumentation*. 2013.

[90]   K. Hari Prasad et al. "Proceedings of International Conference on VLSI, Communication, Advanced Devices, Signals & Systems and Networking (VCASAN-2013)". In: ed. by S. Veena Chakravarthi, M. Yasha Jyothi Shirur, and Rekha Prasad. India: Springer India, 2013. Chap. A CMOS Standard Cell-Based Time-to-Digital Converter, pp. 87–93. ISBN: 978-81-322-1524-0. DOI: `10.1007/978-81-322-1524-0_13`.

[91]   *78 mm (3″) photomultiplier 9265B series data sheet, 130 mm (5″) photomultiplier 9823B series data sheet*. Accessed : 2015-10-05. ET Enterprises Limited.

[92] *EJ-200 Plastic Scintillator, EJ-331 and EJ-335 Gadolinium Loaded Liquid Scintillators, EJ-500 Optical Cement*. Accessed : 2015-09-16. Eljen Technology.

[93] *BC-525 Gd Loaded Mineral Oil Based Liquid Scintillators, BC-521 Gadolinium Loaded Liquid Scintillators, BC-505 Liquid Scintillators*. Accessed : 2015-09-26. Saint-Gobain Ceramics and Plastics, Inc.

[94] *BC-400, BC-404, BC-408, BC412, BC-416, Premium Plastic Scintillators*. Saint-Gobain Ceramics and Plastics, Inc. June 2014.

[95] V. I. Tretyak. "Semi-empirical calculation of quenching factors for ions in scintillators". In: (Sept. 2009). arXiv: `0911.3041v1 [nucl-ex]`.

[96] Zhang Jian-Fu et al. "Measurements of the light output functions of plastic scintillator using ^{9}Be(d, n)^{10}B reaction neutron source". In: *Chinese Physics C* 34.7 (2010), p. 988.

[97] Giulia Hull et al. "New Organic Crystals for Pulse Shape Discrimination". In: *Nuclear Science, IEEE Transactions on* 56.3 (June 2009), pp. 899–903. ISSN: 0018-9499. DOI: `10.1109/TNS.2009.2015944`.

[98] D. Motta and S. Schönert. "Optical properties of bialkali photocathodes". In: *Nuclear Instruments and Methods in Physics Research Section A: Accelerators, Spectrometers, Detectors and Associated Equipment* 539.1-2 (2005), pp. 217 –235. ISSN: 0168-9002. DOI: `http://dx.doi.org/10.1016/j.nima.2004.10.009`.

[99] *BC-622A, Reflector Paint for Liquid Scintillator Tanks*. Saint-Gobain Ceramics and Plastics, Inc. 2014.

[100]   Matthew W. Francis et al. *Reactor Fuel Isotopics and Code Validation for Nuclear Applications*. Report ORNL/TM-2014/464. Oak Ridge, Tennessee 37831-6283, USA: Oak Ridge National Laboratory, Sept. 2014.

[101]   P. Huber, M. Lindner, and W. Winter. "Superbeams vs. neutrino factories". In: *Nuclear Physics B* 645.1-2 (2002), pp. 3 –48. ISSN: 0550-3213. DOI: `http://dx.doi.org/10.1016/S0550-3213(02)00825-8`.

[102]   P. Vogel. "Analysis of the antineutrino capture on protons". In: *Phys. Rev. D* 29.9 (May 1984), pp. 1918–1922. DOI: `10.1103/PhysRevD.29.1918`.

[103]   Tomasz Skwarnicki. "A Study of the radiative cascade transitions between the Upsilon-prime and Upsilon resonances". Appendix-E. PhD thesis. Institute of Nuclear Physics, Cracow and Deutsches Elektronen-Synchrotron DESY, Hamburg, 1986.

[104]   Horst Schölermann and Horst Klein. "Optimizing the energy resolution of scintillation counters at high energies". In: *Nuclear Instruments and Methods* 169.1 (1980), pp. 25 –31. ISSN: 0029-554X. DOI: `http://dx.doi.org/10.1016/0029-554X(80)90097-X`.

[105]   Glenn F. Knoll. *Radiation Detection and measurement*. 3rd ed. Wiley India Pvt. Ltd, 2009. ISBN: 978–81–265–2260–6.

[106]   URL: `https://en.wikipedia.org/wiki/Neutron_temperature`.

[107]   A. K. Singh et al. "Performance characteristics of a thermal neutron detector based on $Li_6Y(BO_3)_3$: Ce single crystals". In: *DAE-BRNS Symposium on Nuclear Physics*. Vol. 59. 2014, p. 896.

[108] A. K. Singh et al. "Variation in the thermal neutron flux at the antineutrino measurement site in the Dhruva reactor". In: *DAE-BRNS Symposium on Nuclear Physics*. Vol. 60. 2015, p. 968.

[109] V. K. S Kashyap et al. "Time distribution measurements of prompt-delay events at the Dhruva reactor for detection of antineutrinos". In: *DAE-BRNS Symposium on Nuclear Physics*. Vol. 60. 2015, p. 924.

[110] CAEN. *User Manual, V1730 & VX1730, 16/8-channel, 14-bit, 500 MS/s Waveform Digitizer*. UM2792. 2014.

[111] V. K. S. Kashyap, A. Joshi, and L. M. Pant. "Development of large area (1 m × 2 m) bakelite gas-gaps in India for INO and related experiments". In: *DAE-BRNS Symposium on Nuclear Physics*. Vol. 60. 2015, p. 946.